Programme Area: Carbon Capture and Storage

Project: Hydrogen Turbines Follow On

Title: Salt Cavern Appraisal for Hydrogen and Gas Storage – Appendices

Abstract:

With the growth of renewables a clean, dispatchable power source will be required in the 2030s. One scheme for providing this involves storing large quantities of H2 in salt caverns, and to use the inventory to produce power or heat during peak hours. Although H2 is stored already in caverns in the UK, there has been little work on the effect of rapid repetitive cycling on cavern integrity. The suitability of UK salt caverns for use in storing H2 in rapid cycle mode is examined, based on detailed geotechnical analysis of saltfields in Yorkshire, Teesside and Cheshire. A detailed analysis is carried out by Atkins on a Cheshire cavern, using a combination of superimposed seasonal and daily demand patterns .The limitations of today's market offering for firing H2 in gas turbines is described. Outline costing for schemes taking H2 from salt caverns and producing power are presented.

Context:

This knowledge gathering project collated data on the performance of gas turbines (conventional and novel cycles) operating on methane, hydrogen and mixtures of the two. It carried out plant and whole system modelling with the aim of understanding how much and in what circumstances gas (with and without CCS) is investable and fits and where it is unlikely to fit easily in the developing energy system from 2020-2050, to meet the increasing requirements for flexibility against an increasingly carbon-constrained system. The gas turbine generation work, was targeted at identifying improved configurations that could be taken to concept stage. At a wider level, the work provided greater understanding of factors affecting the deployment of methane and hydrogen turbines in the UK market and provided better, more accurate performance data for key configurations for future system modelling.

ATKINS

Appendix A:
Baseline information and assumptions

A.1. Hydrogen fuel stream compositions

The following table presents the compositions of the streams considered within this study.

Table A1-1: Hydrogen Fuel Stream Compositions

Parameter	Units	Stream 1 ('pure H_2')	Stream 2 ('syngas variant')	Natural Gas
Stream description	-	89 mol% H_2 stream from Biomass / Coal Gasification	53 mol% H_2, N_2 rich stream from Auto-thermal Reforming of NG	In line with the UK NTS gas quality specification
Hydrogen	mol%	89.12	52.68	0.00
Carbon Monoxide	mol%	1.53	0.59	0.09
Carbon Dioxide	mol%	4.36	1.07	0.02
Nitrogen	mol%	4.34	44.53	3.65
Oxygen	mol%	-	-	0.00
Argon	mol%	0.39	0.53	0.00
Water	mol%	0.16	0.21	0.00
Methane	mol%	-	0.38	87.78
Ethane	mol%	-	-	8.46
Wobbe Index	MJ/m^3	24.7	9.1	49.6
LHV	MJ/kg	39.7	9.0	46.7

A.2. Geology and Stratigraphy of UK salt fields

A.2.1. East Yorkshire

The basin-filling Fordon Evaporites, where the Atwick and Aldbrough caverns in East Yorkshire have been developed, thin rapidly westwards but thicken sharply eastwards to more than 300 m (Smith, 1989) as shown in Figure A2-1.

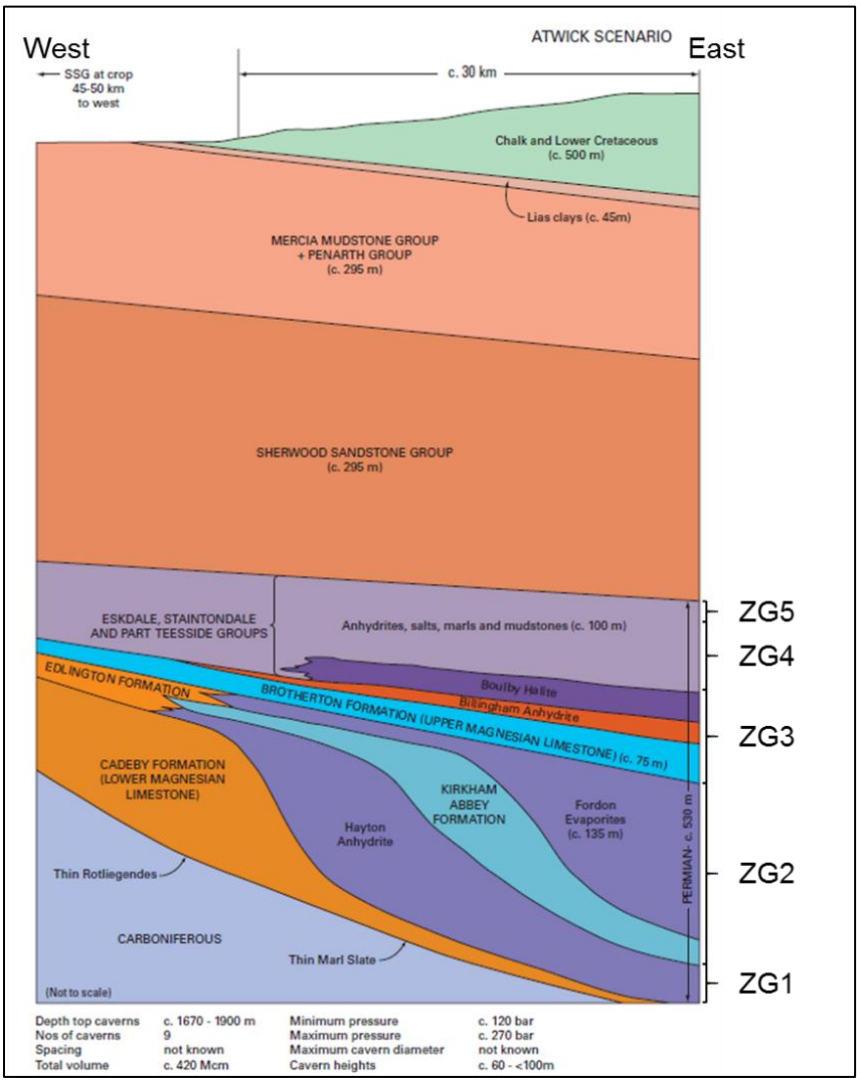

Figure A2-1: Sketch section illustrating the geological conditions likely to represent the NE England Permian formations (Evans, 2008)

A.2.1.1. Regional geological framework

This section of the report utilises the relevant geology-based information provided by the East Yorkshire gas storage operator (SSE Gas Storage) that have been derived from:

- drilling reports,
- openhole wireline logs,
- mudlogs cuttings descriptions,

- 2D seismic data and interpreted structural maps, and
- geologic reports.

The available data were used to develop an understanding of the stratigraphy and the structural geology in the broader Atwick and Aldbrough sites. It is considered that this study is representative of the East Yorkshire region including both the Atwick and Aldbrough cavern site, in fact Evans (2008) indicates that the general geological succession at Aldbrough is the same at Atwick.

The Atwick site is located in the area of an east-west trending basement high known as the Market Weighton Block; a structural high, which extends from the Humber Estuary to Flamborough Head. The Market Weighton Block may have been forming a barrier between two depositional areas, the Cleveland Basin in the north and the Humber Basin and Gainsborough Trough to the south east and south west, respectively; where the Market Weighton Block is characterised by decreased bed thicknesses since at least the end of the Triassic and by a major hiatus encompassing much of the Jurassic sequence.

Within the Market Weighton Block, the late Palaeozoic to Mesozoic units form approximately north-south striking, eastward dipping rock. Therefore, most of the stratigraphical units drilled at depth at Atwick are known from shallower wells or from surface outcrops updip (West) of the site: the Sherwood Sandstone is distributed in the Vale of York – where it forms an important groundwater aquifer – while further west, the Zechstein dolomitic carbonates form a narrow strip along the eastern edge of the Pennines.

It should be noted that corresponding offshore geological strata are located in the southern North Sea and due to hydrocarbon exploration are well-known. However, there is a separate lithostratigraphy for onshore and offshore areas.

A.2.1.2. Regional structural geology

The tectonic setting around Atwick is characterised by normal faulting with two major, N-S to NNW-SSE trending and eastward-dipping faults (or fault zones) of 50 m to 100 m vertical offset west of the cavern site. Furthermore, minor faults with smaller vertical offset can be expected to be present in the area, and there is evidence that these also occur in the cavern field itself; where, given the prevailing lithology of the Atwick sequence, fault planes are rather assumed to be sealed with clay or secondary mineralisation than to provide flow paths for gas (except for, possibly, localised open fissures in dolomite and/or anhydrite rocks of the Zechstein group).

A geological assessment undertaken by British Gas in 1991 indicates that areas to the north and east of the present facility at Atwick are unsuitable for cavity development due to the presence of faulting; the south Atwick site appears to be less risky in terms of tectonic faulting (Knott & Haynes, 1991).

A.2.1.3. Site stratigraphy

The site-specific stratigraphy for the overburden sequence above the ZG2 Halite (shown in the Table A2-1) is aligned with Southern North Sea and Eastern England stratigraphic schemes. However, the definition of formation tops may not correspond in every detail to that of the British Geological Survey stratigraphic scheme. The main source of reference for the adopted stratigraphy has been Johnson et al (1994) and Lott & Knox (1994) which provide stratigraphic interpretations of numerous well logs run over the relevant formations offshore. This offshore information is supplemented by regional accounts in Brenchley & Rawson (2006) and Woodcock & Strachan (2002).

The stratigraphy adopted in this study is shown in Table A2-1, where the anticipated stratum below the ZG2 Halite conforms to the description provided by Evans (2008). In the numerical geomechanical modelling of the caverns the stratigraphic succession from the Carnallitic Marl and up to the surface is not explicitly modelled. Instead, the overburden loading from these layers has been applied to the top of the model as a uniformly distributed pressure. Consequently, the detailed stratigraphy and, in particular, the density of all the encountered geological materials above the Carnallitic marl were used for the estimation of the respective vertical geostatic stress gradient.

Table A2-1: Idealised average stratigraphic column for the East Yorkshire

System	Stratigraphic units			Estimated correlation with the BGS stratigraphic scheme	Typical description from available borehole data	Approximate thickness [m]
	Group		Member			
Quaternary	**Glacial Till**			North Sea Coast Glacigenic	Plastic grey clay with pebbles of coal, sandstone and shale.	30 - 35
Cretaceous	**Chalk Group**			Chalk Group	White, firm, chalky limestones with soft white marly limestones with bands of flint.	506 - 526
Jurassic	**Lias Group**			Lias Group	Slightly silty, slightly calcareous, thinly laminated shales.	15 - 30
Triassic	**Penarth Group**		**Upper Penarth**	Penarth Group	Silty shales containing limestone nodules, grey shales and thin inter-beds of bioclastic limestones.	15 - 17
			Lower Penarth			
	Mercia Mudstone		**Keuper Evaporite**	Blue Anchor Formation	Red, silty shales with bands of grey shales often containing blebs of anhydrite.	295 - 323
				Mercia Mudstone Group		
			Muschelkalk Evaporite Member			
			Röt Evaporite Member			
	Sherwood Sandstone Group			Sherwood Sandstone Group	**Sherwood Sandstone**: Red, medium to fine grained, well sorted, slightly argillaceous sandstone. **Lower Bunter Shale**: Soft to frim red shales with frequent anhydrite stringers.	514 - 529
	Eskdale Group		**Amethyst Member**		No description available.	90 - 95
Permian			**Brockleschiefer Member**	Roxby Formation	Shales, sands and siltstones.	
	Zechstein Group	**ZG4**	**ZG4 Halite**	Zechstein Group	Bed of anhydrite underlain by red shales, siltstone and halite.	**Upper halite***: 17 - 42 **Upper Anhydrite*:** 0 - 10

System	Stratigraphic units			Estimated correlation with the BGS stratigraphic scheme	Typical description from available borehole data	Approximate thickness [m]
	Group		Member			
			Red Salt Clay		**Carnallitic Marl**: Very soft, red shales with varying amounts of potash salt with small amounts of halite and anhydrite.	**Carnallitic Marl**[1]: 19 - 30
		ZG3	**ZG3 Halite** (Boulby Halite, Billingham/Main Anhydrite and Brotherton Formation)		Two units: an upper halite zone, underlain by a grey, slightly argillaceous anhydrite zone.	100 - 112
			Upper Magnesian Limestone		No description available.	
		ZG2	**ZG2 Halite**		**Grauer Salzton**: Argillaceous beds of grey halitic clay. **Fordon Evaporites**: Halite, anhydrite, polyhalite and kieserite.	**Grauer Salzton***: 5 - 17 **Fordon Evaporites***: 222 - 276 (base not proven)
				Kirkham Abbey Formation (Evans,2008)	No description available.	Unknown
		ZG1	**ZG1 Halite**	Zechstein Group	**Hayden Anhydrite**: From Evans (2008); no description available.	Unknown
			Lower Magnesium Limestone	Cadeby Formation	**Cadeby Formation**: From Evans (2008); no description available.	Strata anticipated to increase in thickness westwards.

* Data from Atwick borehole logs.

The detailed description of the geological formations that characterise the Atwick and Aldbrough sites in East Yorkshire are given below:

Glacial Till

The Glacial Till consists mainly of clayey and/or silty matrix with occasional sand and gravel-rich intercalations. Gravel-sized rock fragments are mainly chalk and limestone. The occurrences of these fragments increase towards the base of the unit.

The base of the Glacial Till is determined in the Atwick well logs by a significant drop in gamma ray values at the transition to the underlying limestone of the Chalk Group; the approximate thickness of the Glacial Till varies from 30 m to 35 m.

Chalk Group

The Chalk Group is dominated by relatively well indurated chalky and marly limestones which contain abundant flint nodules especially in the upper part. The Chalk Group is estimated to vary in thickness between 506 m and 526 m.

The limestone of the Chalk Group has significant porosity and permeability and, regionally, is an important aquifer in Yorkshire. Groundwater is contained in major fractures as well as small fissures and in the matrix (Allen et al, 1997).

From available borehole data, four main units can be identified within the chalk.

1. The first unit is approximately 340 m and dominated by white, firm, chalky and earthy textured limestones. Soft, white, marly limestones are also common, particularly in the middle part of the unit; occasional bands of flint are noted within the upper 7 m of the unit.
2. The second unit is approximately 130 m thick and is similar to the first unit with the exception that marly limestones are rare and there are occasional beds of hard, white, microcrystalline limestones; including frequent layers of flint, decreasing within the lower 25 m of the unit.
3. The third unit is approximately 20 m thick; layers of flint are recorded within this unit and colour is described as pinkish becoming red towards the base.
4. The base unit is approximately 10 m thick and comprises pebbly sandstones and red, slightly glauconitic chalk. The sandstones vary in texture from very fine to medium grained with occasional thin grey/green and black shale beds.

Lias Group

The lithology of the Lias Group predominantly consists of well bedded calcareous and silty mudstone and argillaceous limestone; approximate thickness of the unit varies from 15 m to 30 m. The lower boundary is characterised by a lithological change from argillaceous limestone and mudstone to the mudstones of the underlying Penarth Group.

Penarth Group

The Penarth Group consists of silty shale with limonite nodules and thin intercalations of argillaceous limestone and sandstone. The unit can be subdivided into a lower and upper part using the criterion of an abrupt decrease in gamma ray values and an increase in sonic velocity, where the log pattern corresponds to a lithological change from mudstone in the upper part to shale with some thin limestone and siltstone intercalations in the lower part. The Penarth Group shows constant thickness from approximately 15 m to 17 m. Its lower boundary is marked by a change from shales and thin sandstone beds to the thick mudstone deposits of the Mercia Mudstone Group.

Mercia Mudstone Group

The Mercia Mudstone Group is dominated by argillaceous lithologies but includes three main intervals of bedded evaporites, i.e. (from top to bottom) the Keuper Evaporite Member, the Muschelkalk Evaporite

Member and the Röt Evaporite Member. In the electric logs, the evaporite levels typically show low gamma ray values and high sonic velocities representative of anhydrite with sudden changes in both signals across their upper and lower boundaries (i.e. a 'blocky' log signature). Narrow peaks of high gamma ray and decreased sonic velocity thereby correspond to intercalated mudstone beds.

The topmost part of the Mercia Mudstone Group above the upper evaporitic level, the Keuper Evaporite Member, consists mainly of shale interbedded with argillaceous siltstone. The Keuper Evaporite Member is characterised by shale with anhydrite stringers. Below, the section comprises shale with rare stringers of hard dolomite. The Muschelkalk Evaporite Member consists of shale and anhydrite. Further downsection, the lithology is characterised by shale and more frequent intercalations of dolomite. The Röt Evaporite Member lithologically resembles the Keuper and Muschelkalk Evaporite Member. The lowermost part of the Mercia Mudstone Group is dominated by claystone with occasional thin intercalations of fine-grained and argillaceous sandstone. The total thickness of the Mercia Mudstone Group varies between approximately 295 m and 323 m.

The base of the Mercia Mudstone Group is characterised by a strong decrease in gamma ray values due to the decrease in clay content. This log signature reflects the abrupt transition from mudstone to sandstone across the unconformable boundary to the underlying Sherwood Sandstone Group.

From available borehole data, four main units can be identified within the Mercia Mudstone.

1. The first unit is approximately 28 m thick and comprises soft, pale grey/green and red shales becoming red silty shales and red argillaceous siltstones in the lower part of the unit.
2. The second unit is approximately 105 m thick predominately comprises red, occasionally silty shales, together with frequent beds of grey shales, often containing blebs and stringers of anhydrite. The borehole data records rare inter-beds of hard, argillaceous red sandstones.
3. The third unit is approximately 170 m thick and comprises red and grey shales, with stringers of anhydrite. The borehole data records the presence of thin beds of pale grey, dense crystalline dolomite.

Sherwood Sandstone Group

The Sherwood Sandstone Group of eastern England is characterised by fining-upwards sequences of cross-stratified predominantly fine-grained or occasionally medium-grained sandstones representing in-channel deposits of a braided river system and occasional mudstone interbeds that may represent slack water or over bank deposits (Pokar et al, 2006 and Hounslow & Ruffell, 2006). Hounslow & Ruffell (2006) states that close to the English coast the Sherwood is described as a generally coarsening-up unit, a trend which is also seen in the Atwick well logs.

The total thickness of the Sherwood Sandstone Group at Atwick varies between approximately 514 m and 529 m. In the upper two thirds of the unit, the Sherwood Sandstone Group comprises well-sorted, fine to medium-grained sandstone with occasional intercalations of fine-grained, poorly sorted argillaceous sandstone. Gamma ray and sonic velocity log signatures suggest the presence of a couple of individual coarser-grained sandstone beds at the very top of the unit. Finer-grained and more argillaceous sandstones with bedding-parallel clay drapes and intercalated shale beds occur more frequency towards the base of the unit. Especially in its lower third, the Sherwood Sandstone Group is characterised by the common occurrence of shale beds, three of which (each approximately 0.5 m thick) are shown to correlate between all Atwick wells. Stringers of anhydrite are also frequently in the lower part of the unit.

Eskdale Group

The Eskdale Group consists mainly of sandstone and shale, the latter becoming more dominant with depth; additionally, stringers of anhydrite frequently occur. In the area, sandstone and silty mudstone is characteristic for the Amethyst Member at the top of the Eskdale Group. The Bröckelschiefer Member

at the base of the unit comprises silty, anhydritic mudstone intercalated with siltstone. The thickness of the Eskdale Group varies between approximately 90 m and 95 m.

The base of the Eskdale Group is characterised by a sharp lithological change to the evaporitic sequence of the underlying Zechstein Group, with a sudden drop in gamma-ray values and an increase in sonic velocity across the boundary.

Zechstein Group

The Zechstein Group as a whole comprises the four cyclical Upper Permian carbonate-evaporite successions. The Zechstein Group of the East Yorkshire area can be subdivided into a number of units, applying Eastern England and Southern North Sea stratigraphic schemes, but also by analogy with the well-known Zechstein sequences of the Netherlands and Germany.

The ZG4 cycle, which is a succession of shale, anhydrite, siltstone and rock salt up to 59 m thick at Atwick, contains the 15 m thick relatively pure salt interval of the ZG4 Halite and the up to 20 m thick Red Salt Clay.

The ZG3 cycle of 100 m to 112 m thickness consists largely of shale, dolomite, anhydrite and rock salt. It includes the up to 20 m thick relatively pure salt interval of the ZG3 Halite and the Upper Magnesium Limestone. The Upper Magnesium Limestone, which attains a thickness of 60 m at Atwick, is characterised by the occurrence of slightly calcareous and anhydrite dolomite; in its lower part, the dolomitised packstones become more argillaceous and crystalline.

Evans & Holloway (2009) state that in Yorkshire, the ZG2 Fordon Evaporites generally contain a thick halite succession, where caverns have been created in the ZG2 salts between 1,710 m and 1,840 m depth. Furthermore, in the surrounding area the Fordon Evaporites are about 280 m thick, with the top at around 1,660 m below ground level and the base a *c.* 1,940 m.

Alternatively, Evans & Kirk (2013) highlight areas where the generalised depth to the top Fordon Evaporites are similar to the main ZG2 halite unit of similar depth (approximately 1,400 m) and thickness (approximately 150 m to 200 m) to the halite beds in the area.

A.2.2. Teesside

Evans & Holloway (2009) state that the halite-bearing strata of Permian age, lie concealed at depth beneath much of eastern England, from Teesside southwards though Yorkshire (including the Atwick and Aldbrough sites) into northern Lincolnshire. These halite beds form part of the Zechstein Group; as recorded in East Yorkshire.

Correspondingly, the Zechstein Group comprises formations interbedded with thick dolomite, mudstone and anhydrite formations in five cycles (ZG1-ZG5) as shown in Figures A2-1 and A2-2.

A.2.2.1. Regional geological framework

In the north east of England, the search of water near Middlesbrough in 1859, led to the discovery, beneath about 220 m of Sherwood Sandstone, of the Teesside province of the Permian salt field; where it is formed by the (Middle or Main) Boulby Halite Formation (ZG3) overlying the Billingham Main Anhydrite (Evans & Holloway, 2009).

Furthermore, Evans & Holloway (2009) indicate that small caverns were developed at Saltholme north of the river Tees and Wilton to the south (Cooper, 2002); at this location the halite varies in thickness between 30 m and 45 m, and lies at depths between 274 m and 366 m.

At the North Tees salt cavern storage facility located in Saltholme the halite is approximately 340 m below the surface and varies in thicknesses between 27 m and 40 m.

At the Wilton underground storage facility solution-mined caverns were developed in salt beneath a

cover of Mercia Mudstone Group and Sherwood Sandstone Group strata approximately 650 m below the surface in salt of approximately the same thickness as at Saltholme (Evans & Holloway, 2009).

The geology in the Teesside region is characterised by three distinct geological sequences: Quaternary Deposits, Permo-Triassic Red Beds and Zechstein Evaporites.

A.2.2.2. Site stratigraphy

North Tees Site

Based on the borehole log information provided by the operator (SABIC) the North Tees site stratigraphy is as shown in Table A2-2; general descriptions of the strata are provided in the following sections.

It should be noted that examination of the available borehole logs confirmed the subdivision of the ZG3 Boulby Halite into the layers of Upper Main Salt, Honeycomb Anhydrite and Lower Main Salt.

Table A2-2: Idealised average stratigraphic column for the North Tees site

Geological Formation	Depth at the top of formation [m bgl]	Thickness of formation [m]
Quaternary deposits	0.0	27.5
Sherwood Sandstone	27.5	219.8
Roxby Formation	247.4	84.1
ZG4 Sherburn Anhydrite	331.4	2.9
ZG4 Carnallitic Marl	334.3	7.0
ZG3 Boulby Halite	341.3	32.7
ZG3 Billingham Anhydrite	374.0	8.0
ZG3 Brotherton Formation	382.0	30.0
Aislaby Group	412.0	Drilling terminated

Quaternary deposits

The quaternary deposits are identified as Glacial Till which overlies the bedrock at the site, described as brown boulder clay, brown sandy clay, stony clay with basal sand and gravel.

Permo-Triassic Red Beds

The Permo-Triassic Red Beds comprise the Sherwood Sandstone (Triassic) and Roxby Formation (Upper Permian):

- Sherwood Sandstone (Triassic)

  The Sherwood Sandstone (formerly known as the Bunter Sandstone) including red sandstones, uniform in the upper 170 m and interbedded with increasing proportions of red mudstones and siltstones in the lower 100 m, the latter usually described as ‘Transition Beds’.

- Roxby Formation (Upper Permian)

  The Roxby Formation (also known as Upper Marl, Saliferous Marl or Upper Permian Marl) is about 80 m thick on average and consists largely of mudstone and siltstone, reddish brown, with subordinate sandstone. It includes a 7 m and 9 m siltstone bed at its base and generally sulphates (e.g. gypsum and anhydrite) are common towards its base.

Zechstein Evaporites

The Zechstein Evaporites comprising:

- ZG4 Sherburn Anhydrite (Permian)

  The Sherburn Anhydrite (also known as Upper Anhydrite) comprises an upper sulphate unit and a lower sulphate unit separated by a dolomitic middle unit with a characteristic texture of a dolomite network enclosing anhydrite. Commonly is a coarse, grey to buff or pink finely crystalline anhydrite rock, distinguished by the presence of many courses of upright-fibrous pseudomorphs (in anhydrite, halite or sylvite) that follow an early gypsum deposition. The formation is typified by abundant uneven laminae of dolomite or magnesite and evidence of cross-lamination is fairly common in its upper parts.

- ZG4 Carnallitic Marl (Permian)

  The Carnallitic Marl (also known locally as Rotten Marl) comprises a red-brown silty mudstone with its upper part generally salt free except for secondary veins of halite filling contraction joints. Interbedded halite increases with depth and in the lower part of the formation a distinctive unit of anhydritic mudstone can be distinguished, forming a bedded network enclosing finely disseminated halite.

- ZG3 Boulby Halite – Upper Main Salt (Permian)

  The Upper Main Salt belongs to the ZG3 Evaporite group and is a medium to coarse halite, red in the upper part with mudstone and anhydrite impurities and grey in lower part with anhydrite impurities. The insoluble impurities in the Upper Main Salt range approximately between 10% and 15% and are found in the form of relict fragments and bands of mudstone and anhydrite.

- ZG3 Boulby Halite – Honeycomb Anhydrite (Permian)

  The Honeycomb Anhydrite is a mottled light grey and fawn halitic anhydrite with basal shale containing up to 25% disseminated halite. In the uppermost horizon this formation commonly occurs with approximately 15% pale grey halite distributed in the form of distinctive ‘herring-bone texture’. In the lower part of this formation the halite is encountered as disseminated inclusions and irregular stringers.

- ZG3 Boulby Halite – Lower Main Salt (Permian)

  The Lower Main Salt is coarse grained grey to fawn, transparent halite containing variable amounts of anhydrite interbeds and anhydritic shale showing gradation from herringbone textured top to bedded shaley base.

- ZG3 Billingham Anhydrite - Main Anhydrite (Permian)

  The Billingham Anhydrite also known as Main Anhydrite is a light and dark grey mottled, slightly dolomitic, nodular with shaley interstices bedded formation. The formation constitutes the floor of the salt caverns and normally not drilled for more than few metres.

- ZG3 Brotherton Formation – Upper Magnesium Limestone (Permian)

  The Brotherton Formation also known as Upper Magnesian Limestone is a dolomitic limestone, grey with innumerable fossil remains of algae Calcinema permiana on some bedding planes confirming Permian Zechstein age (i.e. 248 - 256 million years ago). Lower beds are said to be of dolomite, while higher beds are of grey uniformly fine-grained thin-bedded limestone. Small-scale sedimentary

structures, especially ripple marks, are abundant at many levels.

- Aislaby Group

Comprising Dolomite and Concretionary Limestone.

Wilton Site

Based on the borehole log data available from Phillips (1976) an idealised average stratigraphy is shown in Table A2-3; general descriptions of the strata are provided in the following sections.

A fault zone was recorded at the Wilton site, as detailed in Philips (1976), described as fault gouge where units are recorded as dipping at 45° and described as white, sugary and friable banded gypsum underlain by dark grey fine grained flinty anhydrite of Main Anhydrite (ZG3 Billingham Anhydrite) with rolled contorted and lineated with flakes and schlieren of white anhydrite, dark grey shale and a little dolomite; this is in turn underlain by white, sugary and friable banded gypsum.

Table A2-3: Idealised average stratigraphic column for the Wilton site

Geological formation	Typical depth at the top of formation [m bgl]	Typical thickness of formation [m]
Drift	0	16
Lower Lias	16	88
Rhaetic (Rhaetian age)	104	12
Keuper Marl	116	206
Bunter Sandstone (Sherwood Sandstone)	322	248
Saliferous Marl (Roxby Formation)	570	76
Upper Anhydrite (ZG4 Sherburn Anhydrite)	646	3
Carnallitic Marl (ZG4 Rotten Marl)	650	9
Upper Main Salt (ZG3 Boulby Halite)	659	33
Honeycomb (ZG3 Boulby Halite)	692	5
Lower Main Salt (ZG3 Boulby Halite)	697	5
Main Anhydrite (ZG3 Billingham Anhydrite)	702	Not proven

Drift deposits

The drift deposits are identified predominantly as brown boulder clay (i.e. Glacial Till) overlain by brown sandy clay and fine gravel with clay.

Lower Lias

The Lower Lias is described as dark grey, thin bedded limey shales including beds of silty micaceous shale, siltstone bands and limestone nodules. Layers of dark grey glauconitic sandstone and pyrite are recorded.

Rhaetian age deposits

The Rhaetic deposits are recorded as light grey soapy shale underlain by dark grey to black splintery shale and very pyritic with interbedded glauconitic siltstones and sandstones.

Keuper Marl

The Keuper Marl is identified as light grey-green ‘Tea Green’ marls underlain by gypsum beds, red brown marl and silty mudstone with occasional beds of grey green siltstone. Upper and lower gypsum zones are recorded. Near the base of the Keuper Marl is a well-defined bed of dark grey anhydrite and the base of Keuper Marl is clearly marked by a change from red sandstone to light red, often friable sandstones.

Bunter Sandstone (Sherwood Sandstone)

The Bunter Sandstone, also known as Sherwood Sandstone, is recorded as fine, medium and coarse grained red sandstone with marl bands; where siltstone and mudstone is noted in the lower part of the stratum.

Saliferous Marl (Roxby Formation)

The Saliferous Marl, also known at the Roxby Formation, is identified as red and brown marl in the upper parts of the stratum and red brown siltstone in the lower parts.

Upper Anhydrite (ZG4 Sherburn Anhydrite)

The Upper Anhydrite, also known as the Sherburn Anhydrite, is recorded as pale grey to colourless and pink to white translucent, fine and medium grained crystalline anhydrite. Borehole log data records indicate an Upper Sulphate Unit, Middle Dolomitic Unit and Lower Sulphate Unit, however, these were not encountered at all locations.

Carnallitic Marl (ZG4 Rotten Marl)

Carnallitic Marl, also known as Rotten Marl, is identified as massive red marl with occasional slightly halitic bands and secondary salt veins. The base of the stratum was recorded as Marl Honeycomb and described as marl with salt transition beds.

Upper Main Salt (ZG3 Boulby Halite)

The Upper Main Salt, part of the Boulby Halite formation, is recorded as medium, course and very coarse grained colourless to fawn and pink to grey halite with red marl and mudstone inclusions and a few bands of anhydritic stringers and inclusions. A 'False Honeycomb' herringbone textured mixture of anhydrite and halite is recorded at the base of the stratum.

Honeycomb (ZG3 Boulby Halite)

The 'Honeycomb' as described in Phillips (1976), part of the Boulby Halite formation, is identified as medium grained light grey banded anhydrite with herringbone intergrowth of anhydrite and halite. A Basal Shale unit composed of dark grey shale and pink and white anhydrite was recorded at the base of the stratum.

Lower Main Salt (ZG3 Boulby Halite)

The Lower Main Salt, part of the Boulby Halite formation, is recorded as grey to fawn halite with interbeds of anhydrite and anhydritic shale units.

Main Anhydrite (ZG3 Billingham Anhydrite)

Information with respect to the Main Anhydrite from Phillips (1976), also known as Billingham Anhydrite, is limited, where recorded it is described as light grey, medium grey and dark grey mottled, nodular and fragmental anhydrite.

A.2.3. Cheshire

Beutel & Black (2004) indicate that the Cheshire salt field has a history of exploitation, growing from its first pre-Roman development around the salt springs into major industry. It is understood that the salt settlement occurred during the Triassic Age approximately 230 million years ago, where the salt was deposited in a semi-arid environment within mainly fault-controlled, land-locked basins linked to the major depositional centres of the North Sea and Irish Sea (Beutel & Black, 2004).

A.2.3.1. Regional geological framework

In the Cheshire Basin, the major Triassic beds are located within two formations: Wilkesley Halite Formation (Upper Saliferous Beds) and the Northwich Halite Formation (Lower Saliferous Beds) (Bell, 1992). The Mercia Mudstone Group in the Cheshire Basin is almost entirely concealed beneath thick glacial deposits (Evans & Holloway, 2012); refer to Figure A2-3 for an illustration of the likely geological conditions of the Cheshire Basin. It is important to clarify that the existing Stublach and the Holford salt cavern sites, which have been developed by different operators, share the same geological framework.

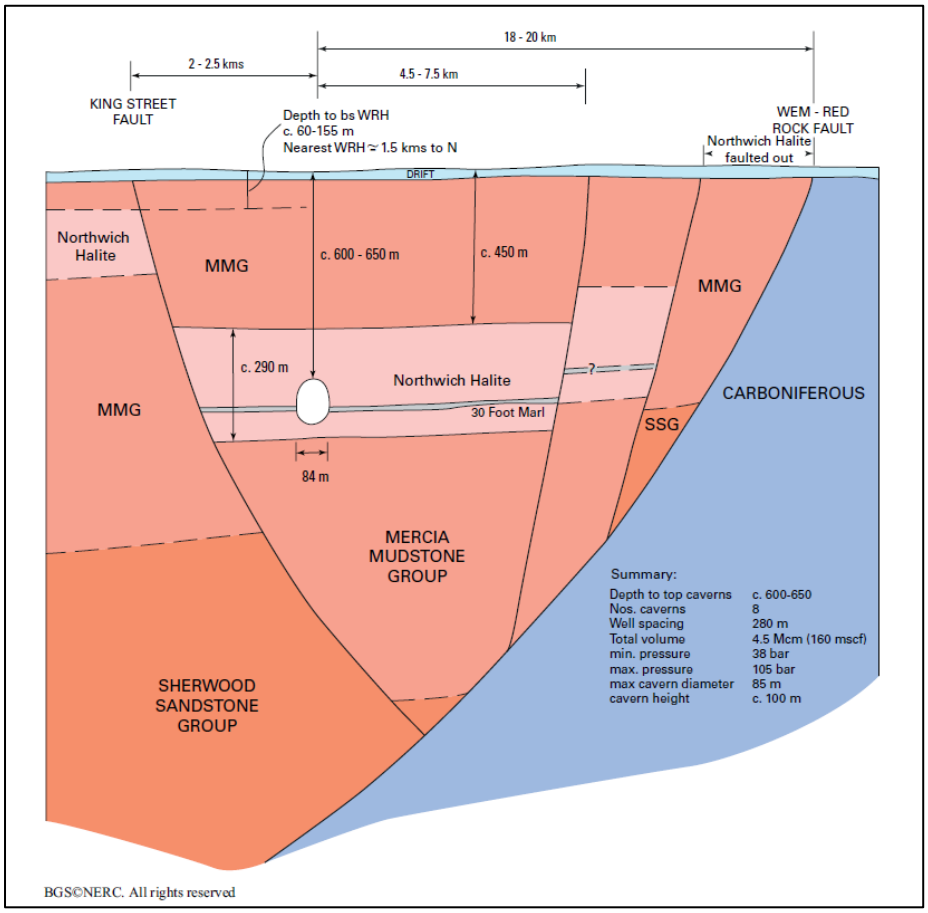

Figure A2-3: Sketch section illustrating the geology likely to represent the conditions encountered in the Cheshire Basin (Evans, 2008)

A.2.3.2. Regional structural geology

In general, the Mercia Mudstone Formation has been subject to only mild tectonic deformation. However, in Cheshire, larger faults affect the Group and are understood to be the reactivation of earlier Carboniferous structures (Hobbs et al, 2002). Regional faulting in the Cheshire district trends from NE to SW in the south and NNW to SSE in the North.

The presence of faulting has largely been inferred from borehole and seismic data. Where exposure is available it tends to be of minor faults in the mid Cheshire hills. Several of these faults are thrown down to the west, a direction which is antithetic to the main faults which bound the western Cheshire graben. These faults are reported to be contemporaneous to the main faulting and are thought to have relieved stress following rupture along the main fault (Earp & Taylor, 1986).

The faults that define the Cheshire Basin are interpreted by the British Geological Survey (Earp & Taylor, 1986) to have been active during the deposition of the Mercia Mudstone Group, suggesting the Cheshire basin was subsiding throughout the deposition of Mercia mudstone Group (Hobbs et al, 2002).

The regional dip of the stratigraphy is in the range of 5° to 7° towards the South West (Evans & Hough, 2009). However, the maximum local dip inferred from the available borehole records is 3° toward the South East, which is in agreement with the geological memoir (Earp & Taylor, 1986).

A.2.3.3. Site stratigraphy

Based on the sources of geological information from Earp &Taylor (1986), Hobbs et al (2002), Howard et al (2008) and Evans (2008); the generalised geological succession anticipated in the Cheshire Basin

is presented in Table A2-4.

Table A2-4: Generalised geological stratigraphy for Cheshire

Sub era	Group	Formation/ member		Former name	Typical description	Maximum thickness [m]
Quaternary		Glacial Till		Not applicable	Red and grey gravelly sandy clay (superficial or 'drift' deposits)	5 - 92
Triassic	Mercia Mudstone Group	Branscombe Mudstone Formation		Brooks Mill Mudstone; Upper Keuper Marl	Red blocky mudstone	Variable/ Not present in some locations
		Sidmouth Mudstone Formation	Wilkesley Halite Member	Upper Keuper Saliferous Beds	Halite with thin red mudstone partings	100
			Sidmouth Mudstone (above) Member	Byley & Wych Mudstone; Middle Keuper Mark; Eldersfield Mudstone	Red blocky mudstone. Rhythmic alternations of red and green-grey mudstone and siltstone in the lower part; mostly red-brown silty mudstone with anhydrite nodules above.	580
			Northwich Halite Member[1]	Lower Keuper Saliferous Beds	Halite and mudstone. Alternations of thick beds of halite and thin intervals of mudstone.	290
			Sidmouth Mudstone (below) Member	Bollin Mudstone; Lower Keuper Marl	Red blocky mudstone. Alternations of siltstone and structureless mudstone in lower part, the latter dominantly above; an intercalation of siltstones and sandstones c. 100 m above base, and thin beds of halite near top; gypsum nodules throughout.	260 - 460
			Tarporley Siltstone Member	Waterstones	Ripple laminated siltstone with local sandstone	20 - 250
	Sherwood Sandstone Group	Helsby Sandstone Formation		Keuper Sandstone	Sandstone and pebbley sandstone	20 - 200

*It should be noted that the Northwich Halite Member comprises up to 10.8 m thick 'Thirty foot' Marl (Evans, 2008).

The detailed description of the geological formations that characterise the Cheshire Basin are given below:

Quaternary Deposits

Glacial Till is known to overlie bedrock; Evans & Hough (2005) describe the Glacial Till as a red and grey gravely and sandy clay.

Sidmouth Mudstone (above Northwich Halite) Member

The Sidmouth Mudstone, formerly the 'Middle Keuper Marl', is a sedimentary sequence of red, reddish grey and greenish grey mudstone and siltstone. Its sedimentary structure is strongly influenced by its depositional conditions and varies between thin laminae to a blocky or an unstructured form. The sequence contains anhydrite ($CaSO_4$) nodules and gypsum ($CaSO_4 \cdot 2H_2O$) veins. Dolomite ($CaMg(CO_3)$) is distributed widely and helps to cement siltstone laminae.

The formation is typically described within the borehole records as red, green and grey marl and laminated siltstones, although detailed descriptions are limited. A number of the borehole records describe veins and layers of gypsum, anhydrite and occasionally rock salt (Halite) within the marl.

Northwich Halite Member

The Northwich Halite Member was formerly known as the Keuper Saliferous beds. It is a sequence of halite (NaCl) with three named beds at the lower part of the formation: The Top Bed (halite sequence), the 'Thirty Foot' Marl (marl) and the Bottom Bed (thin halite sequence). The total thickness of the Northwich Halite Member at the site is in the region of 220 m – 230 m.

The Northwich Halite Member also comprises a number of alternating mudstone layers which contain layers of halite and halite that contains layers of mudstone. Where such sequences are described for a thickness of > 5 m then they are commonly termed Salt/Marl.

Within the Northwich Halite Member, Halite is the dominant mineral but marl (clay and silt) are distributed throughout and account for around 24% of the sequence (Earp & Taylor, 1986). Other impurities are derived from gypsum ($CaSO_4$) and dolomite.

The 'Thirty Foot' Marl, a marl layer, approximately 10m thick divides the Top and Bottom Beds.

The Bottom Bed was historically the main source of rock salt and has yielded up to 95% Sodium Chloride (NaCl) within the extracted brine solution. The bottom bed varies between 25 m to 30 m in thickness and was termed the 'Hundred Foot Salt' in historical literature.

Sidmouth Mudstone (below Northwich Halite) Member

The Sidmouth Mudstone (below) was formerly known as the 'Lower Keuper Marl'. It is similar in nature to the overlying Sidmouth Mudstone, being a sequence of mudstone and siltstone. It also contains many of the same lithological elements present in the underlying Tarporley Siltstones, albeit with a greater proportion of mudstones higher up within the formation.

The upper layers of the formation are characterised by unstructured silty mudstone which contains layers of halite. The lower parts of the formation are dominated by a laminated siltstone and mudstone which are interbedded with the unstructured mudstone. These lithologies are known as known locally as facies A and B respectively.

A.3. Representative cavern details

To successfully carry out the geomechanical analysis of hydrogen storage caverns, the undertaken modelling will employ caverns that conform to the representative configurations encountered in the cavern storage fields identified in the areas of East Yorkshire, Teesside and Cheshire.

For this reason, and in consultation with the operators of the existing salt cavern storage facilities, a representative typical cavern has been identified from each of the three halite-bearing strata namely the East Yorkshire, the Teesside and the Cheshire salt fields.

The criteria that were used in selecting each representative salt caverns included, *inter alia*, the following:

- Geology/stratigraphy of the area,
- Storage capacity of the cavern,
- Geomechanical characteristics of the cavern,
- The particulars and the integrity of the cemented casings and well completion of the well(s), and
- The history of the cavern, both in terms of development and storage operations.

The representative cavern for East Yorkshire is part of the Atwick cluster of salt caverns which is currently operated by SSE Gas Storage who have provided to Atkins access to all the required technical data. Currently in East Yorkshire there are in operation nine caverns in the Atwick site and nine caverns in the Aldbrough site. These caverns have been developed at a depth of approximately 1,800 m below ground level (bgl), with an average volume of approximately 250,000 m^3, and they have the potential to be converted from natural gas storage to hydrogen mixture storage. In addition, plans exist to develop new storage caverns as part of the so called Aldbrough Phase 2 project.

The representative cavern for Teesside is part of the Wilton cluster of salt caverns which is currently operated by SABIC who have provided to Atkins access to all the required technical data. Currently, the Wilton site comprises eight solution mined caverns with an average volume of 43,200 m^3 that have been developed at a depth of approximately 650 m bgl, and are operated by employing the wet-storage technique. Only five of them are currently used for storage purposes, but plans exist to develop in the Wilton site two new storage caverns each with a capacity of 50,000 m^3.

The representative cavern for Cheshire is part of the Stublach cluster of salt caverns which is currently operated by Storengy who have provided to Atkins access to all the required technical data. Storengy have plans to develop 20 storage caverns which are currently being brought progressively into operation. The total storage capacity will eventually reach 400 million cubic metres.

Additionally, details of the storage caverns that are currently in the planning process were provided by Inovyn who is the operator of the Holford salt cavern field in Cheshire. Inovyn is planning the development of 19 salt caverns designed to store a working gas volume of approximately 500 million cubic metres of natural gas.

In the geomechanical modelling of the caverns, a plane strain analysis approach will be adopted for the assessment of the stability of the investigated caverns. The axisymmetric approach is not providing a full three-dimensional appreciation of the stresses around caverns, such as those encountered in actual salt caverns, because it employs the averaged radii and as such it ignores the geometrical irregularities of the caverns' walls. Use of the plane strain method to model cavern behaviour allows flexibility in modelling the dip of the geologic features and cavern irregularities which are considered to be significant structural attributes. Moreover, experience from previous investigations carried out in operational gas storage salt caverns, established that the two-dimensional modelling overestimates marginally the equivalent three-dimensional analysis stresses and therefore the plane strain analysis provides an inherent factor of safety. Therefore, the use of the plane strain method to model cavern behaviour is considered to be acceptable and although this approach is prone to marginally over predicting stresses and displacements, it allows flexibility in modelling the cavern irregularities which are considered to be significant structural features.

During the plane strain analysis of the caverns use will be made of the available sonar surveys, which have been provided by the operators, to identify the most unfavourable cavern cross section (from the point of view of irregularities in the geometry and stress concentrations) that will be used in the geomechanical modelling.

A.3.1. East Yorkshire

A.3.1.1. Geometrical characteristics

The well that was used during the development of the representative cavern is vertical. A 13⅜" intermediate casing string was cemented in place with the casing shoe set at a depth of 553 m bgl. A 9⅝" production casing string was cemented in place with its casing shoe, the wells last cemented casing shoe (LCCS) is set at a depth of 1,717 m bgl. The most recent sonar survey in brine was conducted by Socon on 8 November 2011. The following geometrical details were identified:

- Volume, 275,691 m^3;
- Top of cavern, at 1,722.0 m bgl;
- Bottom of cavern, at 1,826.1 m bgl;
- Bottom of the cavern along the axis on the well, at 1,825.5 m bgl;
- Maximum mean radius, 37.6 m at 1,818 m bgl; and
- Maximum local radius, 46.7 m at 1,821.7 m bgl and azimuth 210°.

The mean radius of the cavern is satisfactorily close to target shape and the upper part of the cavern shape (at the depth range of 1,725 m bgl to 1,750 m bgl) is very regular. The identified shape irregularities in the upper part of the cavern may be attributed to the localised differences in the solubility of the Main Salt during the solution mining operations. The three-dimensional configuration of the East Yorkshire representative cavern is shown in Figure A3-1

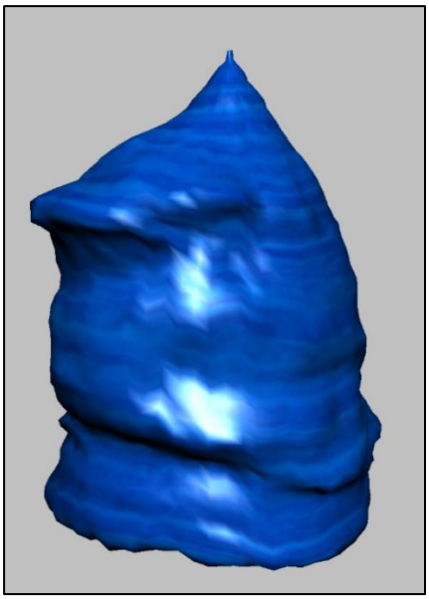

Figure A3-1: Perspective view of the representative cavern in East Yorkshire

A.3.1.2. Operating pressures

The gas storage caverns at East Yorkshire operate with daily movements of natural gas superimposed on a seasonal filling and emptying cycle.

At the last cemented casing shoe, the normal operating range employs a maximum pressure of 271 barg and a minimum pressure of 120 barg. Moreover, in conformance with the specifications provided by the

East Yorkshire operators, the injection and withdrawal rate in the production tubing is maintained below 20 bar/d.

A.3.2. Teesside

A.3.2.1. Geometrical characteristics

The well that was used during the development of the representative cavern is vertical. The well was constructed in the 1965 by drilling a 23" hole between 15 m bgl and 20 m bgl into the Lower Liassic Shales formation and running/cementing an 18" conductor in place. The next 17½" borehole section was drilled to just above or just into the Sherwood Sandstone bed at approximately 310 m bgl and a 13⅜" casing string was cemented in place. The final 12¼" section was drilled into the ZG3 Boulby Halite - Upper Main Salt (Permian) bed at approximately 620 m bgl. A 9⅝" casing string was cemented in place with the casing shoe set just above or just into the top of the salt section.

The most recent sonar survey in brine was conducted by Socon on 30 September 2011. The following geometrical details were identified:

- Volume, 51,144 m^3;
- Top of cavern, at 647.0 m bgl;
- Bottom of cavern, at 668.1 m bgl;
- Bottom of the cavern along the axis on the well, at 668.1 m bgl;
- Maximum mean radius, 38.6 m at 654.0 m bgl; and
- Maximum local radius, 42.4 m at 654.0 m bgl and azimuth 75°.

The three-dimensional configuration of the Teesside representative cavern is shown in Figure A3-2

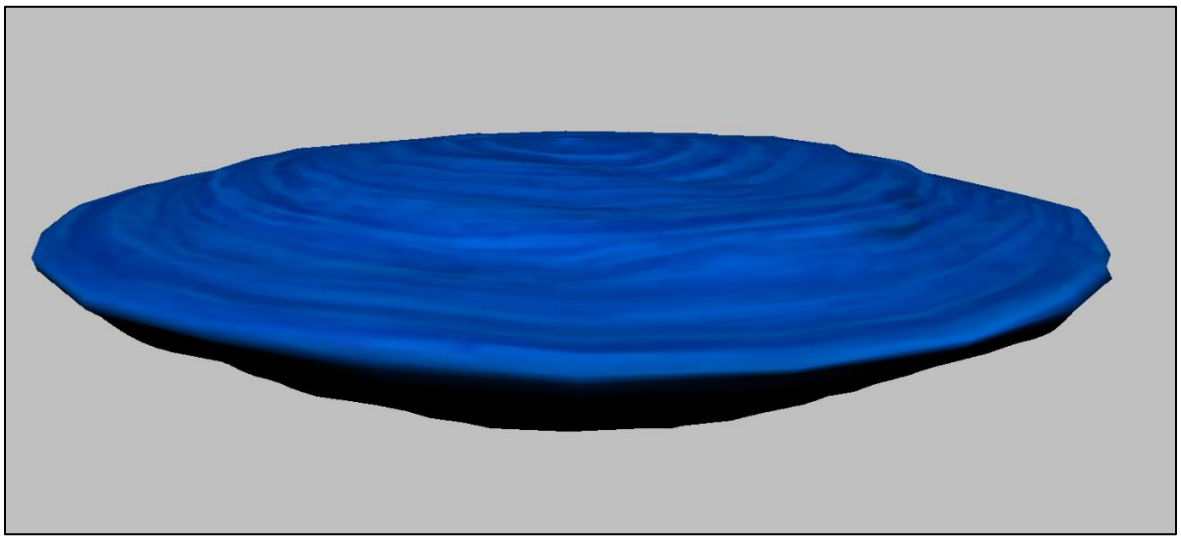

Figure A3-2: Perspective view of Teesside representative cavern

A.3.2.2. Operating pressures

The storage caverns at Teesside function as wet storage facilities and operate by brine displacement; therefore they are subjected continuously to a nearly constant internal pressure that corresponds to the full brine head also known as halmostatic pressure.

The normal cavern pressure conditions are consistent with a pressure maintained by the full head of brine characterised by a density of 1.205 Mg/m3. As a result the caverns' internal pressure corresponds to a hydrostatic loading, acting normal to the cavern's boundary, equivalent to a gradient of 0.0118 MPa/m (= 9.81 × 1.205 / 1000) resulting in an approximate cavern roof pressure equal to 76.5 barg

A.3.3. Cheshire

A.3.3.1. Geometrical characteristics

The well that was used during the development of the representative cavern in Stublach, Cheshire is vertical. The 17½" section of the well was drilled from 535 m to 668 m bgl and the 13⅜" casing string was run and cemented in place in 15 November 2008 with the last cemented casing shoe set at a depth 535 m bgl.

The most recent sonar survey in brine was conducted by Flodim on 17 April 2014. The following geometrical details were identified:

- Volume, 304,438 m^3;
- Top of cavern, at 547 m bgl;
- Bottom of cavern, at 622.09 m bgl;
- Bottom of the cavern along the axis on the well, at 621.37 m bgl;
- Maximum mean radius, 44.45 m at 581 m bgl; and
- Maximum local radius, 54.55 m at 614 m bgl and 305° azimuth.

The mean radius of the cavern is satisfactorily close to target shape and the upper part of the cavern shape (at the depth range of 547 m bgl to 590 m bgl) is considered to be very regular. The identified irregularities in the lower part of the cavern may be attributed to the non-symmetrical collapse of the 'Thirty Foot' Marl band during the solution mining operations. The three-dimensional configuration of the Stublach representative cavern is shown in Figure A3-3

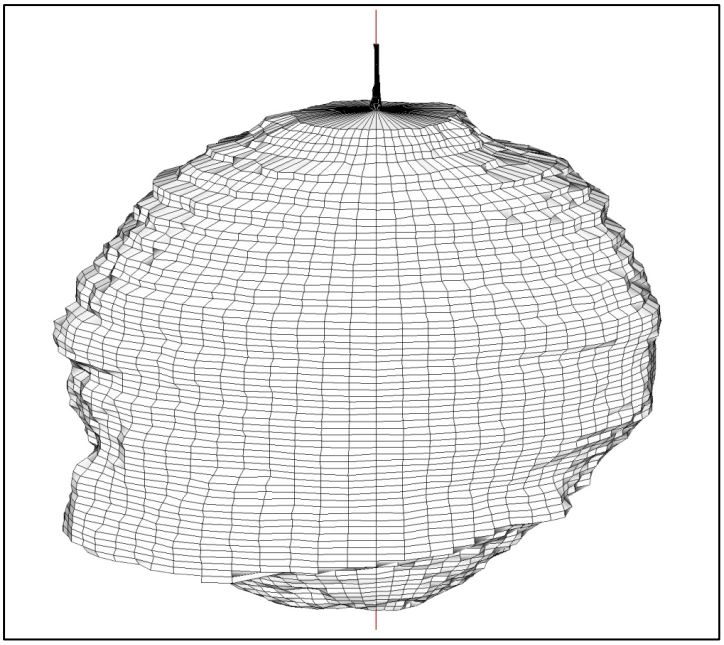

Figure A3-3: Three-dimensional configuration of the Stublach representative cavern, view from west with an overhang of 10°

As a result of the particular geological conditions that exist in Cheshire (i.e. the presence of the 'Thirty Foot' Marl band which is intercalated in the Northwich Halite) an alternative cavern type will also be considered for this particular location. The differences between the Stublach caverns and the proposed Holford caverns are graphically shown in Figure A3-4, where it is shown that the Stublach caverns have been developed with their sump located below the 'Thirty Foot' Marl, while in Holford there is opportunity to develop the caverns with their sump above the 'Thirty Foot' Marl.

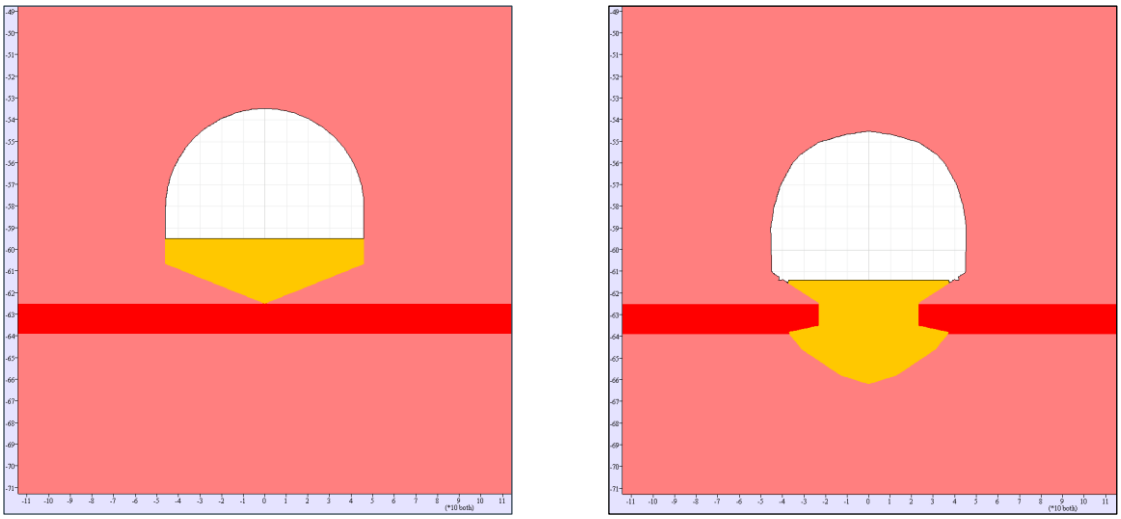

Holford cavern Stublach cavern

Figure A3-4: Comparison between the Holford and Stublach caverns

A.3.3.2. Operating pressures

The caverns at Stublach operate with daily movements of gas superimposed on a seasonal filling and emptying cycle. At the last cemented casing shoe, the maximum operating pressure is 95 barg and the minimum pressure is 30 barg. Moreover, the maximum natural gas velocity in the production tubing is 15 m/s. The reason for the gas velocity limitation provided by the site operator is currently unknown. However, experience suggests a maximum allowable gas velocity of 30 m/s has been shown to be allowable for maximum gas velocities, which will be considered as a constraint for this study.

Typical diagrams of calculated pressure and temperature histories related to natural gas storage operations of the Stublach caverns are shown in Figure A3-5.

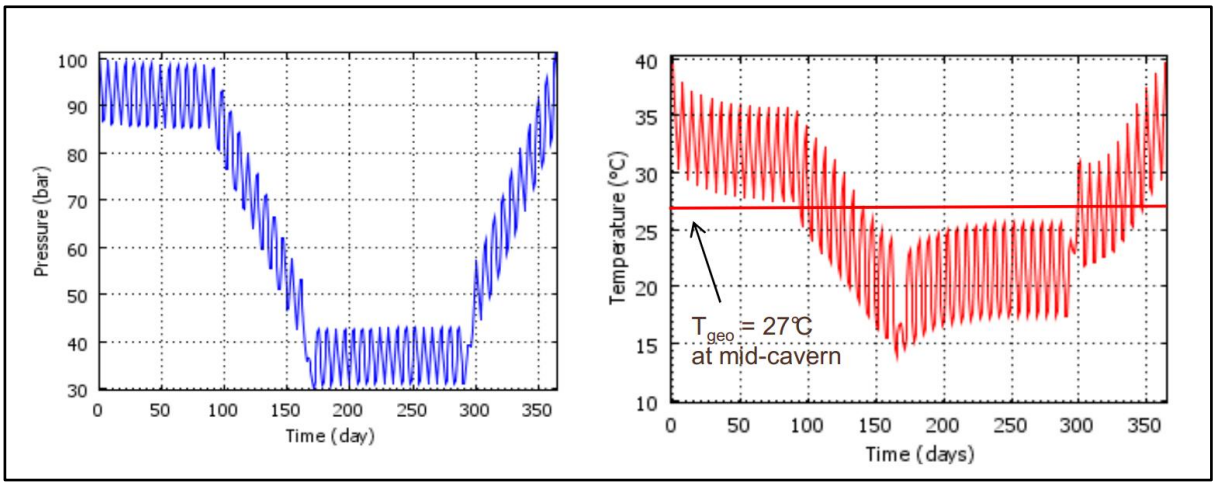

Figure A3-5: Calculated pressure and temperature histories for Stublach caverns resulting from the thermodynamic modelling of the natural gas storage operations (Charnavel, 2012)

A.4. Cavern assessment theory

Reliable estimates of the strength and deformation characteristics of rock masses are required for almost any form of geomechanical analysis needed for the design of salt caverns that are used for storage purposes. The properties of the geological materials that characterise the three identified halite-baring strata areas under investigation (i.e. East Yorkshire, Teesside and Cheshire) have been reviewed and accordingly modelled by employing appropriate rock mechanics analogues ensuring that:

1. the adopted modelling process did not reduce the significance of the critical influence of the constitutive behaviour of the geological materials, and
2. an element of conservatism was introduced, with respect to the different criteria for proof of safety, yet not overly conservative with respect to economics.

In investigating the stability of storage salt caverns, a careful study of the mechanical behaviour of the surrounding rock materials is one of the most important requirements. The relevant characteristics of the associated geological materials have been determined by reviewing and analysing an appropriate number of suitable laboratory tests and, in some cases, by subsequent confirmation from tests carried out *in situ*. After comparing these characteristics with those of an idealised material, appropriate rock mechanics models have been selected to be used in the numerical geomechanical analysis of the salt caverns.

The modelling of the quasi-static material behaviour of the identified geological layers was carried out by employing selectively specific constitutive models. In particular, the Drucker-Prager yield criterion and the Mohr-Coulomb yield function are used accordingly to model the yield response of the geological materials when subjected to shear loading. These particular constitutive models have been selected since they involve a degree of permanent, path-dependent deformations (failure) as a consequence of the nonlinearity of their stress-strain relations.

A.4.1. Geological material models

A.4.1.1. The Mohr-Coulomb failure criterion

Numerous empirical criteria have been developed to describe the onset of yield for geological materials, among those the Mohr-Coulomb yield criterion remains the most popular because it clearly captures and describes both frictional and cohesive strength resistance to shear failure.

The Mohr-Coulomb plasticity model is used for geological materials that yield when subjected to shear loading while the yield stress depends only on the major (σ_1) and minor (σ_3) principal stresses.

All plastic models, including the Mohr-Coulomb model, potentially involve some degree of permanent, path-dependent deformations (failure); a consequence of the nonlinearity of the stress-strain relations. The plastic flow formulation for the Mohr-Coulomb model rests on basic assumptions from plasticity theory that the total strain increment may be decomposed into elastic and plastic parts, with only the elastic part contributing to the stress increment by means of an elastic law (Itasca, 2011). In addition, both plastic and elastic strain increments are taken to be coaxial with the current principal axes of the stresses.

The flow rule used by the Mohr-Coulomb model specifies the direction of the plastic strain increment vector as that normal to the potential surface and is called *associated* if the potential and yield functions coincide, and *non-associated* otherwise. For the Mohr-Coulomb model, a shear yield function and a *non-associated* shear flow rule is used. In addition, the failure envelope is characterised by a tensile yield function with *associated* flow rule.

In the numerical modelling that is implemented for the stress analysis of salt caverns, an *elastic trial* for the stress increment is first computed from the total strain increment using the incremental form of Hooke's law. The corresponding stresses are then evaluated and if they violate the yield criteria (i.e. if

the stress point representation lies above the yield function in the generalised stress space), plastic deformations take place. In this case, only the elastic part of the strain increment can contribute to the stress increment; the latter is corrected by using the plastic flow rule to ensure that the stresses lie on the composite yield function (Itasca, 2011).

The relationships that express mathematically the failure characteristics of the Mohr-Coulomb model are defined below.

In many instances, particularly in salt cavern engineering problems, the response of a geological material after the onset of failure is an important factor in the design of the underground structure under consideration. Consequently, there is a need to incorporate the post-failure response approach for the material models that will be used in the geomechanical modelling of salt caverns.

In the Mohr-Coulomb model this simulation is implemented, the introduction of the residual shear strength parameters (i.e. the residual cohesion c_{res} and the residual angle of shearing resistance φ_{res}) and the dilation parameter N_ψ, that model the shear dilatancy type of post-failure response. These properties are only activated after the onset of failure, as defined by the Mohr-Coulomb relation described by Equation A4-1 below.

Mathematical definition of Mohr-Coulomb failure criterion

The Mohr-Coulomb yield function defines the shear failure envelope by means of the expression:

$$f^s = \sigma_1 - \sigma_3 N_\varphi + 2c\sqrt{N_\varphi}$$ **Equation A4-1**

and the tensile failure by the tension yield function:

$$f^t = \sigma_t - \sigma_3$$ **Equation A4-2**

where φ is the peak angle of shearing resistance, c is the peak cohesion, σ_t the tensile strength and

$$N_\varphi = \frac{1+\sin\varphi}{1-\sin\varphi}$$ **Equation A4-3**

Note that only the major (σ_1) and minor (σ_3) principal stresses are active in the shear yield formulation presented in Equation A4-1; the intermediate principal stress (σ_2) has no effect.

The post-failure response is modelled by using a *non-associated* flow rule which corresponds to a plastic shear potential function g^s that resembles the adopted yield function of Equation A4-1, but which involves a dilatancy angle ψ instead of an of peak angle of shear resistance φ (Itasca, 2011):

$$g^s = \sigma_1 - \sigma_3 N_\psi$$ **Equation A4-4**

where the dilation parameter N_ψ is given by

$$N_\psi = \frac{1+\sin\psi}{1-\sin\psi}$$ **Equation A4-5**

The angle ψ is the dilation angle which is related to the ratio of plastic volume change to plastic shear strain and which characterises the shear dilatancy of a material i.e. the change in volume that occurs with shear distortion. Slightly before and beyond peak strength, the dilatancy angle attains a constant value which is significantly smaller than the peak angle of shearing resistance.

The dilation angle ψ for geological materials is typically determined from triaxial tests, as specified by ISRM (1983), by making use of the slope of the volumetric strain versus axial strain that characterises the post-failure regime (Vermeer & de Borst, 1984).

A.4.1.2. The Drucker-Prager plasticity model

The Drucker-Prager model (Drucker & Prager, 1952) belongs to the family of the plastic models which potentially involve some degree of permanent, path-dependent deformation (failure): a consequence of the nonlinearity of the stress-strain relation that governs its constitutive response. The model is characterised by its yield function, hardening/softening functions and flow rule. The yield function defines the stress combination for which plastic flow takes place and is represented by a combination of limiting surfaces in a generalised stress space with points below or on the surface being characterised by an incremental elastic or plastic behaviour, respectively.

The adopted plastic flow formulation rests on basic assumptions from plasticity theory that the total strain increment may be decomposed into elastic and plastic parts, with only the elastic part contributing to the stress increment by means of an elastic law (Itasca, 2011). In addition, both plastic and elastic strain increments are taken to be coaxial with the current principal axes of the stresses. (This is only valid if elastic strains are small compared to plastic strains during plastic flow.) The flow rule specifies the direction of the plastic strain increment vector as that normal to the potential surface - it is called *associated* if the potential and yield functions coincide, and *non-associated* otherwise.

For the Drucker-Prager model a shear yield function and a *non-associated* shear flow rule are used. In addition, the failure envelope is characterised by a tensile yield function with *associated* flow rule. The relationships that express mathematically the failure characteristics of the Drucker-Prager model are included below.

In the implemented numerical analysis the out-of-plane stress is taken into consideration in the formulation that is expressed in three-dimensional terms. In the numerical implementation of the model, an elastic trial (or 'elastic guess') for the stress increment is first computed from the total strain increment using the incremental form of Hooke's law. The corresponding stresses are then evaluated. If they violate the yield criterion (i.e., the stress point representation lies above the yield function in the generalised stress space), plastic deformations take place. In this case, only the elastic part of the strain increment can contribute to the stress increment; the latter is corrected by using the plastic flow rule to ensure that the stresses lie on the composite yield function.

In the Drucker-Prager model the post-failure simulation is implemented, as shown below, by introducing the dilation q_ψ to model the shear dilatancy type of post-failure response. This property is only activated after the onset of failure, as defined by the Drucker-Prager relation shown in Equation A4-6, below.

Mathematical definition of Drucker-Prager failure criterion

The Drucker-Prager model is used for geological materials that yield when subjected to shear loading and the corresponding shear failure envelope is expressed by the following relationship:

$$f^s = \sqrt{J_2} + \frac{q_\varphi}{3} I_1 - k_\varphi$$

Equation A4-6

while the tensile failure is given by the following tension yield function:

$$f^t = \frac{I_1}{3} - \sigma_t$$

Equation A4-7

where σ_t is the tensile strength.

Examination of Equation A.4-6 indicates that that the yield stress depends on the two stress invariants:

- the first invariant (I_1) of the Cauchy stress tensor equal to:

$$I_1 = (\sigma_1 + \sigma_2 + \sigma_3)$$

Equation A4-8

- the second invariant (J_2) of the deviatoric stress tensor equal to:

$$J_2 = \frac{1}{6}\left[(\sigma_1 - \sigma_2)^2 + (\sigma_1 - \sigma_3)^2 + (\sigma_2 - \sigma_3)^2\right]$$

Equation A4-9

where: σ_1, σ_2 and σ_3 are the major, intermediate and minor principal stresses respectively and where q_φ and k_φ are constant material properties. The slope of the Drucker-Prager failure envelope corresponds to ⅓ of the parameter q_φ and the parameter k_φ is the intercept of the Drucker-Prager failure envelope with the $\sqrt{J_2}$ axis.

The post-failure response is modelled by using a *non-associated* flow rule which corresponds to a plastic shear potential function g^s that resembles the adopted yield function of Equation A4-6, but has the form:

$$g^s = \sqrt{J_2} + \frac{q_\psi}{3} I_1$$

Equation A4-10

Shear dilatancy is the change in volume that occurs with shear distortion of a material and is characterised by a dilation angle, ψ, which is related to the ratio of plastic volume change to plastic shear strain. The dilation parameter q_ψ for the Drucker-Prager model is determined by employing the following equation:

$$q_\psi = \frac{6}{\sqrt{3}(3 - \sin\psi)} \sin\psi$$

Equation A4-11

A.4.1.3. The creep models for salt

Appraisal of the safety of the long term stability of the hydrogen storage caverns requires a constitutive law that accurately models the time-dependent mechanical behaviour of salt. Salt is characterised by a distinctive creep response which is manifested by the fact that it is capable of deforming with time even if the applied stress remains constant.

Creep typically occurs in three stages: primary, or Stage I; secondary, or Stage II and tertiary, or Stage III (see Figure A4-1). At first, as the load is applied the initial elastic strain occurs (virtually instantaneously) but as time passes, under constant stress, the rate of strain reduces. Initially, the strain rate is relatively high but it slows with increasing strain and this period of decelerating strain-rate is identified as primary creep. Resistance to creep increases as the strain rate eventually reaches a minimum and nearly becomes constant when the secondary creep phase is reached. The rate of creep during the secondary creep phase becomes approximately steady and for this reason this stage is often referred to as steady state creep.

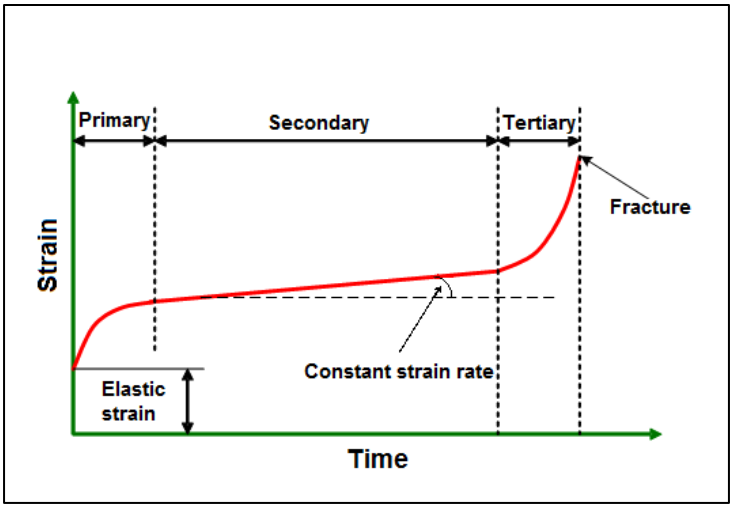

Figure A4-1: The idealised strain-time curve for a creep test

At the end of Stage II, as the strain rate exponentially increases with strain, the creep rate begins to accelerate resulting in the initiation of a creep fracture process. This final stage of accelerating deformation that leads to a rapid material failure is called Stage III, or tertiary creep.

It is interesting to note that laboratory long-term creep tests conducted during the 80's and 90's in the University of Newcastle upon Tyne using UK Triassic and Permian salt specimens, failed to identify clearly the transition from primary to secondary creep stage and a progression from the primary directly to the tertiary creep stage was observed instead. A similar conclusion, for the transition from primary to secondary creep stage, has been reached in assessing long-term in situ creep converge measurements taken in the Winsford salt mine in Cheshire (Passaris & Dunn, 2016).

Several models, which employ a variety of constitutive equations that express mathematically the time-dependent response of geological materials that creep, may be found in the literature. From the various available models, the WIPP model and the Norton Power Law model were selected to mathematically describe the creep response of the geological materials involved in the geomechanical analysis of the salt caverns.

The creep parameters for the Triassic Northwich Halite salt, which were provided by the Cheshire caverns operators, are based on the Lemaitre creep model. However, during the geomechanical modelling of the Cheshire caverns in Stage 2, the Lemaitre parameters will be converted to their equivalent WIPP parameters. Consequently the creep response of the Permian strata of ZG2 Main Salt and the Triassic Northwich Halite salt will be modelled using the WIPP law. Furthermore, the Permian strata of the Carnallitic Marl, the ZG3 Boulby Halite and the ZG2 Upper and Lower Halites will be modelled using the Norton Power Law.

The WIPP-creep visco-elastic model

The creep law that describes the behaviour of salt should be valid for wide ranges of stress states, stress magnitude and time, and also for complex stress histories and temperature histories. For this reason the time-dependent behaviour of salt in this report will been modelled in Stage 2 by combining the non-linear visco-elastic WIPP model (Herrmann et al, 1980a, 1980b) with the Drucker-Prager plasticity model. Of the available plasticity models the Drucker-Prager model is the most compatible with the WIPP-reference creep law, because both models are formulated in terms of the second invariant of the deviatoric stress tensor (J_2).

The relationships that express mathematically the creep response of salt in accordance with the WIPP model are included below.

The WIPP creep law is based in the exponential function of Arrhenius (Logan, 1982) according to the mathematical configuration described by Equations A4-12 and A4-13:

$$\varepsilon_c = A\sigma^n \exp\left(-\frac{Q}{RT}\right) t + \varepsilon_a (1 - exp[-B\dot{\varepsilon}_{ss} t]) \quad \text{for} \quad \dot{\varepsilon}_{ss} \geq \dot{\varepsilon}^*_{ss}$$ **Equation A4-12**

$$\varepsilon_c = A\sigma^n \exp\left(-\frac{Q}{RT}\right) t + \varepsilon_a \left(\dot{\varepsilon}_{ss} / \dot{\varepsilon}^*_{ss}\right)\left(1 - exp[-B\dot{\varepsilon}^*_{ss} t]\right) \quad \text{for} \quad \dot{\varepsilon}_{ss} \leq \dot{\varepsilon}^*_{ss}$$ **Equation A4-13**

where:

ε_c= creep strain expressed in [m/m],

t = time expressed in [d], and

σ = applied stress (stress difference) expressed in [MPa],

T = temperature expressed in [K],

Q = activation energy expressed in [cal/mol],

R = 1.987 cal/(mol K) the universal gas constant,

n = dimensionless stress exponent,

A = creep constant expressed in [MPa^{-n} d^{-1}],

B = dimensionless empirical material parameter relating the creep rate parameters to the steady-state creep rate,

$\dot{\varepsilon}^{*}_{ss}$= critical steady-state creep rate expressed in [(m/m) d^{-1}], and

ε_{α} = asymptotic transient strain parameter expressed in [m/m].

In Equations A4-12 and A4-13, which express mathematically the WIPP creep law, the first part i.e. the expression:

$$A\sigma^{n}\exp\left(-\frac{Q}{RT}\right)t \qquad \textbf{Equation A4-14}$$

represents the secondary creep, while the remaining terms correspond to the primary creep.

The implication of using the WIPP creep law that includes secondary creep, in modelling storage caverns developed in a salt formation that may not exhibit secondary creep, is to provide an additional factor of safety.

The Lemaitre creep model

The Lemaitre power law (Lemaitre, 1970), which expresses the behaviour of ductile metals, describes also the creep constitutive response of materials in the form of strain hardening. This model was employed by Vouille et al (1981) for the creep of salt rocks and has been used in a large number of studies concerning the geomechanical response of gas storage caverns to describe both the salt and non-salt (mudstone) interbeds viscoplastic behaviour. The relationships that express mathematically the creep response of salt in accordance with the Lemaitre model are included below. The Lemaitre law is capable of describing both the transient primary creep and the steady-state creep mechanisms. Consideration of creep induced failure, or tertiary creep, is generally not attainable by numerical codes and reflected by numerical instabilities.

For comparison purposes, the so-called Vouille's index is often used which represents the viscoplastic strain reflected by a sample subjected for one year to 10 MPa of deviatoric stress. A selection of Lemaitre creep law parameters and Vouille's index values may be found in Fine (1998). Vouille's index can be easily used to compare Lemaitre creep law with other constitutive creep expressions that may be used for the time-dependent modelling of salt.

In its general form the rheological model of Lemaitre, also referred to as Menzel-Schreiner (Menzel & Schreiner, 1977) is characterised by the following features (Hadj-Hassen et al, 2009):

- the material is isotropic and elasto-visco-plastic and undergoes irreversible deformations when it is subjected to a deviatoric stress,
- the viscoplastic deformations occur without change of volume and the rate of the non-elastic strain tensor is parallel to the deviatoric stress tensor,
- a cylindrical salt sample subjected to a constant deviatoric stress σ_{dev} (difference between the axial stress σ_{axl} and the confining lateral stress σ_{cnf}) and a constant temperature T, undergoes a relative reduction ε_{axl} of its height (axial strain) which may be expressed by the following relationship:

$$\boldsymbol{\varepsilon_{axl} = \frac{\sigma_{axl}-2\nu\sigma_{cnf}}{E} + \varepsilon_{vp}\,\xi(T)\mathrm{t}^{\alpha} + \alpha_{l}(T-T_{o})} \qquad \textbf{Equation A4-15}$$

The elastic part of the strain is related to the variation of the stress by the standard linear elastic law defined by the Young's modulus E and the Poisson's ratio ν. The thermal part is a linear function of the temperature characterised by the thermal dilation coefficient α_l. The creep part is due to the viscosity of the salt and obeys a power law with time (power α).

Where:

- $\xi(T)$ is an increasing temperature function that quantifies the effect of temperature on creep. The $\xi(T)$ function indicates that higher is the temperature of the test, the more the material is creeping and it takes in general the following form:

$$\xi(T) = \exp\left[-\frac{Q}{R}\left(\frac{1}{T}-\frac{1}{T_r}\right)\right] \qquad \text{Equation A4-16}$$

with T_r being a reference temperature, typically taken as 300 K.

- ε_{vp} is the viscoplastic strain which is expressed, in its classical uniaxial form, as follows:

$$\varepsilon_{vp} = \left(\frac{\sigma_{dev}}{K}\right)^{\beta} t^{\alpha} \qquad \text{Equation A4-17}$$

Where:

σ_{dev} = deviatoric stress expressed in [MPa]

t = time expressed in [d]

α = time exponent, dimensionless Lemaitre parameter

β = stress ratio exponent, dimensionless Lemaitre parameter

K = stress Lemaitre parameter expressed in [MPa].

The Norton power law

The Norton power law (Norton, 1929) is a classic creep law used to describe the time-dependent deformation of geological materials. This is often expressed in rate form as:

$$\dot{\varepsilon_c} = C\sigma^n \qquad \text{Equation A4-17}$$

where $\dot{\varepsilon_c}$ is the steady-state creep rate expressed in [(m/m) d^{-1}], σ is the applied stress (stress difference) expressed in [MPa], while C and n are material parameters.

It is important to mention that the Norton creep law is only an approximation of the actual creep behaviour of the modelled geological materials. It neglects the straining occurring in the transient phase and it idealises the stress-strain rate relationship. Nevertheless, this model is commonly used because of its simplicity of application.

A.4.2. Geological material parameters

A.4.2.1. East Yorkshire Salt Field

Table A4-1 Density, deformability and tensile strength

Material	Density [Mg/m3]	Bulk modulus [MPa]	Shear modulus [MPa]	Tensile strength [MPa]
Carnallitic Marl:	2.30	3,894	2,921	1.89
Zechstein III Boulby Halite:	2.15	10,283	8,701	1.43
Zechstein III Billingham Anhydrite:	2.93	51,321	32,282	5.88
Zechstein III Brotherton Formation:	2.42	16,571	15,130	5.28
Grauer Salzton:	2.29	18,519	12,195	1.30
Zechstein II Fordon Evaporites – Upper Halite:	2.15	16,667	10,000	1.60
Zechstein II Fordon Evaporites – Anhydrite:	2.90	33,333	15,385	8.56
Zechstein II Fordon Evaporites – Lower Halite:	2.15	16,667	10 000	1.60
Zechstein II Fordon Evaporites – Main salt:	2.56	19,279	12,127	1.60
Zechstein II Polyhalite:	2.85	27,785	14,777	4.73
Hayton Anhydrite:	2.94	50,000	23,077	8.44
Cadeby Formation:	2.62	26,149	18,802	11.0

Table A4-2 Mohr-Coulomb parameters

Material	Angle of shearing resistance [°]	Cohesion [MPa]	Dilation angle [°]
Zechstein III Billingham Anhydrite	48.18	15.6	11.08
Zechstein III Brotherton Formation	44.05	13.8	9.65
Grauer Salzton	49.0	0.41	11.39
Zechstein II Fordon Evaporites - Anhydrite	45.0	5.0	9.96
Zechstein II Polyhalite	44.13	10.73	9.68
Hayton – Anhydrite	41.6	23.96	8.89
Cadeby Formation	40.0	42.0	8.41

Table A4-3 Norton Power Law parameters

Material	Constant C	Stress exponent n
Carnallitic Marl	1.20×10^{-10}	4.0
Zechstein III Boulby Halite	1.73×10^{-11}	4.8
Zechstein II Fordon Evaporites – Upper Halite	1.73×10^{-11}	4.8
Zechstein II Fordon Evaporites – Lower Halite	1.73×10^{-11}	4.8

Table A4-4 Main Salt parameters for the PWIPP model

q_φ	0.2016,
k_φ	24.176 MPa
q_ψ	0.001
Q	14,030 cal/mol,
R	1.987 cal/(mol K),
n	2.10,
A	45 MPa-n d-1,
B	700,
$\dot{\varepsilon}^*_{ss}$	9.5 × 10-6 (m/m) d-1, and
ε_α	0.02 m/m.

A.4.2.2. Teesside Salt Field

Table A4-5 Density, deformability and tensile strength

Material	Density [Mg/m3]	Young's modulus [GPa]	Poisson's ratio	Tensile strength [MPa]
Boulder Clay (assumed)	1.95	0.037	0.31	0.006
Lower Liassic Shales	2.40	16.830	0.20	3.88
Penarth Shales	2.58	12.970	0.29	4.25
Mercia Mudstone	2.48	34.070	0.10	2.78
Sherwood Sandstone	2.45	14.574	0.08	2.60
Roxby Formation	2.55	14.191	0.09	2.75
Sherburn Anhydrite	2.76	33.045	0.23	3.04
Carnallitic Marl	2.30	7.100	0.20	1.89
Upper Main Salt	2.15	20.360	0.17	1.43
Honeycomb Anhydrite	2.85	56.550	0.24	4.46
Lower Main Salt	2.15	20.360	0.17	1.43
Billingham Anhydrite	2.93	80.060	0.24	5.88
Brotherton Formation	2.42	34.800	0.15	5.28

Table A4-6 Mohr-Coulomb parameters

Material	Angle of shearing resistance [°]	Cohesion [MPa]	Dilation angle [°]
Boulder Clay (assumed)	28.08	0.01	7.50
Lower Liassic Shales	33.92	15.22	6.81
Penarth Shales	33.87	14.10	6.80
Mercia Mudstone	47.77	21.83	10.93
Sherwood Sandstone	31.58	16.82	14.00
Roxby Formation	36.07	16.00	16.00
Sherburn Anhydrite	21.38	22.88	10.00
Carnallitic Marl	6.93	5.74	4.00
Upper Main Salt	38.64	8.74	6.00
Honeycomb Anhydrite	25.69	27.44	10.00
Lower Main Salt	6.93	5.74	4.00
Billingham Anhydrite	30.00	32.00	10.00
Brotherton Formation	40.00	42.00	20.00

A.4.2.3. Cheshire basin

Table A4-7: Marl and Salt Material Properties

Material property	Marl	Salt
Density[Mg/m3]	2.498	2.174
Young's modulus [GPa]	9.287	27.048
Poisson's ratio	0.17	0.30
Tensile strength [MPa]	1.76	1.75
Cohesion [MPa]	10.0	-
Angle of shearing resistance [°]	35	-

The mean deviatoric stress associated with the beginning of dilation of the salt is about 28.7 MPa. For salt, the dilation strength should be understood as a maximum allowable stress magnitude, but cannot be interpreted as a shear failure criterion. As the confining pressure is increased, the dilating phase is less pronounced and in fact the deviatoric stress ($\sigma_1 - \sigma_3$) depends on the applied pressure (σ_3). The linear fitting of this trend leads to the following relationship:

$$(\sigma_1 - \sigma_3) = 2.4 \times \sigma_3 + 15.9 \text{ [MPa]} \qquad \text{Equation A4-18}$$

The creep tests led to very similar results (the Vouille creep index varying between 0.42% and 0.52%). These indexes show that Cheshire salt may be classified as a relatively low creeping rock.

The following parameters describe the creep behaviour of Stublach salt according to Lemaitre's model:

α= 0.1, β= 2.208, K = 0.349 MPa (at T=300 K) and B = Q/R =1,581 K.

These values lead to a Vouille creep index of 0.47 %.

ATKINS

Appendix B: Power generation

B.1. GT PRO

Selected GTs were simulated in the industry recognised GT PRO software package to model both the open cycle GT and the overall CCGT plant performance predicting the following parameters, including:

- GT gross power output and efficiency at various GT loads;
- CCGT plant net power output and efficiency;
- Turbine Inlet and Exhaust Temperature;
- Compressor air bleed flow (if applicable).

The power output and efficiency values were then used to estimate the overall fuel/diluent gas flow demand for the Power Plant and consequently evaluate the salt cavern suitability for H_2 fuel storage at each site. Figure B1-1 presents a summary of the evaluation process.

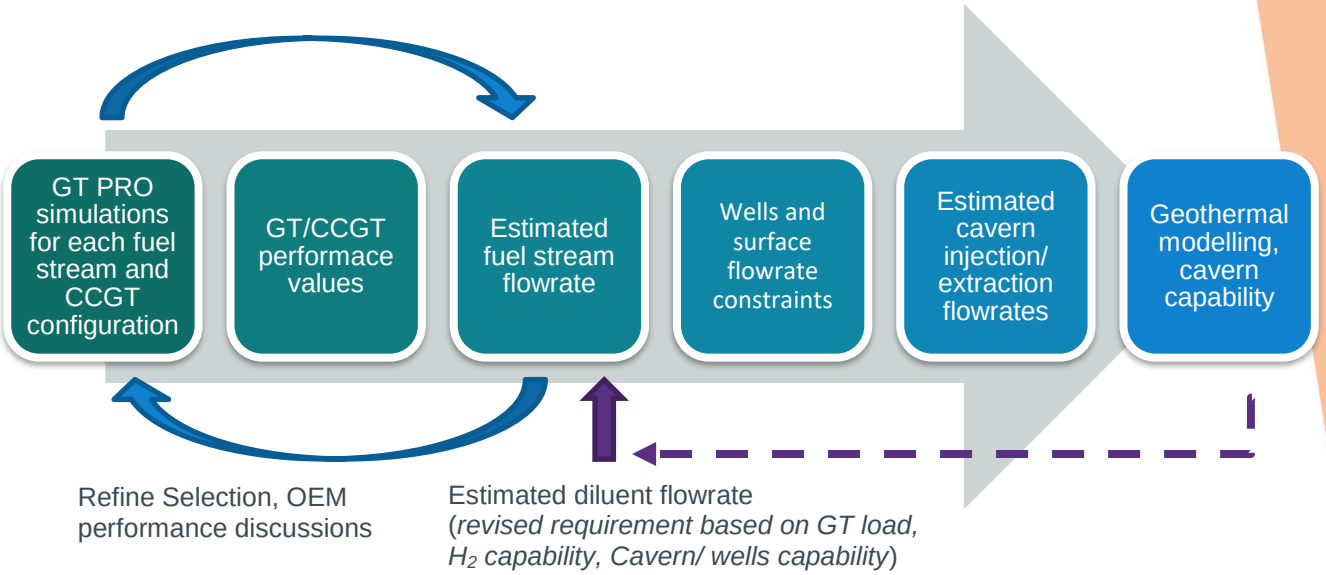

Figure B1-1: Evaluation process flow diagram

B.1.1. GT PRO Assumptions

The following assumptions have been made within the GT PRO simulations:

- GT PRO assumed dry air cooled condenser at ISO conditions across all cases. Except for the case with SGT-800, where the calculations were based purely on data received from the manufacturer.
- GT PRO assumed that N_2 for dilution was supplied externally from outside of the Power Plant. For example, in case of biomass gasification, H_2 Production Plant ASU is estimated to produce circa 75kg/s pure N_2 (based on AmecFW report).
- When required, compressor air bleed flowrate was assumed to be the same as N_2 injection flowrate.
- GT PRO assumed that steam for dilution was supplied from the main CCGT HP steam thus reducing the overall plant net power output and efficiency.
- The “H” class SGT5-8000H GT has been considered, however the GT PRO modelling capability of this GT is limited to natural gas and distillate oil, and the modelling of increased H_2 fractions is still ongoing R&D. As such, initial modelling results have been interpreted from GTs firing natural gas and refined through discussions with OEMs.

B.1.2. GT PRO limitations

GT PRO is configured to maintain the TIT (TIT) constant and therefore, resulting in the near constant GT power output by varying the amount of fuel required. Whereas based on the OEM feedback for DLE burners, it became clear that beyond a certain fraction of H_2 in the fuel of about 10-15 vol%, the TIT would likely reduce to avoid flame instabilities in the combustor. By modelling through GT-PRO on this basis, It was found that TITs below approx. 1,150°C should not pose a flame instability issue. In GT PRO, the SGT5-2000E model is configured to 1,149 °C TIT. Therefore, when modelling the "E" class GT, it was assumed that the TIT would not have to be reduced further.

B.2. GT down selection

Table B2-1 below presents the list of GTs reviewed as part of this study against the performance metrics listed in Table B2-2. The GTs considered have also been plotted against technical risk to combust H_2 and GT size in Figure B2-1.

Table B2-1: GTs modelled for perfomance characteristics on high hydrogen fuel

GT type	Type	Net output (MW) OCGT	Net output (MW) CCGT 1+1	Plant efficiency (%) LHV for OCGT 1+1	Plant efficiency (%) LHV for CCGT 1+1
GE GT-9E.04	Frame	153	223	38	56
GE GT-9F.05	Frame	324	481	40	60
GE GT-9HA.02	Frame	521	757	42	61
GE GT-6B.03	Frame	46	70	34	52
Ansaldo 13E2	Frame	200	284	39	56
Siemens SGT5-2000E	Frame	171	260	35	54
Siemens SGT5-4000F	Frame	301	435	41	59
*Siemens SGT5-8000H	Frame	425	630	40	61
Siemens SGT-800	Frame	53	74	40	55
Siemens SGT-700	Frame	33	47	37	53
Siemens SGT-600	Frame	26	37	35	50
MHPS 701F4	Frame	345	492	41	59
MHPS 701F5	Frame	400	566	43	61
Siemens RR Trent 60 DLE	Aero	55	72	43	56

* GT PRO has no capability to model Siemens SGT5-8000H with other fuel than pure methane and distillate oil, so the performance values for this GT model were taken from Siemens catalogue (Siemens, 2017).

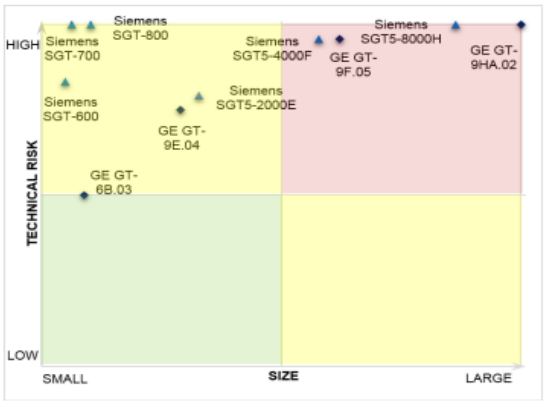

Figure B2-1: GT selection, technical risk vs size (relative comparison only)

Table B2-1: GT selection matrix

	Max H_2 (vol%)	Past experience	Emissions (NO_x)	Hot start-up times (OCGT)	Hot start-up times (CCGT)	Cold start-up times (CCGT)	Turn down - Minimum load (CCGT)	No of units for capacity (CCGT)	Turn down - Minimum load (OCGT)	No of units for 1GWe capacity (OCGT)
GE GT-9HA.02 (DLE)										
Siemens SGT5-8000H (DLE)										
Siemens SGT5-8000H* (Diffusion)										
GE GT-9F.05 (DLE)										
Siemens SGT5-4000F* (DLE)										
*MHPS 701F4										
*MHPS 701F5										
GE GT-9E.04 (DLE)										
Siemens SGT5-2000E* (DLE)										
Siemens SGT5-2000E* (Diffusion)										
*Ansaldo 13E2										
GE GT-6B.03 (DLE)										
Siemens SGT-800 (DLE)*										
Siemens SGT-700 (DLE)										
Siemens SGT-600 (DLE)										
Siemens SGT-600 (Diffusion)										
Siemens RR Trent 60										

***GTs highlighted in bold are the GTs down selected as part of this study.**

Other GT choices reviewed:

- "F" class GTs are well established and would provide more flexibility as a plant configuration to meet the 1 GWe demand. However, Siemens and GE, have indicated that the "F" class GTs would, at present, be unsuitable to fire more than 5-10 vol%H_2 in DLE combustors. The H_2 fraction is low relative to the "E" class models of similar power range and so "F" class GTs are a less preferred option for this study.
- It should be noted that Aero-derivative GTs were not reviewed in detail as initial research revealed they are unsuited for high H_2 combustion due to risk of flashback and auto-ignition. Although the aero-derivative GTs appear to be technically capable to combust proportions of hydrogen, it is likely that they would not be suitable to fire such low calorific value fuel as methane ATR fuel, as considered in the study. Additionally, due to their small size it was considered impracticable to scale to 1GW generation.

References of firing syngas or hydrogen (vol%H_2)

- Red - <10 vol%
- Yellow - 10-50 vol%
- Green - ≥50 vol%

References for previous experience with H_2

- Green - Proven references on gas AND hydrogen (e.g. E Class)
- Yellow - Proven references on gas OR hydrogen (e.g. F Class)
- Red - References and experience largely only on gas (e.g. H Class, aero)

Emissions (NO_x)

- Green - < 50 mg/Nm3
- Yellow - 50-120 mg/Nm3
- Red - > 120 mg/Nm3

Hot start-up times (OCGT)

- Green - < 15 mins
- Yellow - 15 – 60 mins
- Red - > 60 mins

Hot start-up times (CCGT)

- Green - < 30 mins
- Yellow - 30 – 60 mins
- Red - > 60 mins

Cold start-up times (CCGT)

- Green - < 120 mins
- Yellow - 120 – 240 mins
- Red - > 240 mins

Turn down - Minimum load (per unit) - Measure of flexibility of plant

- Green - 25 - 35%
- Yellow - 35 – 40%
- Red - >40%

No of blocks/units for 1GWe capacity

- Green - 2 - 5
- Yellow - 5 - 15
- Red - 15+

Notes: Most GTs will stay within the NO_x limit unless fired with fuel, which exceeds their maximum H_2 fraction specified by the OEMs.

B.3. GT Case Studies

Many of the projects listed below involve government funding support and are unlikely to meet the hurdles, at this time, for project finance in the UK. This is not just a technical issue but one of identifying risk and restructuring of the current UK electricity supply market to cater for the new entrants which are able to deliver firm capacity. It is noted that a significant benefit of the "F" & "H" class GTs relates to the economies of scale of the larger GTs driving down the installed CAPEX and installed generation specific costs.

Table B3-1: GT Case Studies

Project	GT	Power output (MW)	H_2/ N_2 (vol%)	LHV	GT operation start date	Source fuel
La Coruna, Spain	6B	~40	up to 52	25.00 MJ/m^3	1991	Refinery gas
Rotterdam, Holland	6B	~40	59	28.00 MJ/m^3	1900	Refinery gas
Cartagena, Spain	6B	~40	66	25.10 MJ/m^3	1993	Refinery gas
San Roque, Spain	2x6B	2x~40 MW	70	24.00 MJ/m^3	1993	Refinery gas
Antwerp, Belgium	6B	~40MW	78	20.70 MJ/m^3	1993	Refinery gas
Tenerife, Spain	6B	~40	70	29.00 MJ/m^3	1994	Refinery gas
Puertollano, Spain (currently operational)	2x6B	2x~40 MW	60	16.70 MJ/m^3	1992/94	Refinery gas
Texaco El Dorado, Kansas	6B	40	35.4 / 2.1	9.54 MJ/m^3	1996	Syngas from pet coke
SVZ Schwarze Pumpe, Germany	6B	40	61.9 / 1.8	12.52 MJ/m^3	1996	Syngas from coal/ waste gasification
Shell Pernis, Netherlands	206B	120	34.4 / 0.2	8.24 MJ/m^3	1997	Syngas from oil gasification
Daesan 2, Korea	6B	~40	up to 95%H_2	16.50 MJ/m^3	1995	Process gas
IBIL Sanghi, Gujarat, India	106B	53	12.7 / 46.0	4.53 MJ/m^3	2001	Syngas from coal gasification
ILVA ISE, Taranto, Italy	3x109E	520	8.6 / 42.5	7.60 MJ/m^3	1996	Coke Oven Gas (COG)
SUV Vresova, Czech Rep.	209E	350	47	11.80 MJ/Nm^3	1995	Syngas from coal gasification
Sarlux, Sarroch, Italy (currently operational)	3x109E	550	22.7 / 1.1	6.42 MJ/m^3	2000	Syngas from oil gasification
EDF-Total, Gardanne France	2x9E	400	Oil Cogen/H_2 Syngas		2003	Syngas from oil gasification
Fawley Esso Plant, UK	9E	120	up to 55vol%H_2	27.30 MJ/m^3	1998	Refinery gas
Fife Electric, Scotland	109FA	350	34.3 / 3.1	12.69 MJ/m^3	2000	Syngas from coal/ waste gasification

Nuon Power Buggenum, Netherlands (currently operational)	V94.2 (old naming for SGT5-2000E)	253	12.3 / 42.0	4.3 MJ/kg	1994/95	Syngas from coal/ biomass gasification
ELCOGAS, Puertollano, Spain	V94.3 (old naming for SGT5-4000F)	300	10.7 / 53.1	4.3 MJ/kg	1997/98	Syngas from coal/ petroleum coke gasification
ISAB Energy Priolo Gargallo, Italy (currently operational)	2xV94.2K (old naming for SGT5-2000E)	521	31.1	9.1 MJ/kg	1999	Syngas from oil gasification
ELETTRA GLT Servola, Italy	V94.2K	180			2000	Steel making recovery gas
Eni Power Sannazzaro, Italy	V94.2K (old naming for SGT5-2000E)	250			2006	Syngas from heavy-oil gasification
Huaneng Tianjin IGCC Green Coal Power, China	SGT5-2000E	250			2011	Syngas from coal gasification
BP Castellon Refinery, Spain	SGT-600	26	<55%		2007	Refinery gas
Petrochemical Corporation of Singapore	SGT-600	25	10-25%		1994	Refinery gas
Hellenic Refinery, Aspropyrgos, Greece	2xSGT-600	about 50MW	20-90		1988	Refinery gas
Stora Enso, Maxau, Germany	SGT-600	about 25MW	10-75%		1991	Refinery gas
Cool Water Barstow, California	107E	120			1984	Syngas from coal gasification
PSI/ Terre Haute Indiana	7FA	262	24.8/2.3	8.35 MJ/m^3	1996	Syngas from coal gasification
Tampa Electric, Polk, Florida	107FA	250	27/6.8	7.96MJ/m^3	1996	Syngas from coal gasification
Tampa Electric Sparks Nevada	106FA	100	27/6.8	7.96MJ/m^3	1996	Syngas from coal gasification
Motiva, Delaware	2-6FA	180			1999	Syngas from petroleum coke gasification
Fife Electric, Scotland	106FA	109	34.3 / 3.1		1999	Syngas from coal/ waste gasification
Api Energie Falconara, Italy (currently operating)	GT-1, GT13E2, ST-1	280			2001	Syngas from oil gasification
Nakoso, Fukishima, Japan (currently operating)	ST-7, ST-8, ST-9, ST-10	250	Approx. 10%		2011	Syngas from coal gasification

The case studies are taken from:

- GE Power Systems, 2000. “GE IGCC Technology and Experience with Advanced GTs”. Prepared by Brdar, D.R. & Jones, R.M. on behalf of General Electric Power Systems.
- GE Energy, 2004. “H_2-fuelled GTs: experience and prospects”. Prepared by Moliere, M. & Hugonnet, N.
- Siemens, 2009. “IGCC experience and further developments to meet CCS market needs.” Prepared by Juergen Karg on behalf of Siemen.
- The Global Energy Conservatory: http://globalenergyobservatory.org

B.4. GT PRO fuel flowrates outputs

Figure B4-1: GT Pro fuel outputs

GT model		SGT5-2000E	SGT5-2000E	SGT5-2000E	SGT5-2000E	SGT5-2000E	SGT5-2000E	SGT5-2000E	SGT-800
Combustion Type		Diffusion	Diffusion	Diffusion	Diffusion	Diffusion	DLE	DLE	DLE
Fuel Mix		**Mix 1**	**Mix 1 (no NG)**	**Mix 1a**	**Mix2**	**Mix 2 (no NG)**	**Mix 3**	**Mix 4**	***Mix5 (Siemens data)***
Fuel Stream and description		Stream 1 blended with NG, diluted with N_2	Stream 1 diluted with N_2, no NG	Stream 1 blended with NG, diluted with Steam	Stream 2 blended with NG.	Stream 2 further diluted with NG, no NG	Stream 1 blended with NG in DLE combustor	Stream 2 blended with NG in DLE combustor	Stream 1 blended with NG in DLE combustor
Number of GTs		4	4	4	4	4	4	4	15
Stream ID		Stream 1	Stream 1	Stream 1	Stream 2	Stream 2	Stream 1	Stream 2	Stream 1
Plant Net Output at 100% GT load	kW	1,009,792	791,918	1,002,592	986,642	787,830	972,915	977,194	*912,825*
Total GT Gross Power Output at 100% load	kW	670,472	625,754	665,888	672,460	631,524	659,564	663,340	*608,550*
GT Gross Power at 90% load	kW	603,476	563,218	599,076	608,704	568,416	593,664	597,060	*547,695*
GT Gross Power at 70% load	kW	469,376	438,062	465,508	473,440	442,108	461,740	464,384	*425,985*
GT Gross Power at 40% load	kW	268,240	250,306	265,644	270,560	252,624	263,880	265,388	*243,420*
Plant Net Electrical Efficiency at 100%load	%	52.5	50.7	52.2	51.3	50.3	51.0	51.1	-
GT Gross LHV Efficiency at 100%load	%	34.9	40.1	34.7	34.9	40.3	34.6	34.7	*36.9*
GT Gross LHV Efficiency at 90%load	%	34.2	39.1	34.0	34.3	39.3	33.9	34.0	*35.9*
GT Gross LHV Efficiency at 70%load	%	32.0	36.3	31.8	32.1	36.6	31.7	31.8	*32.9*
GT Gross LHV Efficiency at 40%load	%	26.4	28.8	26.2	26.5	29.1	26.1	26.2	*25.9*
At 100% GT Load									
Compressor inlet mass flow; per GT	kg/s	520		520	518	520	520	520	-
Compressor air bleed flow as percent of airflow; per GT	%	1	0	0	0	0	0	0	-
Turbine inlet temperature	degC	1149		1149	1148	845	1149	1149	-
Turbine exhaust temperature	degC	544		544	542	345	544	544	-
GT Gross Power	kW	670,472	625,754	665,888	672,460	631,524	659,564	663,340	608,550
GT Gross LHV Efficiency	%	34.9	40.1	34.7	34.9	40.3	34.6	34.7	36.9
LHV	kJ/kg	30350	2841	45480	30520	2905	46019	40312	43725
GT inlet fuel mass flowrate	kg/s	63	550	42	63	540	41	47	38
Fuel mix density at 0degC, 1atm	kg/Nm3	0.7294	0.9694	0.6311	0.7247	0.9638	0.7343	0.7675	0.4264
GT inlet fuel volumetric flowrate	Nm3/s	87	567	67	87	560	56	62	88.41
Stream 1 or 2 fraction (vol)	-	0.28	0.28	0.30	0.47	0.47	0.11	0.19	0.67
Stream 1 or 2 GT inlet volumetric flowrate	Nm3/s	24	159	20	41	266	6	12	59
Stream 1 or 2 density at 0degC, 1atm	kg/Nm3	0.2474	0.2474	0.2474	0.6462	0.6462	0.2474	0.6462	0.2474
Stream 1 or 2 GT inlet mass flowrate	kg/s	6	39	5	27	172	2	8	15
Stream 1 or 2 GT inlet mass flowrate + 10% Margin	**kg/s**	**7**	**43**	**5**	**29**	**189**	**2**	**8**	**16**

A1Nitrogen fraction (vol)	-	0.19	0.72	0.00	0.00	0.53	0.00	0.00	0.00
Nitrogen GT inlet volumetric flowrate	Nm3/s	17	408	-	-	294	-	-	-
Nitrogen density at 0degC, 1atm	kg/Nm3	1.251	1.251	1.251	1.251	1.251	1.251	1.251	1.251
Nitrogen GT inlet mass flowrate	kg/s	21	511	-	-	368	-	-	-
Nitrogen GT inlet mass flowrate + 10% Margin	**kg/s**	**23**	**562**	**-**	**-**	**405**	**-**	**-**	**-**
Natural Gas fraction (vol)	-	0.53	0.00	0.70	0.53	0.00	0.89	0.81	0.33
Natural Gas GT inlet volumetric flowrate	Nm3/s	46	-	47	46	-	50	50	29
Natural Gas density at 0degC, 1atm	kg/Nm3	0.7962	0.7962	0.7962	0.7962	0.7962	0.7962	0.7962	0.7962
Natural Gas GT inlet mass flowrate	kg/s	36	-	37	36	-	40	40	23
Natural Gas GT inlet mass flowrate + 10% Design Margin	**kg/s**	**40**	**-**	**41**	**40**	**-**	**44**	**44**	**25**
External GT Steam Injection flowrate	kg/s	-	-	4	-	-	-	-	-
Steam GT inlet mass flowrate + 10% Margin	**kg/s**	**-**	**-**	**4**	**-**	**-**	**-**	**-**	**-**
At 90% Load									
Compressor inlet mass flow; per GT	kg/s	484		483	483	489	483	483	-
Compressor air bleed flow as percent of airflow; per GT	%	1	0	0	0	0	0	0	-
Turbine inlet temperature	degC	1130		1130	1130	829	1130	1130	-
Turbine exhaust temperature	degC	544		544	542	345	544	544	-
GT Gross Power at 90% load	kW	603,476	563,218	599,076	608,704	568,416	593,664	597,060	547,695
GT Gross LHV Efficiency at 90%load	%	34.2	40.1	34.0	34.3	40.3	33.9	34.0	35.9
LHV	kJ/kg	30350	2841	45480	30520	2905	46019	40312	43725
GT inlet fuel mass flowrate	kg/s	58	495	39	58	486	38	44	35
Fuel mix density at 0degC, 1atm	kg/Nm3	0.7294	0.9694	0.6311	0.7247	0.9638	0.7343	0.7675	0.4264
GT inlet fuel volumetric flowrate	Nm3/s	80	511	61	80	504	52	57	82
Stream 1 or 2 fraction	-	0.28	0.28	0.30	0.47	0.47	0.11	0.19	0.67
Stream 1 or 2 GT inlet volumetric flowrate	Nm3/s	22	143	18	38	239	6	11	55
Stream 1 or 2 density at 0degC, 1atm	kg/Nm3	0.2474	0.2474	0.2474	0.6462	0.6462	0.2474	0.6462	0.2474
Stream 1 or 2 GT inlet mass flowrate	kg/s	6	35	5	25	155	1	7	14
Stream 1 or 2 GT inlet mass flowrate + 10% Margin	**kg/s**	**6**	**39**	**5**	**27**	**170**	**2**	**8**	**15**
Nitrogen fraction (vol)	-	0.19	0.72	0.00	0.00	0.53	0.00	0.00	0.00
Nitrogen GT inlet volumetric flowrate	Nm3/s	15	368	-	-	265	-	-	-
Nitrogen density at 0degC, 1atm	kg/Nm3	1.251	1.251	1.251	1.251	0.9694	1.251	1.251	1.251
Nitrogen GT inlet mass flowrate	kg/s	19	460	-	-	257	-	-	-
Nitrogen GT inlet mass flowrate + 10% Margin	**kg/s**	**21**	**506**	**-**	**-**	**282**	**-**	**-**	**-**
Natural Gas fraction (vol)	-	0.53	0.00	0.70	0.53	0.00	0.89	0.81	0.33
Natural Gas GT inlet volumetric flowrate	Nm3/s	42	-	43	42	-	46	46	27
Natural Gas density at 0degC, 1atm	kg/Nm3	0.7962	0.7962	0.7962	0.7962	0.7962	0.7962	0.7962	0.7962
Natural Gas GT inlet mass flowrate	kg/s	34	-	34	34	-	37	37	21
Natural Gas GT inlet mass flowrate + 10% Margin	**kg/s**	**37**	**-**	**38**	**37**	**-**	**40**	**40**	**23**
External GT Steam Injection flowrate	kg/s	-	-	4	-	-	-	-	-
Steam GT inlet mass flowrate + 10% Margin	**kg/s**	**-**	**-**	**4**	**-**	**-**	**-**	**-**	-
At 70% Load									
Compressor inlet mass flow; per GT	kg/s	416		415	415	434	416	416	-

Compressor air bleed flow as percent of airflow; per GT	%	1	0	0	0	0	0	0	-
Turbine inlet temperature	degC	1084		1083	1084	791	1083	1084	-
Turbine exhaust temperature	degC	544		544	542	345	544	544	-
GT Gross Power at 70% load	kW	469,376	438,062	465,508	473,440	442,108	461,740	464,384	425,985
GT Gross LHV Efficiency at 70%load	%	31.97	36.31	31.78	32.11	36.56	31.69	31.79	32.92
LHV	kJ/kg	30350	2841	45480	30520	2905	46019	40312	43725
GT inlet fuel mass flowrate	kg/s	48	425	32	48	416	32	36	30
Fuel mix density at 0degC, 1atm	kg/Nm3	0.7294	0.9694	0.6311	0.7247	0.9638	0.7343	0.7675	0.4264
GT inlet fuel volumetric flowrate	Nm3/s	66	438	51	67	432	43	47	69
Stream 1 or 2 fraction	-	0.28	0.28	0.30	0.47	0.47	0.11	0.19	0.67
Stream 1 or 2 GT inlet volumetric flowrate	Nm3/s	19	123	15	32	205	5	9	47
Stream 1 or 2 density at 0degC, 1atm	kg/Nm3	0.2474	0.2474	0.2474	0.6462	0.6462	0.2474	0.6462	0.2474
Stream 1 or 2 GT inlet mass flowrate	kg/s	5	30	4	20	132	1	6	12
Stream 1 or 2 GT inlet mass flowrate + 10% Margin	**kg/s**	**5**	**33**	**4**	**22**	**146**	**1**	**6**	**13**
Nitrogen fraction (vol)	-	0.19	0.72	0.00	0.00	0.53	0.00	0.00	0.00
Nitrogen GT inlet volumetric flowrate	Nm3/s	13	315	-	-	227	-	-	-
Nitrogen density at 0degC, 1atm	kg/Nm3	1.251	1.251	1.251	1.251	1.251	1.251	1.251	1.251
Nitrogen GT inlet mass flowrate	kg/s	16	394	-	-	284	-	-	-
Nitrogen GT inlet mass flowrate + 10% Margin	**kg/s**	**18**	**434**	**-**	**-**	**312**	**-**	**-**	**-**
Natural Gas fraction (vol)	-	0.53	0.00	0.70	0.53	0.00	0.89	0.81	0.33
Natural Gas GT inlet volumetric flowrate	Nm3/s	35	-	36	35	-	38	38	23
Natural Gas density at 0degC, 1atm	kg/Nm3	0.7962	0.7962	0.7962	0.7962	0.7962	0.7962	0.7962	0.7962
Natural Gas GT inlet mass flowrate	kg/s	28	-	28	28	-	30	30	18
Natural Gas GT inlet mass flowrate + 10% Margin	**kg/s**	**31**	**-**	**31**	**31**	**-**	**34**	**34**	**20**
External GT Steam Injection flowrate	kg/s	-	-	3	-	-	-	-	-
Steam GT inlet mass flowrate + 10% Margin	**kg/s**	**-**	**-**	**3**	**-**	**-**	**-**	**-**	**-**
At 40% Load									
Compressor inlet mass flow; per GT	kg/s	356		356	356	358	356	356	-
Compressor air bleed flow as percent of airflow; per GT	%	1	0	0	0	0	0	0	-
Turbine inlet temperature	degC	920		917	917	714	918	918	-
Turbine exhaust temperature	degC	487		486	484	345	486	486	-
GT Gross Power at 40% load	kW	268,240	250,306	265,644	270,560	252,624	263,880	265,388	243,420
GT Gross LHV Efficiency at 40%load	%	26.4	28.8	26.2	26.5	29.1	26.1	26.2	25.9
LHV	kJ/kg	30350	2841	45480	30520	2905	46019	40312	43725
GT inlet fuel mass flowrate	kg/s	34	306	22	33	299	22	25	21
Fuel mix density at 0degC, 1atm	kg/Nm3	0.7294	0.9694	0.6311	0.7247	0.9638	0.7343	0.7675	0.4264
GT inlet fuel volumetric flowrate	Nm3/s	46	315	35	46	310	30	33	50
Stream 1 or 2 fraction	-	0.28	0.28	0.30	0.47	0.47	0.11	0.19	0.67
Stream 1 or 2 GT inlet volumetric flowrate	Nm3/s	13	88	11	22	147	3	6	34
Stream 1 or 2 density at 0degC, 1atm	kg/Nm3	0.2474	0.2474	0.2474	0.6462	0.6462	0.2474	0.6462	0.2474
Stream 1 or 2 GT inlet mass flowrate	kg/s	3	22	3	14	95	1	4	8
Stream 1 or 2 GT inlet mass flowrate + 10% Margin	**kg/s**	**4**	**24**	**3**	**16**	**105**	**1**	**4**	**9**

Nitrogen fraction (vol)	-	0.19	0.72	0.00	0.00	0.53	0.00	0.00	0.00
Nitrogen GT inlet volumetric flowrate	Nm3/s	9	227	-	-	163	-	-	-
Nitrogen density at 0degC, 1atm	kg/Nm3	1.251	1.251	1.251	1.251	1.251	1.251	1.251	1.251
Nitrogen GT inlet mass flowrate	kg/s	11	284	-	-	204	-	-	-
Nitrogen GT inlet mass flowrate + 10% Margin	**kg/s**	**12**	**312**	**-**	**-**	**224**	**-**	**-**	**-**
Natural Gas fraction (vol)	-	0.53	0.00	0.70	0.53	0.00	0.89	0.81	0.33
Natural Gas GT inlet volumetric flowrate	Nm3/s	24	-	25	24	-	27	27	16
Natural Gas density at 0degC, 1atm	kg/Nm3	0.7962	0.7962	0.7962	0.7962	0.7962	0.7962	0.7962	0.7962
Natural Gas GT inlet mass flowrate	kg/s	19	-	20	19	-	21	21	13
Natural Gas GT inlet mass flowrate + 10% Margin	**kg/s**	**21**	**-**	**22**	**21**	**-**	**23**	**23**	**14**
External GT Steam Injection flowrate	kg/s	-	-	2	-	-	-	-	-
Steam GT inlet mass flowrate + 10% Margin	**kg/s**	**-**	**-**	**2**	**-**	**-**	**-**	**-**	-

ATKINS

Appendix C:

Surface Plant Process Design

C.1. Surface plant design considerations

C.1.1. Surface plant flow diagram

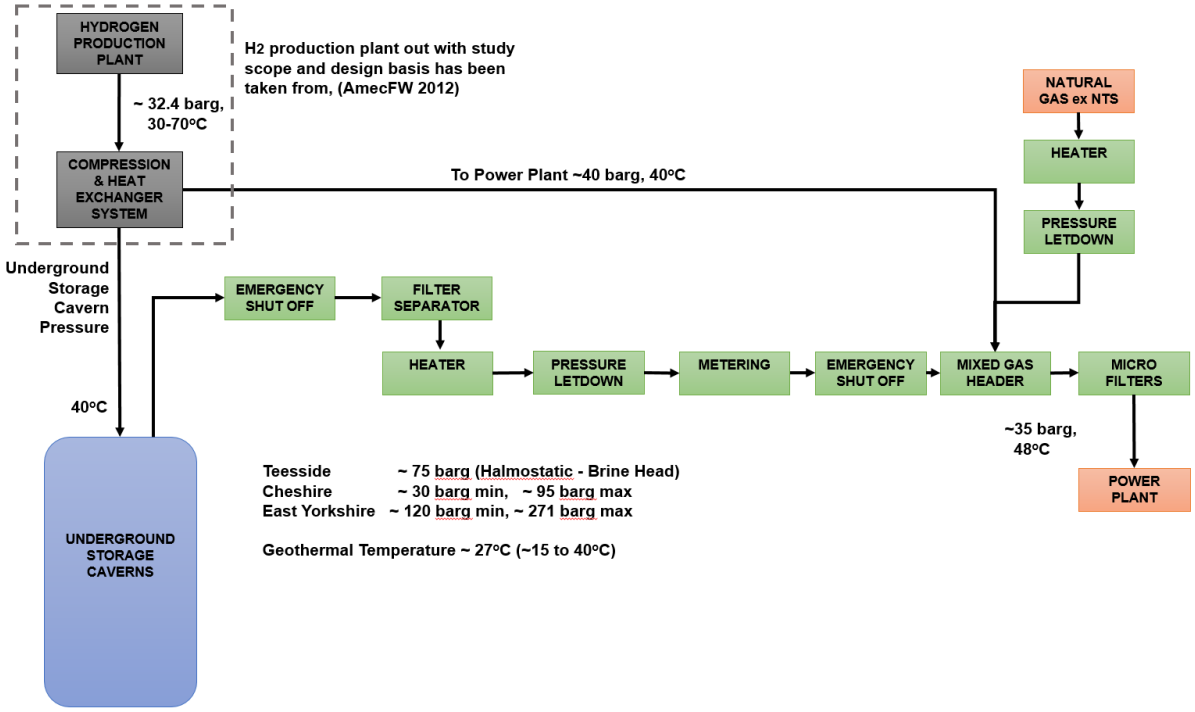

Figure C-1: Block flow diagram – H_2 treatment plant

C.1.2. Compression system

The compression system at the outlet of the hydrogen production plant will preferably be capable of delivering hydrogen product at circa 20 barg to 35 barg for the power plant and at a higher pressure for underground storage (up to circa 271 barg dependent on location). Design for delivery at only the underground storage pressure will have an associated energy penalty as the pressure will need to be let-down again prior to entry to the power plant.

C.1.3. Hydrogen treatment plant

The hydrogen currently stored in underground salt caverns in the UK and in the US is high purity and is used as a chemical feedstock to processing plants. It is not used as a fuel supply for GTs. The hydrogen product stream from the hydrogen production plant is stored at pressure and will pick up moisture in the cavern (this is the case for both wet and dry storage).

Given the fuel specification requirements for the GTs within the power plant, the stored hydrogen product will need to be dried, let-down in pressure and heated prior to entering the power plant.

C.1.4. Process integrity aspects

The following are anticipated from a process integrity perspective

- Emergency shut off facilities on the hydrogen stream leaving the storage cavern at the inlet to the hydrogen treatment area to allow isolation.

- Emergency shut off facilities on the hydrogen stream leaving the hydrogen treatment area to allow isolation.
- Overpressure protection for any low pressure systems downstream of the pressure let-down facility to protect them in the event of failure of the let-down. The GTs themselves will be low pressure.

Emergency shut-off facilities for gas systems are typically automated double block and bleed; two trip valves with a vent in between, the vent itself fitted with a trip valve and routed to a safe location. For hydrogen streams, in particular the 89 mol% stream, additional design consideration needs to be given to the selection and number of valves required to achieve a low leakage / high system integrity. In terms of venting, design consideration would need to be given to the potential for the hydrogen to ignite (e.g. friction, static) as it is vented.

In terms of overpressure protection, onshore systems typically include a combination of both high integrity safety instrumented systems and mechanical pressure relief devices. The venting location of any pressure relief device outlets would need to be given careful consideration in terms of hydrogen content. For the overall facility including the production plant a dedicated common vent system and stack may be the preferred approach.

C.1.5. Gas hydrates

Methane hydrates (CH_4. nH_2O) are a common concern in high pressure natural gas storage, treatment and distribution systems due to their formation and stability at the handling pressures even at temperatures above 0°C. They are a crystalline substance of water and methane formed under higher pressure that can cause blockages. Methanol injection is typically available as a preventative measure in natural gas systems but not always employed. Hydrogen hydrates are not formed / stable at gas storage conditions less than 500 barg and methanol injection is not required provided that there is no significant methane in the system. Carbon dioxide and nitrogen can also form stable hydrates but these are unstable at geothermal storage temperatures and methanol injection is not considered to be required. Methanol adsorption is preferential to water adsorption in molecular sieve beds so it is important to understand if injection is or is not required in terms of gas drying technology selection. It is not currently anticipated that the proposed streams 1 and 2 (89 mol% H_2 from biomass and 53 mol% H_2 from ATR) will form hydrates under the proposed storage conditions and therefore methanol injection is not currently considered to be required.

C.1.6. Gas drying

The first step in the hydrogen treatment plant would be removal of any free water and particulates in a simple knock-out drum / scrubber arrangement. A disposal route / user would be required for the liquids collected. Table C-1 gives an indication of the mass of liquid produced from the two saturated hydrogen product streams in a separator, fed with gas at storage conditions (without additional moisture from the cavern). In the Teesside location where the underground storage caverns would be wet, significantly more liquids are likely to be produced than those shown.

Table C-1: Estimated mass of liquid produced for each type of fuel

Parameter	Teesside	Cheshire	East Yorkshire
Storage Pressure	75.5 barg	95 barg	271 barg
Geothermal Storage Temperature (typical)	27°C	27°C	27°C
Liquid per 1000 kg/hr Biomass hydrogen	2.9 kg/hr	3.2 kg/hr	3.7 kg/hr
Liquid per 1000 kg/hr ATR hydrogen	1.5 kg/hr	1.6 kg/hr	1.5 kg/hr

Further drying of the hydrogen product is then required to meet GT requirements and potentially avoid icing on high pressure let-down. The design pressure for gas drying will be dependent on the drying

technology selected and the available underground storage pressure. Initial pressure let-down may be required prior to gas drying with this being more likely if the storage location is in East Yorkshire (271 barg). The main gas drying technology options include:

- Glycol dehydration.
- Molecular sieve beds.
- Silica gel beds.
- Pressure swing adsorption.
- Membrane separation.
- Twister cyclonic gas / liquid separation.

Glycol dehydration and molecular sieve beds are the most widely used in gas storage applications. Twister is a newer and less well established technology but may be a favourable option given the high storage pressures relative to the power plant pressure requirements.

- Glycol systems are in general more complex, have higher operating costs, cannot achieve fast starts and are not a Best Available Technology in terms of emissions.
- Molecular sieve beds would typically operate cyclically with one or more beds on line and the other(s) being regenerated using a hot gas. A regeneration heater is therefore also required to heat the regeneration gas (which could be process gas or natural gas).
- Twister operates on the principle of expansion followed by cyclonic gas/liquid separation followed by re-compression. It can only work where there is at least circa 30 barg to 70 barg pressure differential between storage and user pressure and is not normally economical below that.

The technology selection decision will in part be dependent on the volume of gas to be treated with molecular sieve beds tending to be used on smaller facilities. Dependent on location and storage pressure, Twister may be favoured.

C.1.7. Pressure let-down

The pressure required at the power plant to the inlet to the GTs is of the order of 20 to 35 barg. Teesside and East Yorkshire caverns indicatively operate significantly above these pressures. In terms of Cheshire, operating at the minimum cavern operating pressure (circa 30 barg) could mean a pressure supply lower than that required by selected GT technology taking into account pressure loss through the drying section. From a design concept / capital perspective, it would be better to avoid the requirement for a compressor between the drying section and power plant either by limiting the minimum cavern pressure and / or GT technology selection.

In terms of pressure let-down, there are two main technologies:

- Turbo expander.
- Pressure control valves / throttle valves.

A turbo expander would allow the recovery of additional power and as such would likely be preferred for Teesside and East Yorkshire based on indicative cavern pressures. In terms of Cheshire, a turbo expander at the maximum pressure would look advantageous. Ultimately, technology selection would be based on installed cost and benefits, the turbo expander being more capital intensive but providing better energy efficiency / power generation. A turbo expander would to be paired with a small pressure reduction control valve to achieve final pressure.

C.1.8. Heater

Although pure hydrogen itself increases in temperature when reduced in pressure in a Joule-Thomson process (isenthalpic expansion) starting at ambient temperature, the hydrogen product from the hydrogen production plant will overall cool after pressure let-down. Conceptually, heating is then

required to meet turbine inlet requirements; superheat to circa 10°C to 30°C above the hydrocarbon dew point. The technology typically employed for heating is a water bath heater where the water is heated with process gas. The table below gives a conceptual indication of the temperatures of the hydrogen product after pressure let-down. It is based on the worst case of maximum storage pressure and minimum (15°C) to typical (27°C) geothermal temperature.

Table C-2: Indication of the temperatures of the hydrogen product after pressure let-down

Parameter	Teesside	Cheshire	East Yorkshire
Storage pressure	75.5 barg	95 barg	271 barg
Geothermal storage temperature	15°C to 27°C	15°C to 27°C	15 to 27°C
Outlet pressure of let-down	20 barg	20 barg	20 barg
Biomass hydrogen temperature after pressure let-down	14°C to 26°C	13°C to 25°C	13°C to 25°C
ATR hydrogen temperature after pressure let-down	10°C to 23°C	9°C to 21°C	2°C to 15°C

C.1.9. Metering

Metering from storage will be required for a number of reasons, namely;

- For fiscal measurement purposes.
- To ensure that the hydrogen treatment plant is operated within its design envelope.
- For operational performance and control.
- Good practice / general loss control.

Given the importance of the metering, typically a back-up system is also installed. The metering is conceptually shown at the inlet to the power plant but the location and technology would be optimised during development of the design. Additional non fiscal flow metering may be required e.g., at the inlet to the hydrogen treatment plant.

C.1.10. Microfiltration

Microfiltration is recommended to achieve removal of all particulates in the gas supply to the GTs within the power plant.

C.1.11. Natural gas blending

The GT fuel options include blending natural gas with the biomass produced hydrogen stream; 60mol% and 25mol% biomass produced hydrogen product blended in natural gas.

Typically, blending would be carried out using a control scheme by ratio control of metered hydrogen product and metered natural gas. An in-line pipe mixer may also be required.

Blending is currently proposed downstream of the heater but upstream of the microfiltration. The location would be optimised during design development.

C.1.12. Operating mode of the overall facility

The three operating scenarios for the power plant all show power generation on a discontinuous/ intermittent basis.

In terms of the operational considerations for the overall facility;

- The hydrogen production plant would conceptually operate continuously with hydrogen product being fed to the power plant and / or underground cavern storage.
- The hydrogen treatment plant is only required to operate when the power plant is fed with hydrogen from storage.

If the Power Plant is only operational intermittently for periods of up to 12 hours, then this presents significant challenges for the design of the hydrogen treatment plant. Due to the nature of the technology and the time taken to commission and achieve performance, it is not practical to design a hydrogen treatment plant for operation of up to 12 hours with starts and stops several times a day. The conceptual design solution would be to design the hydrogen treatment plant for continuous operation at low load by continuously generating a base load of power in the power plant and / or designing for continuous operation with a recycle. Designing the unit with a low turndown would reduce associated operating costs of continuous low load operation.

C.1.13. Material selection

Material selection has not been considered at this stage. There are specific considerations required for hydrogen duty due to hydrogen embrittlement and hydrogen attack. Each material to be used in the process should be carefully evaluated for its compatibility to hydrogen at the design, operating and emergency conditions to which it will be exposed. API RP 941 gives general guidance.

Hydrogen embrittlement

Some metallic materials used in vessels and equipment can undergo a significant loss in ductility when exposed to hydrogen. This is known as hydrogen embrittlement and occurs when hydrogen / hydrogen compounds permeate the lattice structure of the material. Material degradation induced by embrittlement can result in catastrophic failure of equipment. Proper design and selection of materials is required to counteract the risk of hydrogen embrittlement.

Hydrogen attack

Another form of hydrogen embrittlement is hydrogen attack which is a non-reversible degradation of the steel microstructure caused by a chemical reaction between the diffusing hydrogen and carbon in the steel. The severity of hydrogen attack increases with increasing temperatures and pressures.

ATKINS

Appendix D: Cavern storage

D.1. Cavern thermodynamics

The mathematical basis that characterises the thermodynamic behaviour of a salt cavern used for storage operations of gaseous products, has been presented in detail by Nieland (2008) and is presented in this appendix.

The gas storage capacity of a solution-mined cavern is governed by the gas equation-of-state, which for a real gas has been defined as:

$$m = \frac{V\ p\ M}{Z\ R\ T}$$ **Equation D1**

where:

m = mass of stored gas
V = cavern volume
p = absolute gas pressure in the cavern
M =molecular weight of the gas
Z = compressibility factor of the gas
R = universal gas constant
T = absolute temperature of gas.

Neglecting creep closure, the storage volume of a cavern is fixed after leaching is competed. The gas storage pressure range is generally fixed based on geomechanical stability of the cavern, regulation, or by compressor capacity. The molecular weight of the gas is dependent on gas composition and generally remains relatively constant. The compressibility factor is a function of the gas temperature, gas pressure, and gas composition. The only variable that is not generally known during the design stage is temperature. The gas temperature in a storage cavern is dependent on the storage pressure cycle, gas injection temperature, temperature of the host salt, and the thermodynamic properties of the stored gas.

The thermodynamic processes involved in a gas storage cavern include the heating and cooling caused by gas compression and expansion, heat transfer between the gas and the surrounding rock, and energy changes caused by mass flow into and out of the cavern. The following equation represents the time rate of change of the bulk or average cavern gas temperature and is used to describe the energy balance in a gas storage cavern:

$$\frac{dT}{dt} = \frac{1}{\rho\ V\ c_v}\left[\frac{V\ T}{\rho}\left(\frac{\partial P}{\partial T}\right)\frac{d\rho}{dt} + A\ q_c + \dot{m}\ c_p\ (T_\theta - T)\right]$$ **Equation D2**

where:

T = bulk cavern temperature
t = time
ρ = bulk density of the gas in the cavern
c_v = constant-volume specific heat of the gas
V = cavern storage volume
p = cavern pressure
A = surface area of cavern
q_c = heat flux at cavern wall
$\dot{m}$ = mass flow rate of gas entering cavern
c_p = constant-pressure specific heat of gas entering cavern
T_θ = temperature of gas entering cavern.

The first term on the right-hand side of the energy balance equation is the energy change related to the compression/expansion of the natural gas. As gas is injected into a cavern, the gas in the cavern is compressed and its temperature and pressure increase. During gas withdrawal, the gas in the cavern expands and its temperature and pressure decrease.

The second term on the right-hand side of the energy balance equation represents the change in energy caused by heat transfer with the surrounding salt. If the temperature of the gas is greater than that of the surrounding salt, heat will be transferred from the gas to the salt. Heat will be transferred from the salt to the gas if the gas temperature is lower than that of the salt. The heat flux into the cavern at the cavern wall is described by:

$$q_c = h(T_w - T_c) = -k\frac{dT}{dr}$$ **Equation D3**

where:

h = convective heat transfer coefficient
T_w = cavern wall temperature
T_c = bulk cavern gas temperature
k = salt thermal conductivity
$\frac{dT}{dr}$ = temperature gradient in the salt at the cavern wall.

The convective heat transfer coefficient used in the thermodynamic analysis is based on free convection in a vertical cylinder (Kreith & Black, 1980) and is given by:

$$h = 0.1\left(\frac{\beta\ g\ \rho^2(T_w - T_c)\ c_p\ k^2}{\mu}\right)^{\frac{1}{3}}$$ **Equation D4**

where:

T_w = cavern wall temperature
T_c = bulk cavern temperature
k = thermal conductivity of the gas
β = coefficient of volume expansion of the gas = $\frac{1}{v}\left(\frac{\partial v}{\partial T}\right)_p$
v = specific volume of gas (1/ρ)
g =gravitational acceleration
ρ = gas density
μ = dynamic viscosity of the gas
c_p = constant-pressure specific heat of the gas.

The final term on the right-hand side energy balance equation represents the energy change in the cavern because of mass flow into or out of the cavern.

D.2. Density and thermal properties of the East Yorkshire geological formations

Table D2-1: East Yorkshire goelogical formations density and thermal properties

Geological layer	Thickness of layer [m]	ρ density [kg/m^3]	k thermal conductivity [W/(m K)]	c specific heat capacity [J/(kg K)]	α_t coefficient of linear thermal expansion [10^{-6} K^{-1}]
Boulder Clay (Quaternary)	36.88	1950	2.5	800	-
Flamborough Chalk (Cretaceous)	506.58	1880	3.3	900	-
Lower Liassic Shales - Jurassic (Clays & Thin Limestones)	29.57	2400	1.2	920	-
Penarth Shales (Rhaetic Hard Shales)	17.07	2580	1.36	860	-
Mercia Mudstone (Keuper Mudstone)	143.87	2480	1.59	910	-
Muschelkalk (Dolomitic Shales)	62.48	2500	4.06	1180	-
Upper Bunter Shale	93.57	2400	1.97	840	-
Sherwood Sandstone (Middle Bunter Sandstone)	542.85	2450	2.24	868	-
Lower Bunter Shale	37.80	2400	1.71	860	-
Bröckelschiefer (Silty Sandy Shale)	29.87	2540	3.35	860	-
Zechstein IV Evaporite (Upper Halite)	28.65	2180	6.57	800	-
Upper Anhydrite (Sherburn Anhydrite)	8.84	2760	3.33	880	-
Carnallitic Marl	29.87	2300	1.83	900	8.5

Geological layer	Thickness of layer [m]	ρ density [kg/m^3]	k thermal conductivity [W/(m K)]	c specific heat capacity [J/(kg K)]	α_t coefficient of linear thermal expansion [10^{-6} K^{-1}]
Zechstein III Boulby Halite	18.29	2150	5.74	870	40.0
Zechstein III Billingham Anhydrite (Main Anhydrite)	5.49	2930	3.82	1050	20.0
Zechstein III Brotherton Formation (Upper Magnesian Limestone)	64.01	2420	2.40	890	11.3
Grauer Salzton (Grey Silty Halitic Clay)	5.49	2290	2.76	1187	7.9
Zechstein II Fordon Evaporites (Upper Halite)	10.55	2150	5.52	837	40.0
Zechstein II Fordon Evaporites (Anhydrite)	37.00	2900	3.82	1050	20.0
Zechstein II Fordon Evaporites (Main Salt)	151.00	2558	5.19	900	38.9
Zechstein II Fordon Evaporites (Polyhalite)	11.00	2770	2.00	860	24.0
Zechstein I Hayden Anhydrite	148.00	2940	3.33	880	20.0
Zechstein I Cadeby Formation (Dolomite rock)	99.29	2620	3.11	930	21.0

D.3. Density and thermal properties of the Cheshire geological formations

Table D3-1: Cheshire geological formation density and thermal properties

Geological layer	Thickness of layer [m]	ρ density [kg/m^3]	k thermal conductivity [W/(m K)]	c specific heat capacity [J/(kg K)]	α_t coefficient of linear thermal expansion [10^{-6} K^{-1}]
Glacial Till	18.00	1860	2.5	800	-
Sidmouth Mudstone Above	387.50	2498	1.47	650	9.0
Northwich Halite (layers I to D)	221.00	2174	5.74	900	32.0
30ft Marl (layer C)	11.80	2498	1.47	650	9.0
Nortwich Halite (layer B)	30.00	2174	5.74	900	32.0
Sidmouth Mudstone Below	282.20	2498	1.47	650	9.0

D.4. Contour diagrams for the East Yorkshire representative cavern concerning the temperature, minor σ_3 and major principal stresses, von Mises stress component σ_{vm} and vertical displacements u_y.

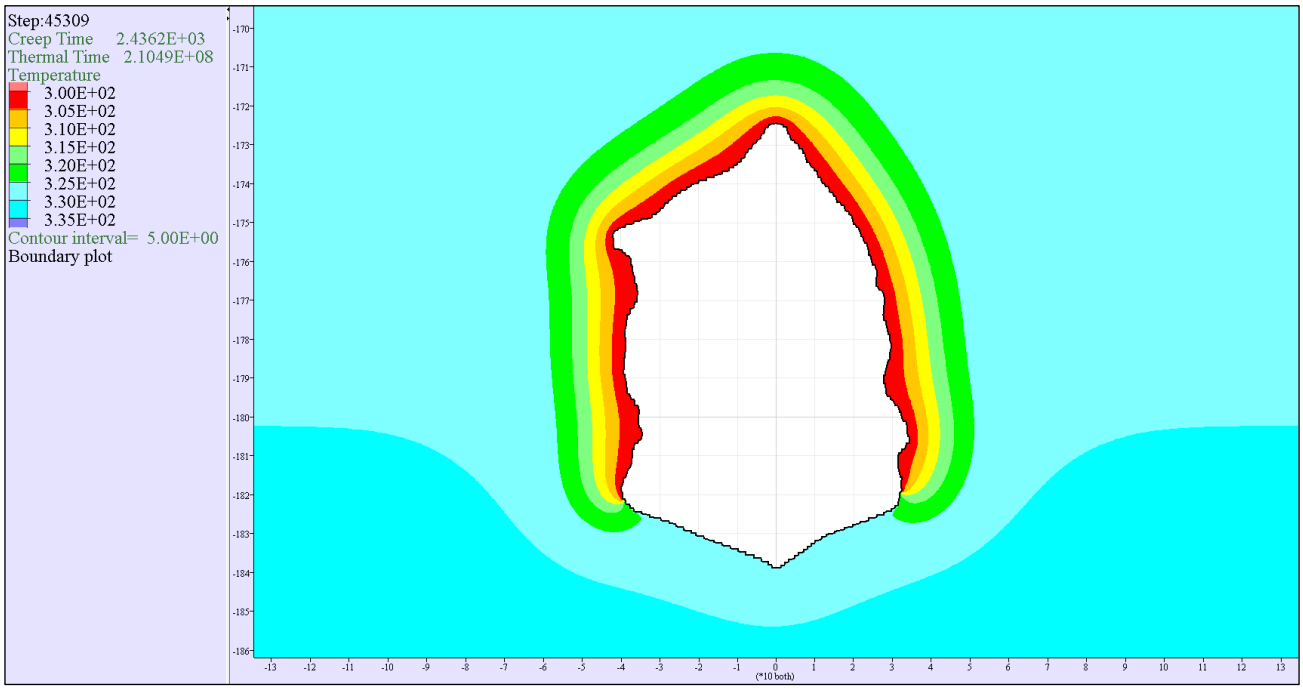

Figure D4-1: Distribution of temperature [expressed in K] around East Yorkshire representative cavern at the end of the cavern de-pressurisation phase

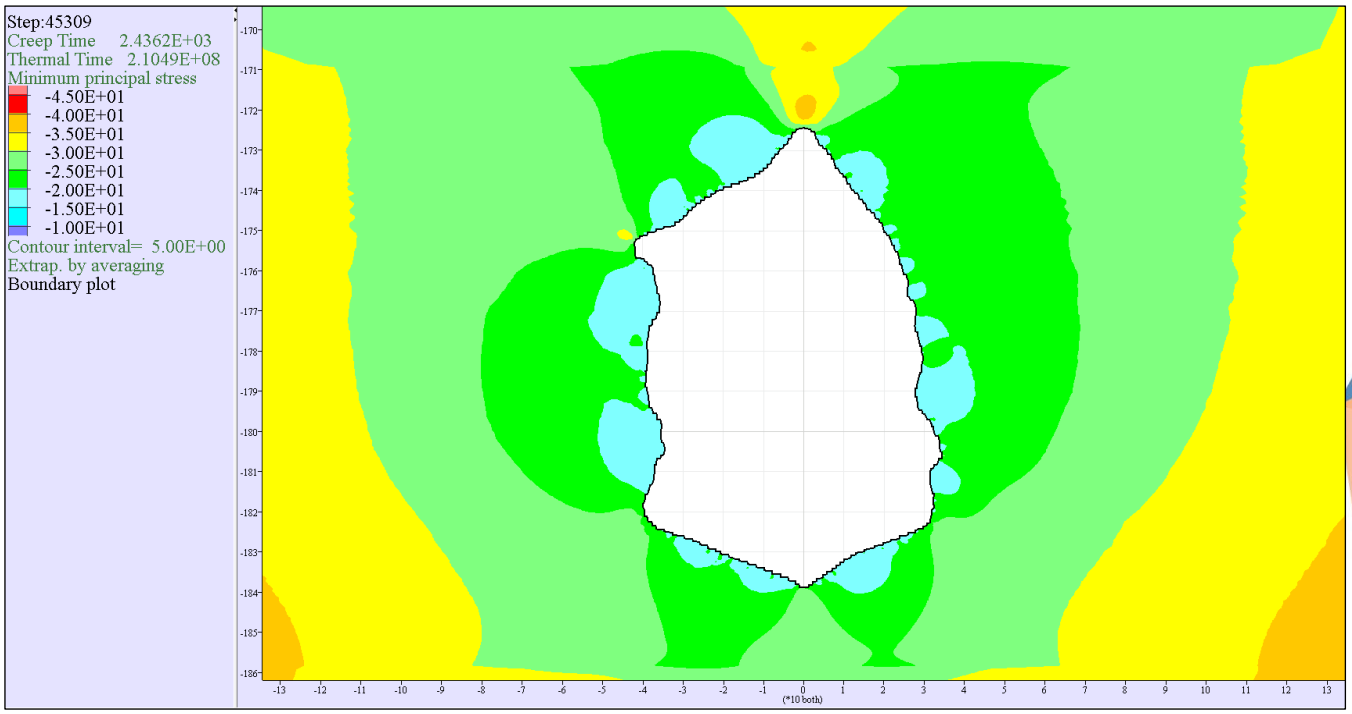

Figure D4-2: Distribution of minor principal stress [expressed in MPa] around East Yorkshire representative cavern at the end of the cavern de-pressurisation phase

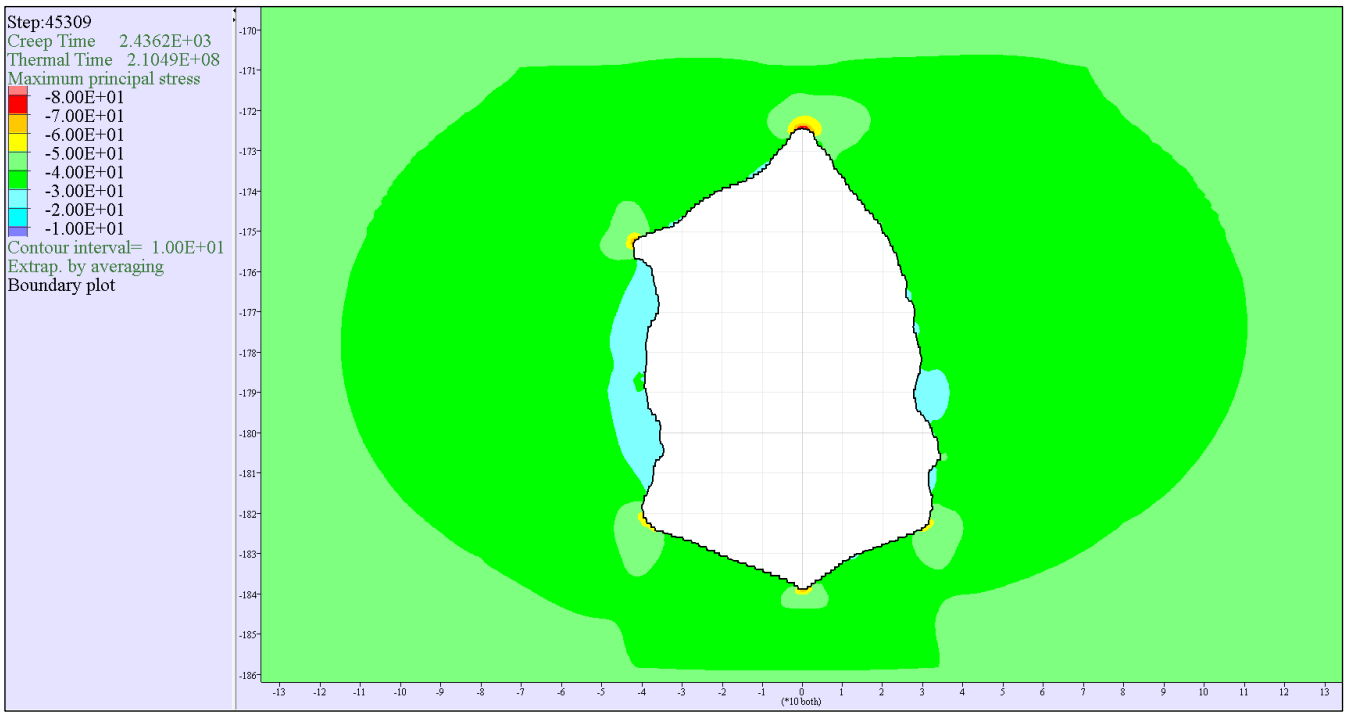

Figure D4-3: Distribution of major principal stress [expressed in MPa] around East Yorkshire representative cavern at the end of the cavern de-pressurisation phase

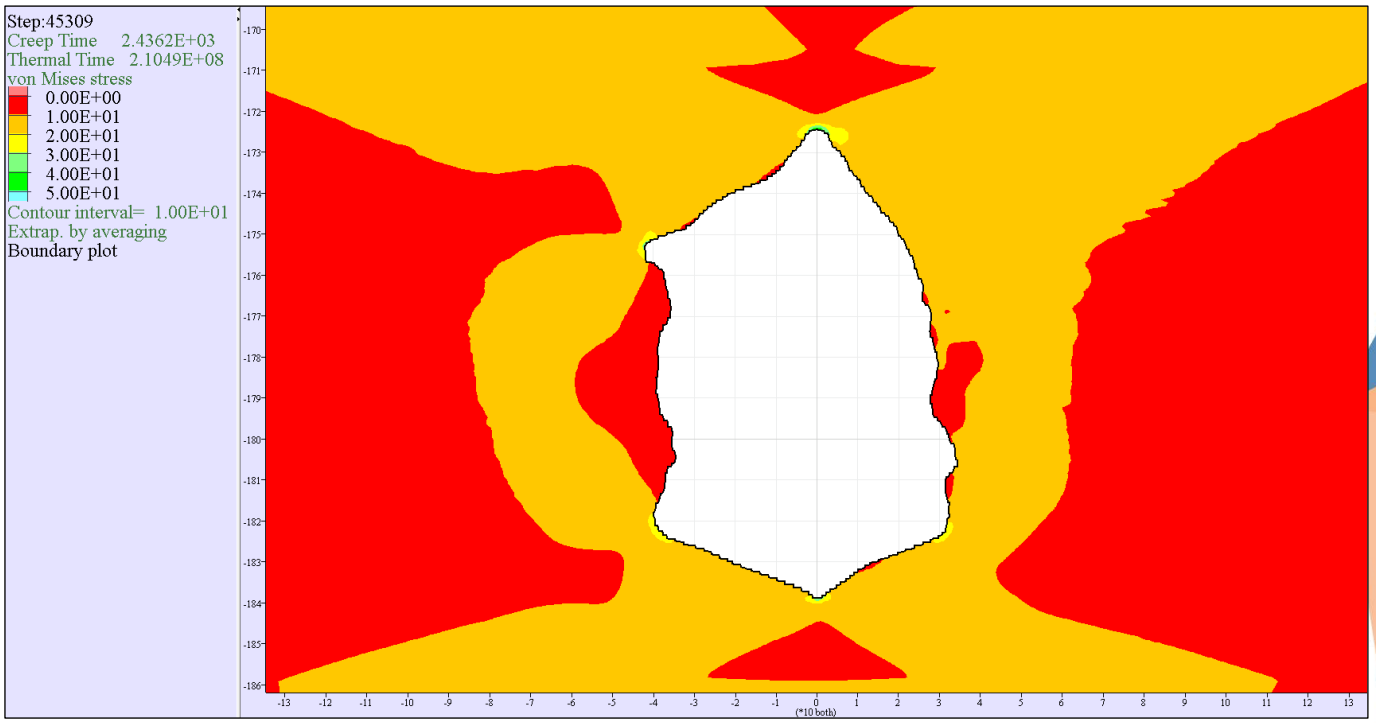

Figure D4-4: Distribution of von Mises stress [expressed in MPa] around East Yorkshire representative cavern at the end of the cavern de-pressurisation phase

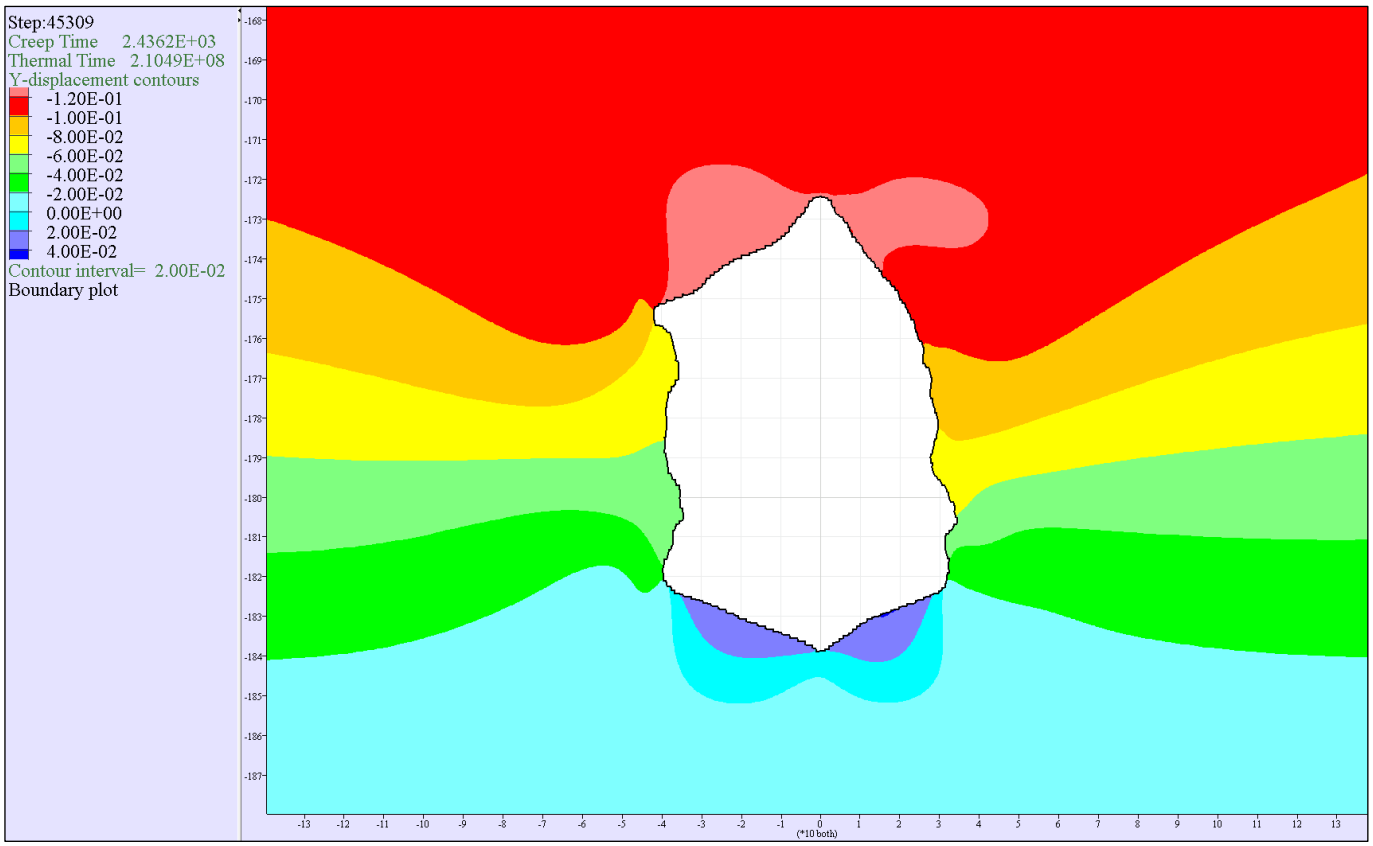

Figure D4-5: Distribution of vertical displacements [expressed in m] around East Yorkshire representative cavern at the end of the cavern de-pressurisation phase

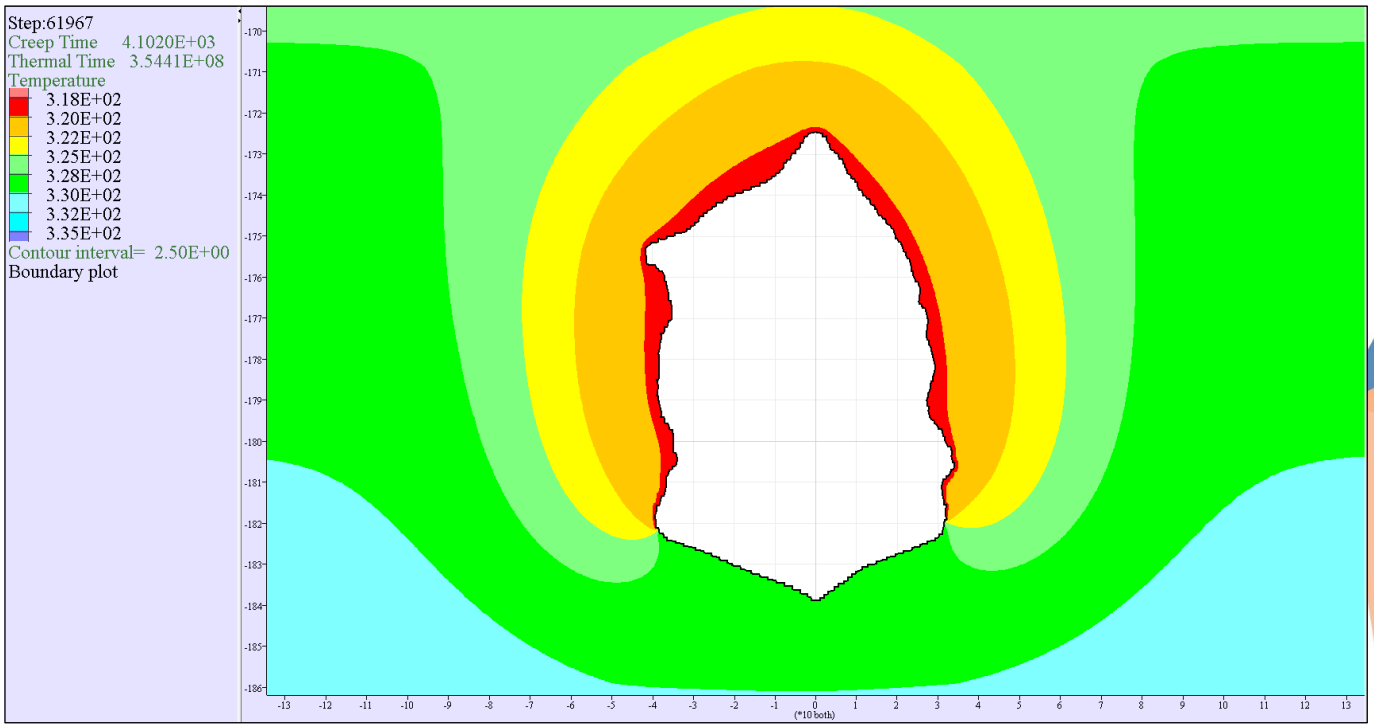

Figure D4-6: Distribution of temperature [expressed in K] around East Yorkshire representative cavern at the end of five years of cyclic loading

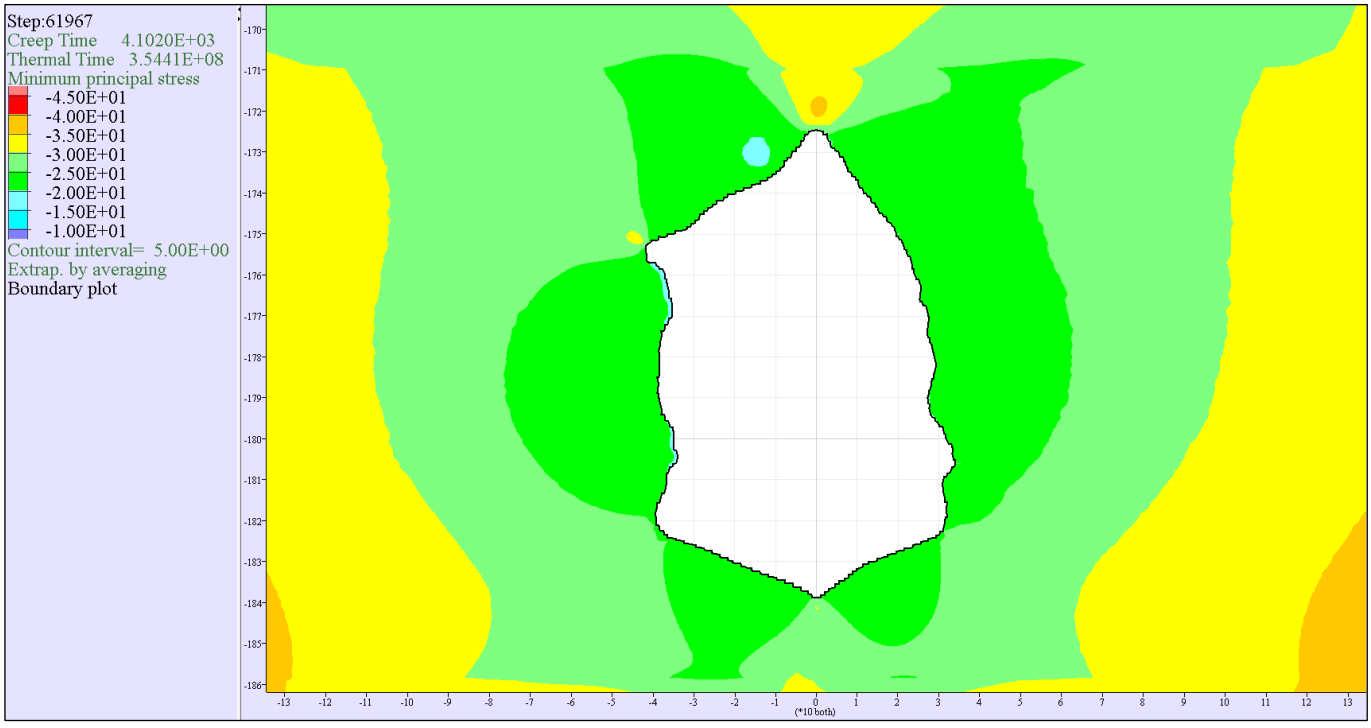

Figure D4-7: Distribution of minor principal stress [expressed in MPa] around East Yorkshire representative cavern at the end of five years of cyclic loading

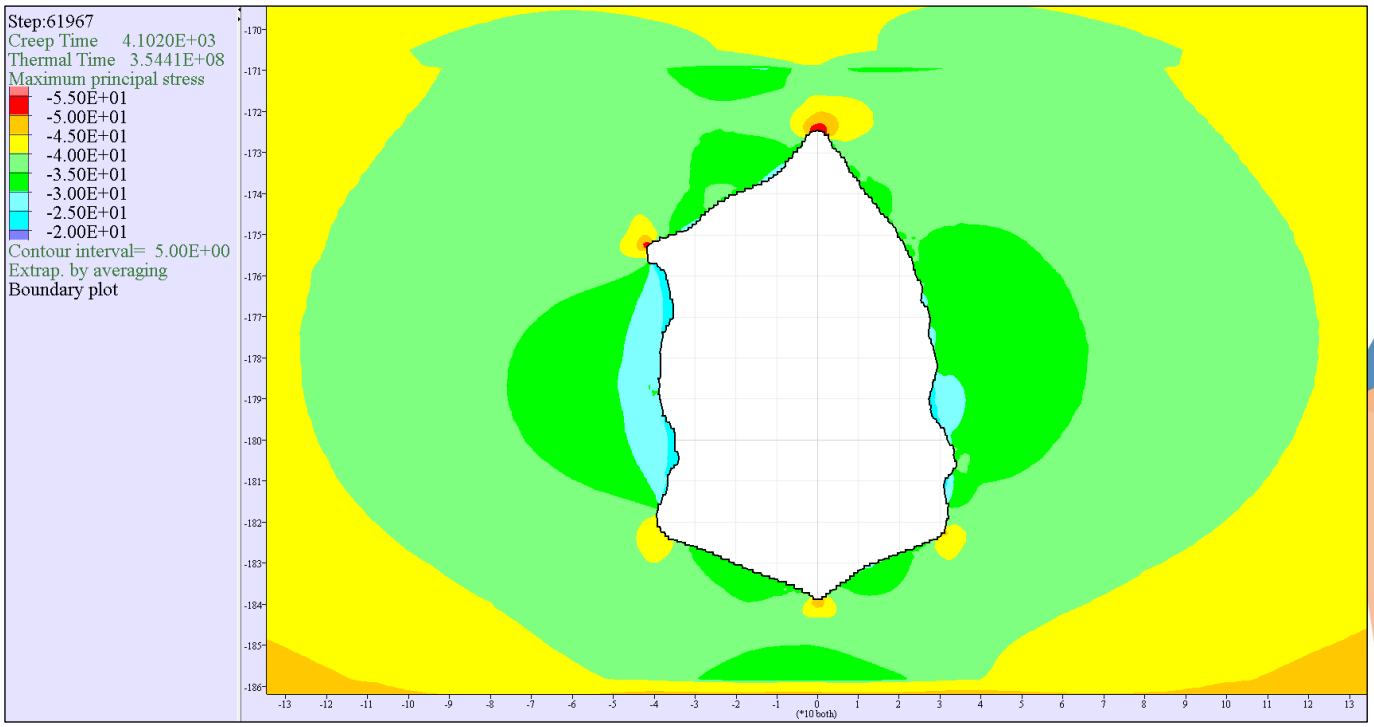

Figure D4-8: Distribution of major principal stress [expressed in MPa] around East Yorkshire representative cavern at the end of five years of cyclic loading

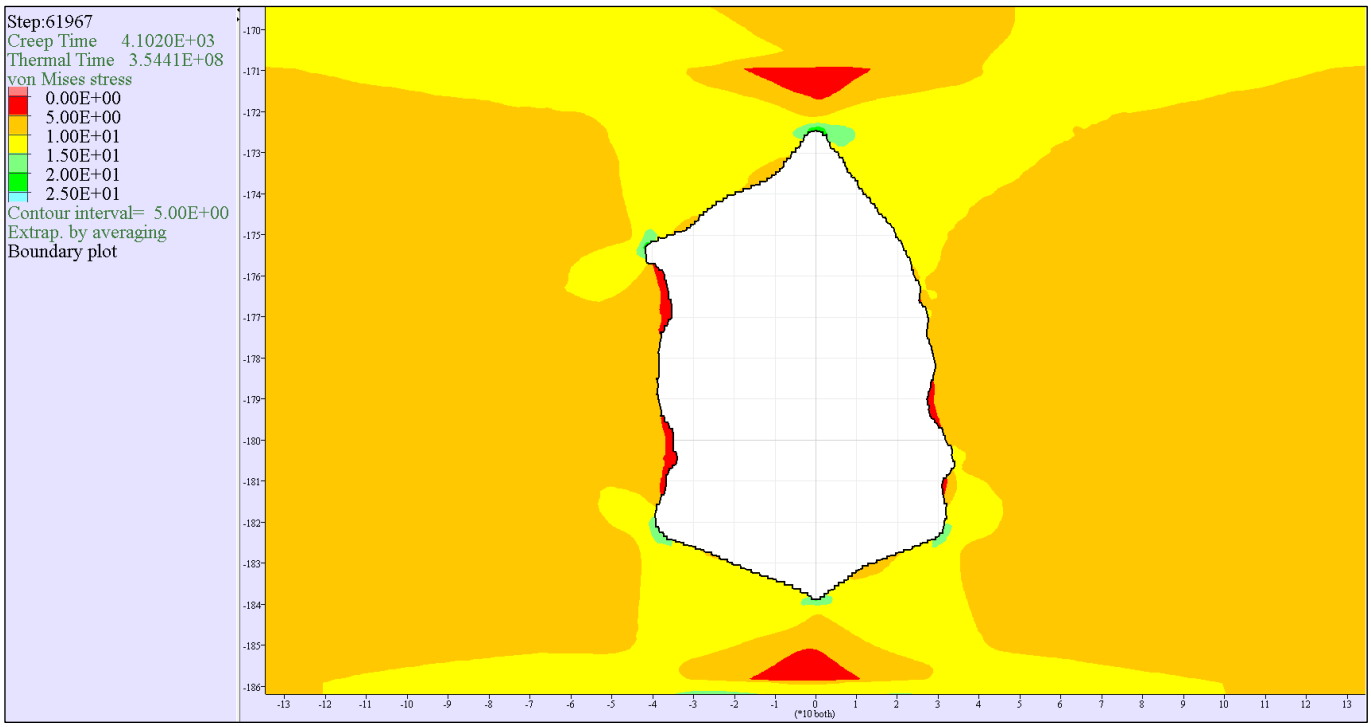

Figure D4-9: Distribution of von Mises stress [expressed in MPa] around East Yorkshire representative cavern at the end of five years of cyclic loading

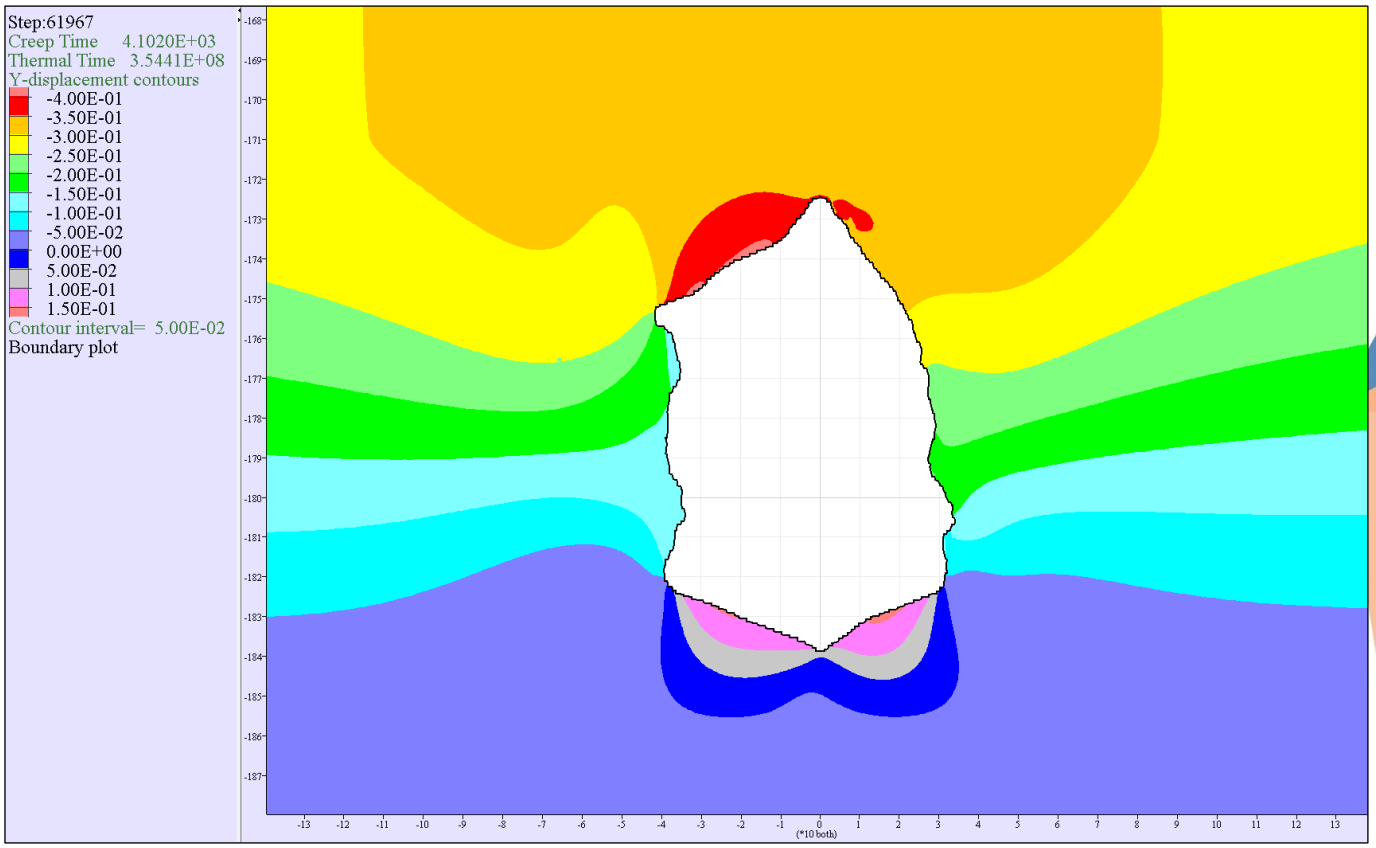

Figure D4-10: Distribution of vertical displacements [expressed in m] around East Yorkshire representative cavern at the end of five years of cyclic loading

D.5. Contour diagrams for the Cheshire representative cavern concerning the temperature, minor σ_3 and major principal stresses, von Mises stress component σ_{vm} and vertical displacements u_y.

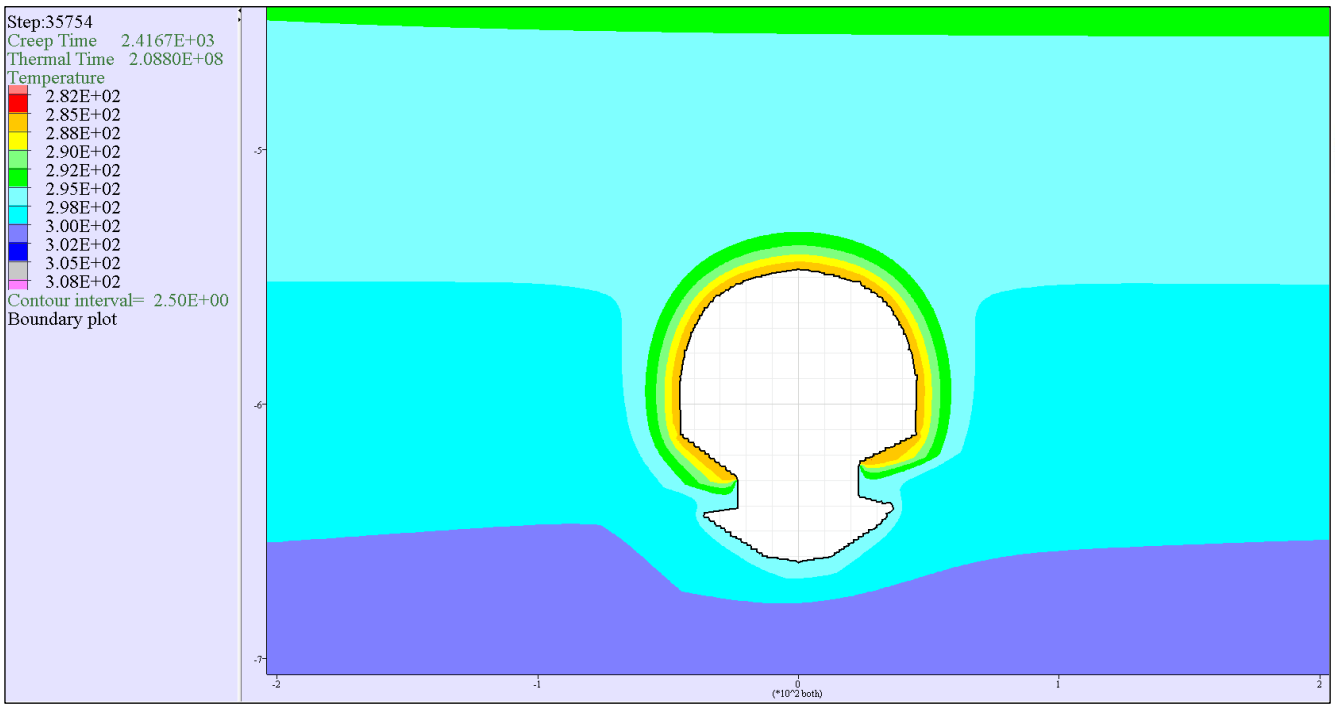

Figure D5-1: Distribution of temperature [expressed in K] around Cheshire representative cavern at the end of the cavern de-pressurisation phase

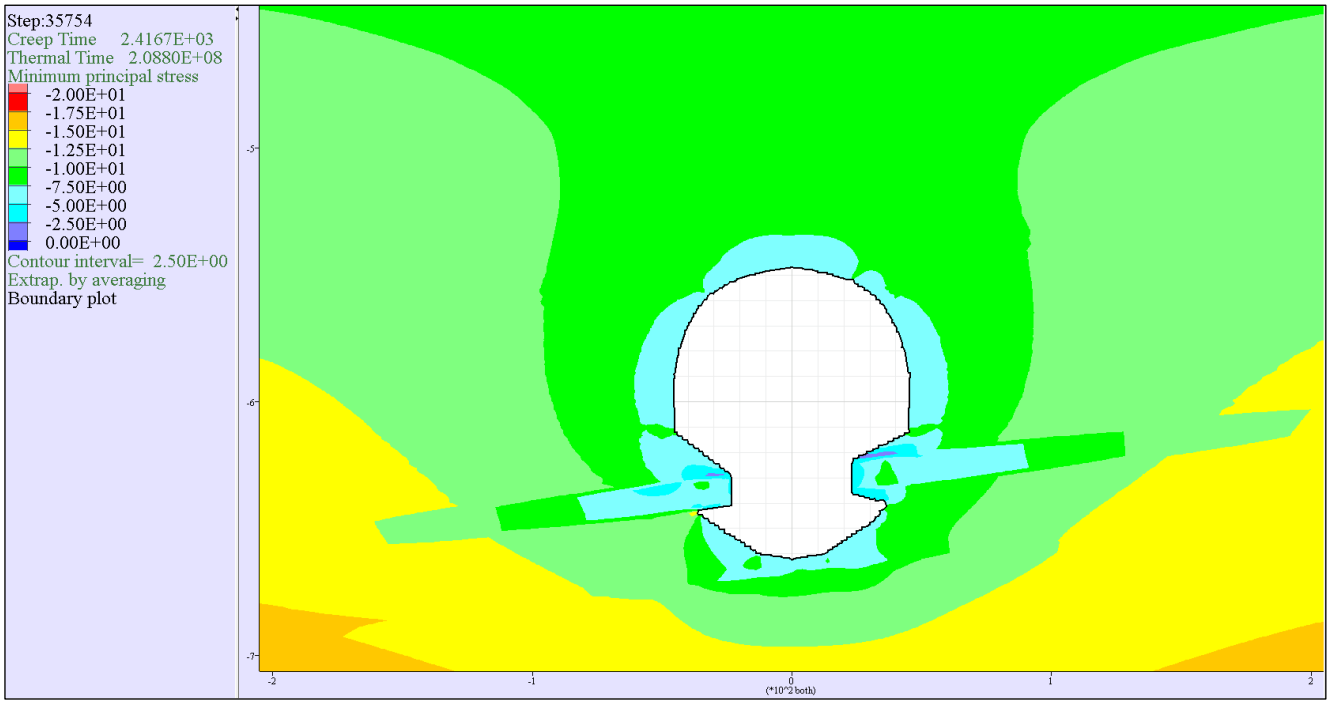

Figure D5-2: Distribution of minor principal stress [expressed in MPa] around Cheshire representative

cavern at the end of the cavern de-pressurisation phase

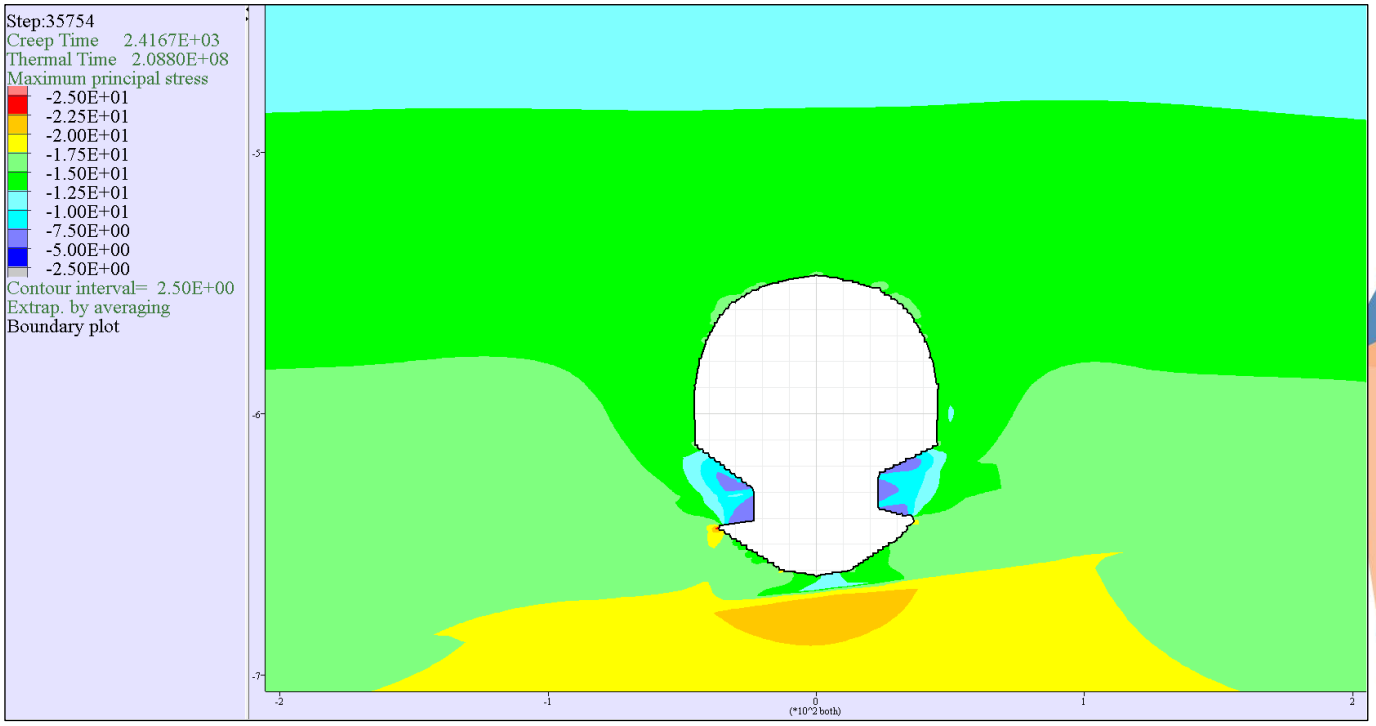

Figure D5-3: Distribution of major principal stress [expressed in MPa] around Cheshire representative cavern at the end of the cavern de-pressurisation phase

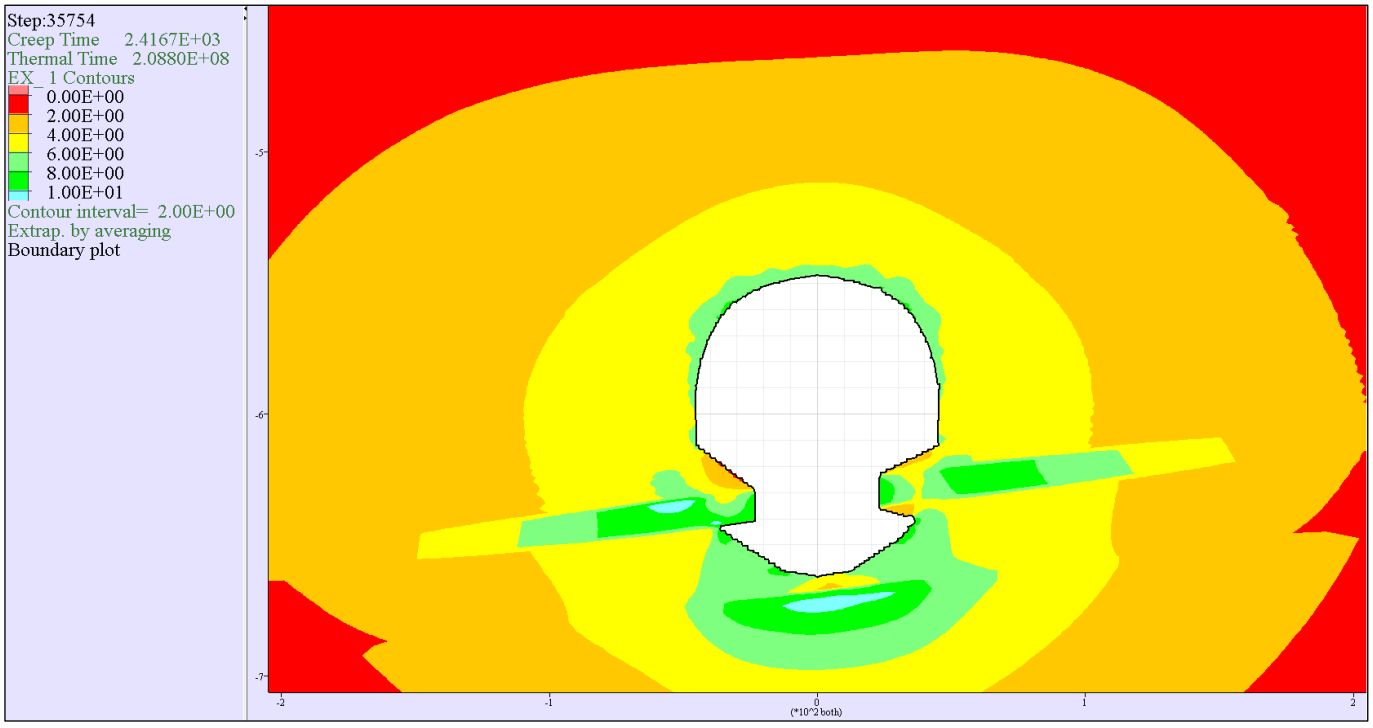

Figure D5-4: Distribution of von Mises stress [expressed in MPa] around Cheshire representative cavern at the end of the cavern de-pressurisation phase

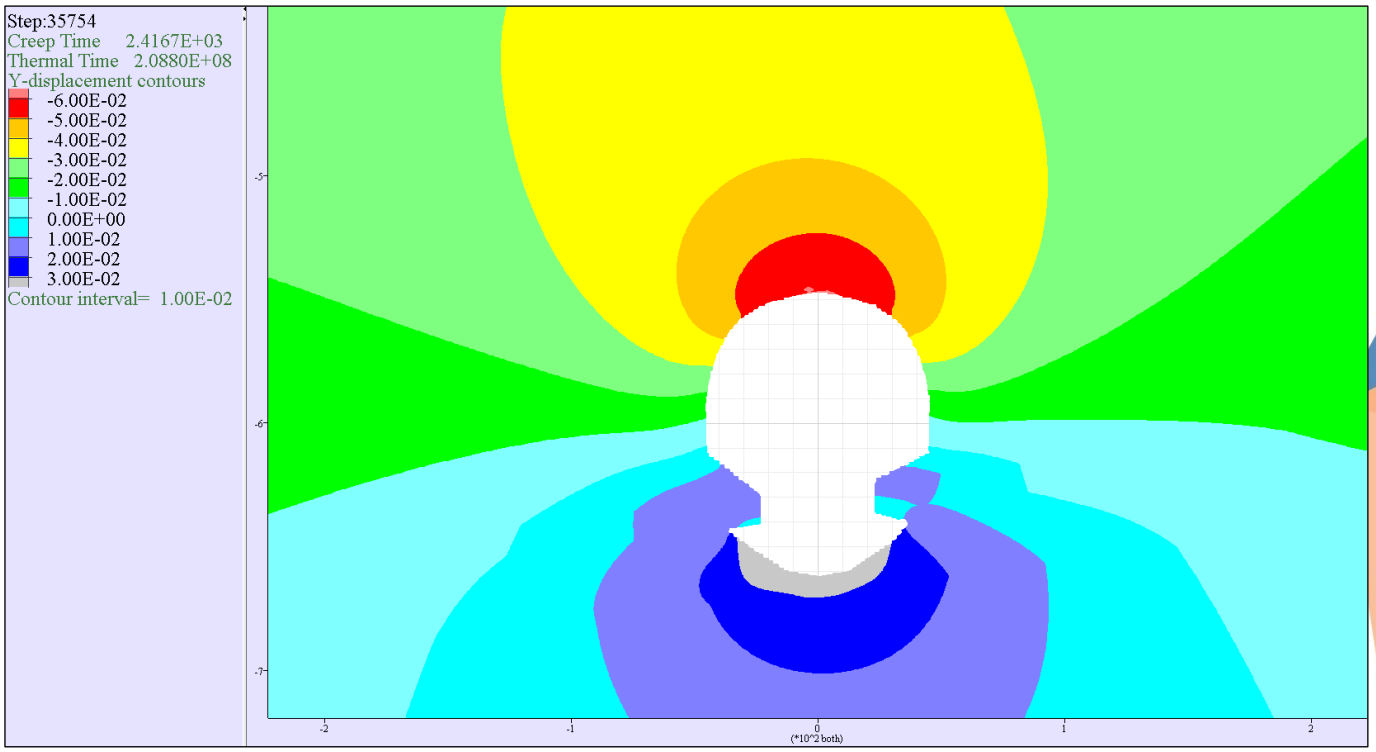

Figure D5-5: Distribution of vertical displacements [expressed in m] around Cheshire representative cavern at the end of the cavern de-pressurisation phase

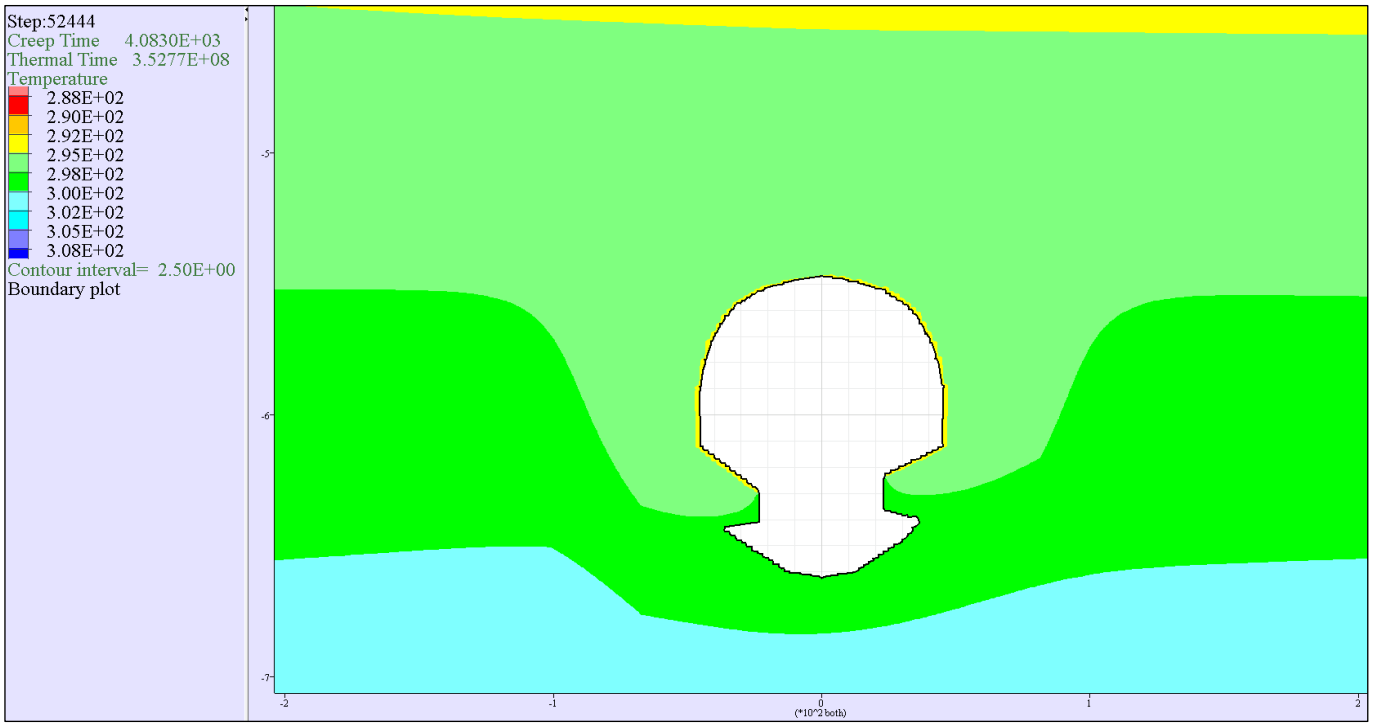

Figure D5-6: Distribution of temperature [expressed in K] around Cheshire representative cavern at the end of five years of cyclic loading

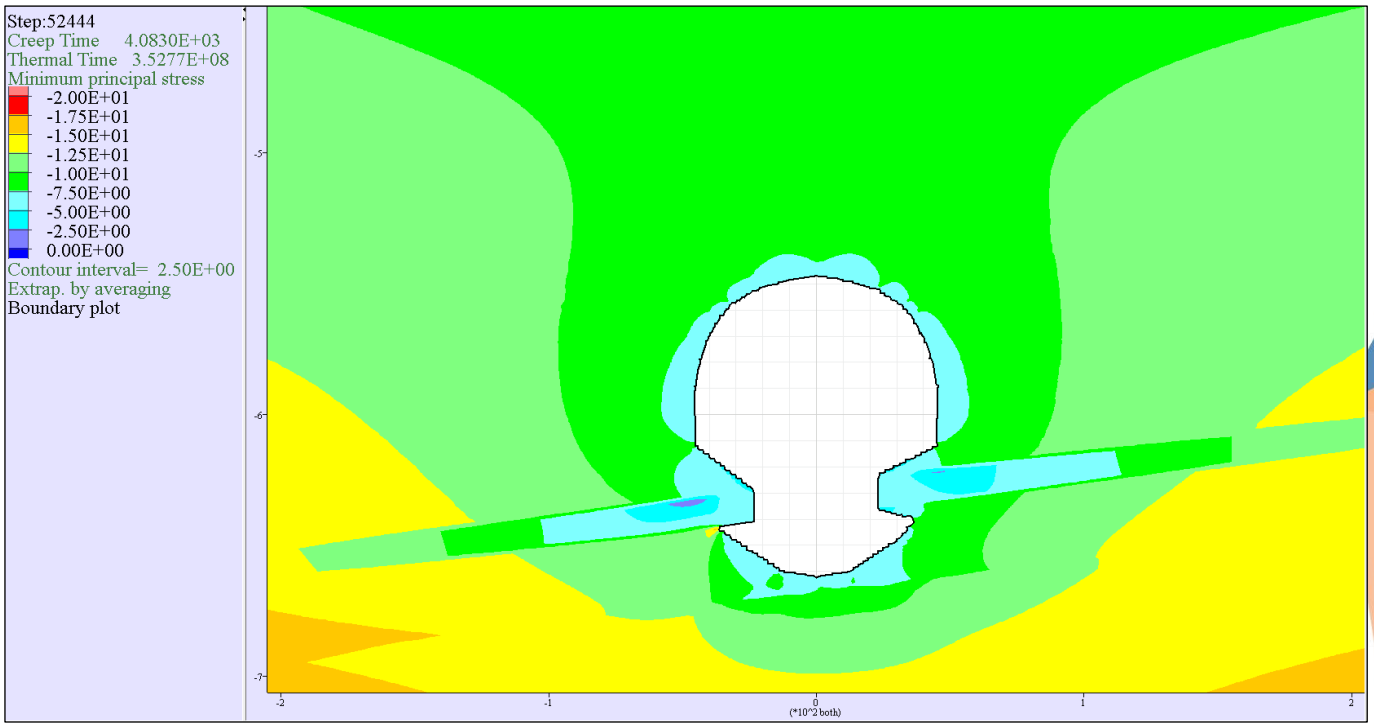

Figure D5-7: Distribution of minor principal stress [expressed in MPa] around Cheshire representative cavern at the end of five years of cyclic loading

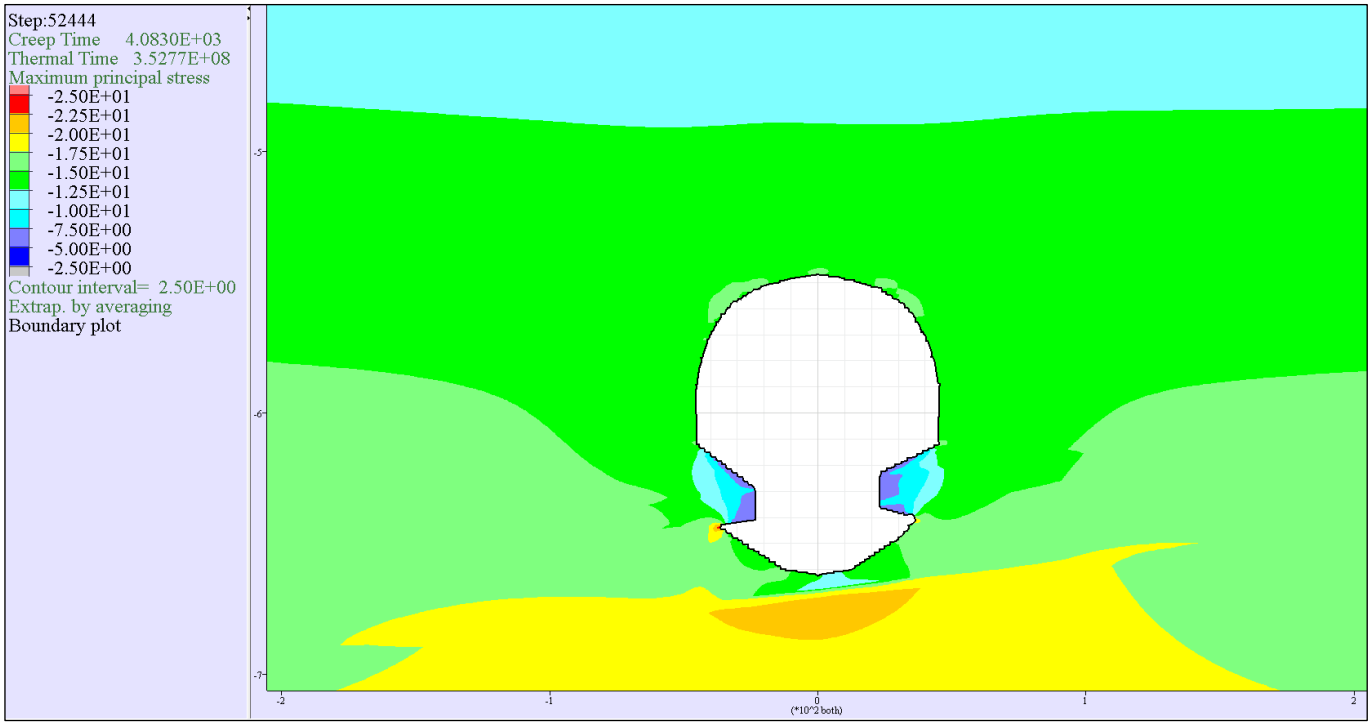

Figure D5-8: Distribution of major principal stress [expressed in MPa] around Cheshire representative cavern at the end of five years of cyclic loading

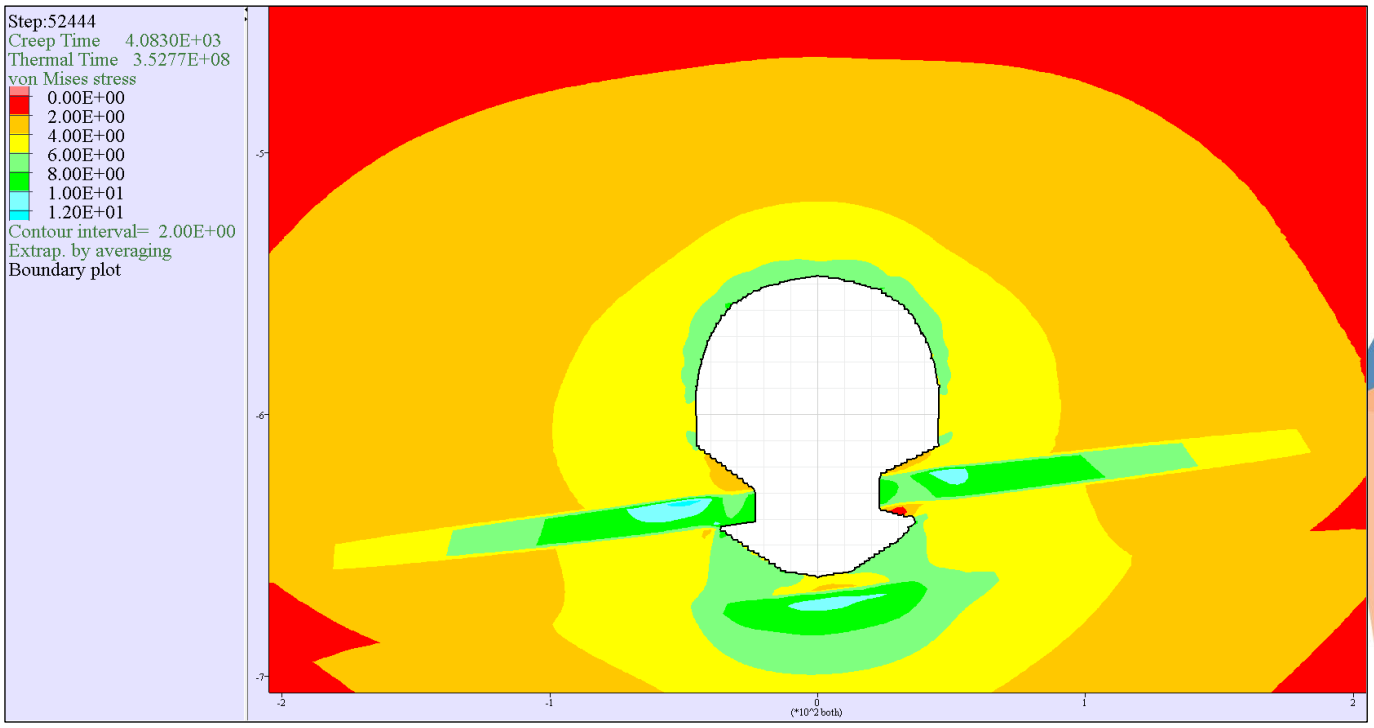

Figure D5-9: Distribution of von mises stress [expressed in MPa] around Cheshire representative cavern at the end of five years of cyclic loading

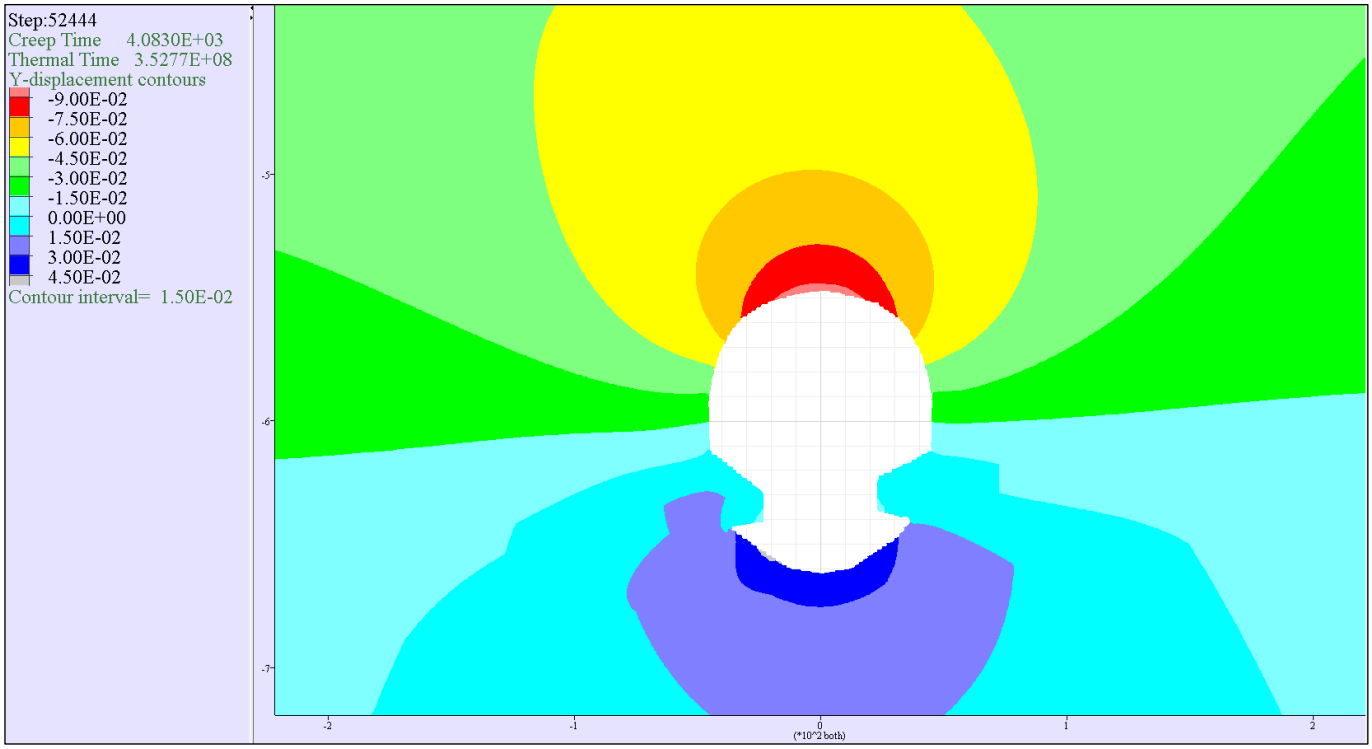

Figure D5-10: Distribution of vertical displacements [expressed in m] around Cheshire representative cavern at the end of five years of cyclic loading

D.6. Contour diagrams for the Teesside representative cavern concerning the minor σ_3 and major principal stresses, von Mises stress component σ_{vm} and vertical displacements u_y. and *Strength Factor*

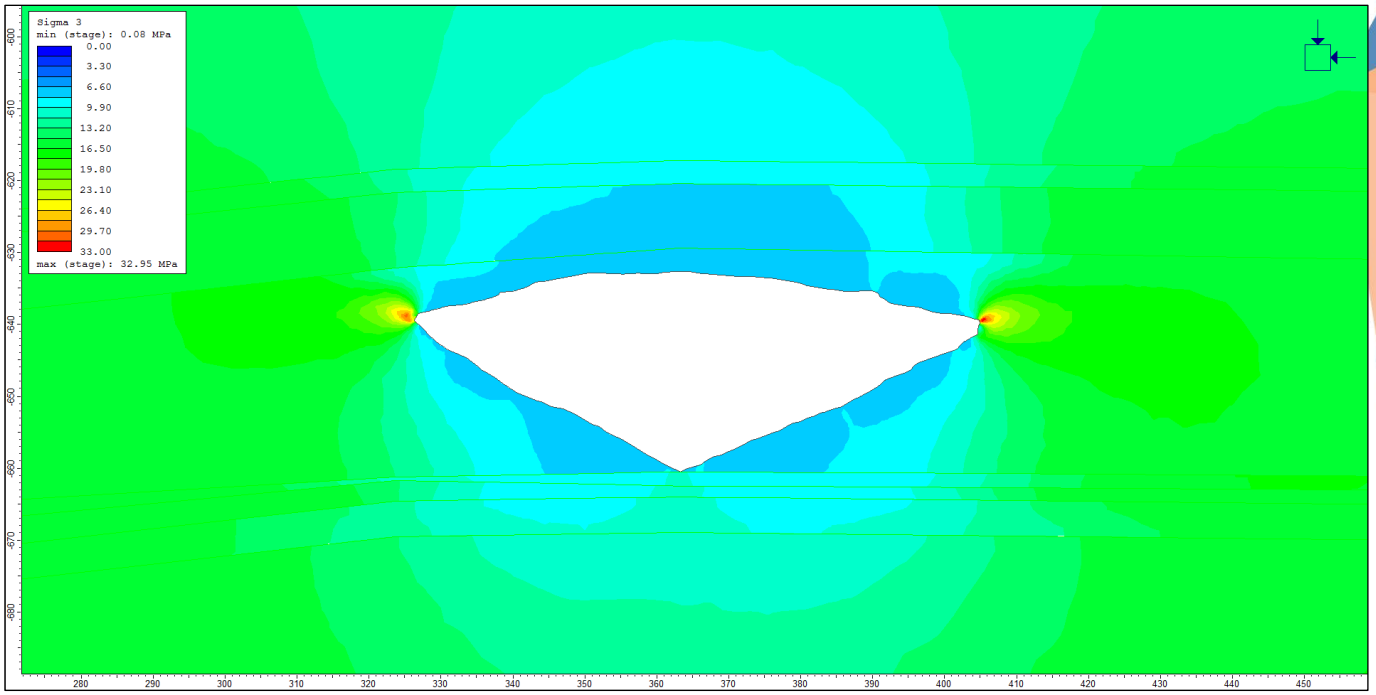

Figure D6-1: Distribution of minor principal stress [expressed in MPa] around Teesside representative

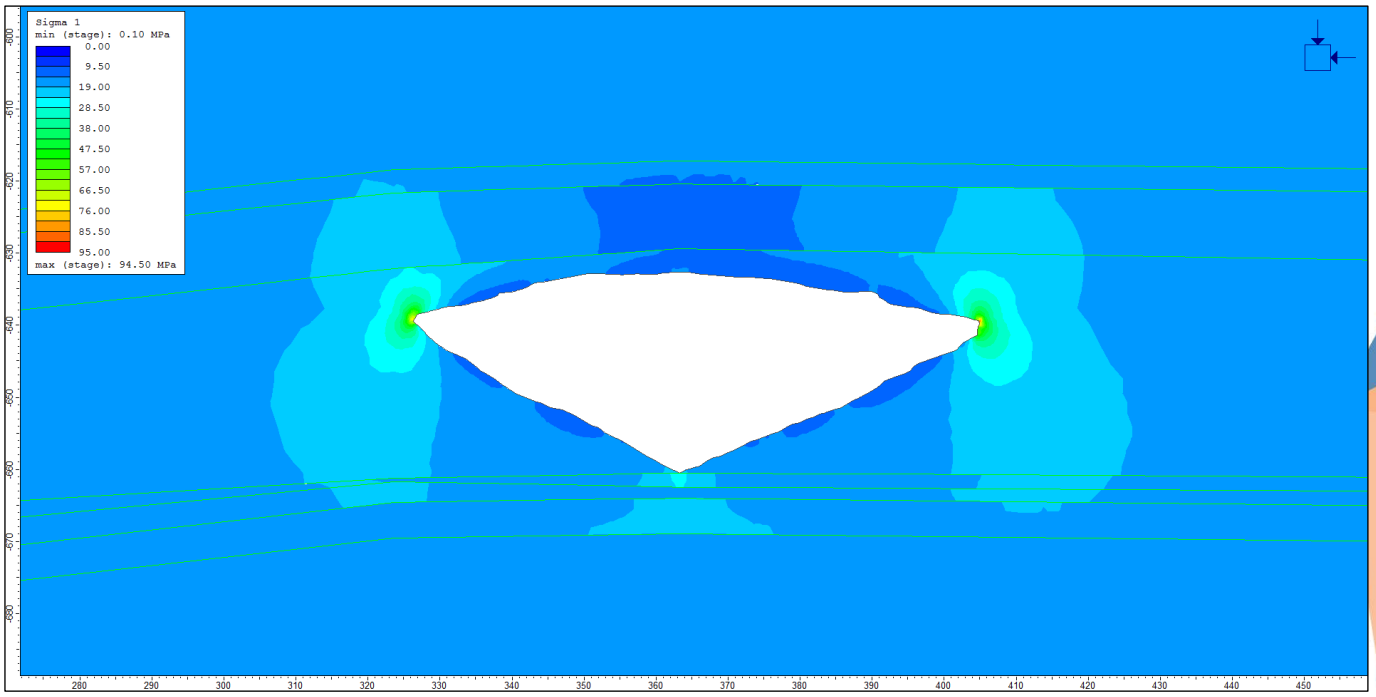

Figure D6-2: Distribution of major principal stress [expressed in MPa] around Teesside representative cavern

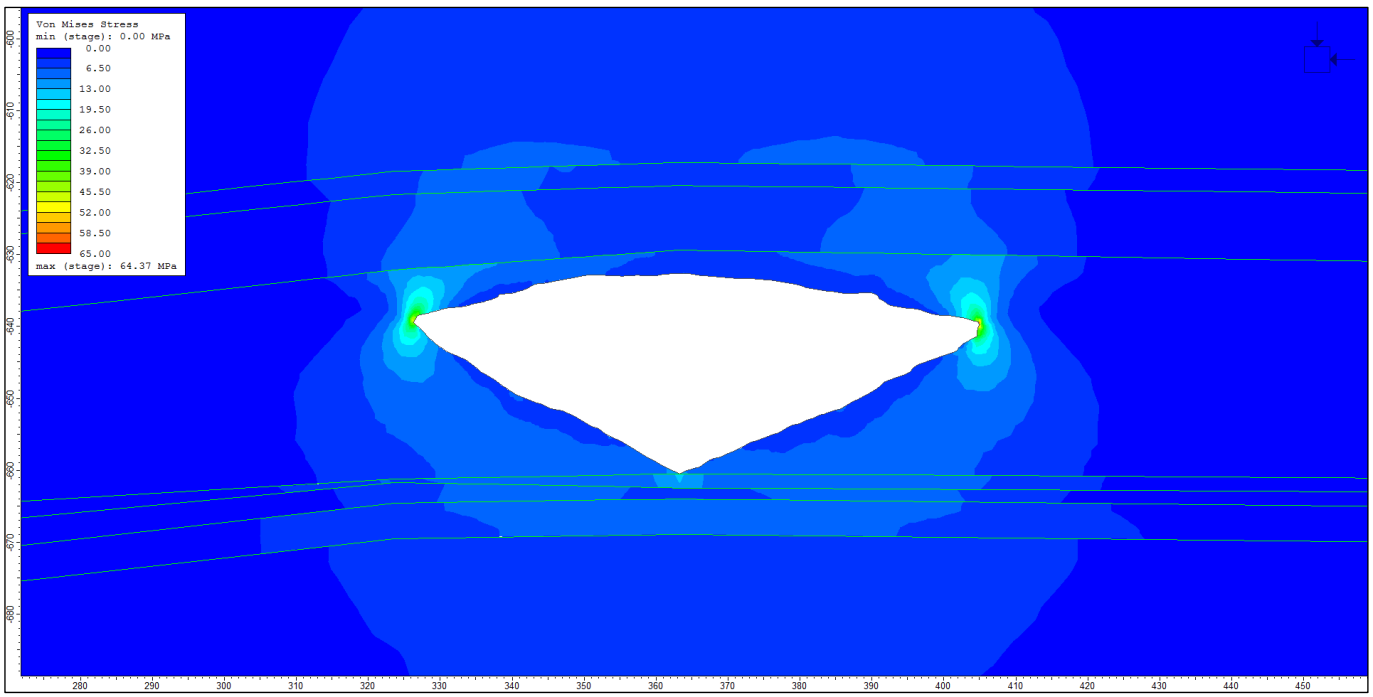

Figure D6-3: Distribution of von Mises stress [expressed in MPa] around Teesside representative cavern

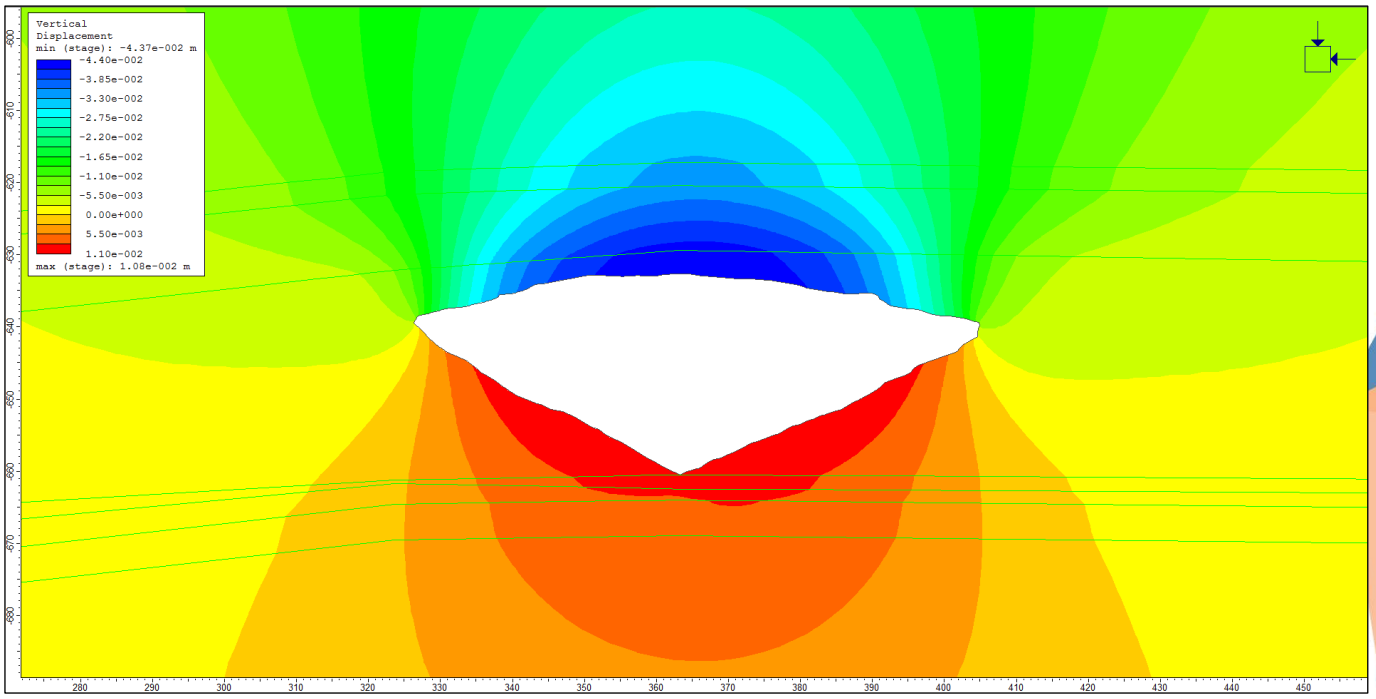

Figure D6-4: Distribution of vertical displacements [expressed in m] around Teesside representative cavern

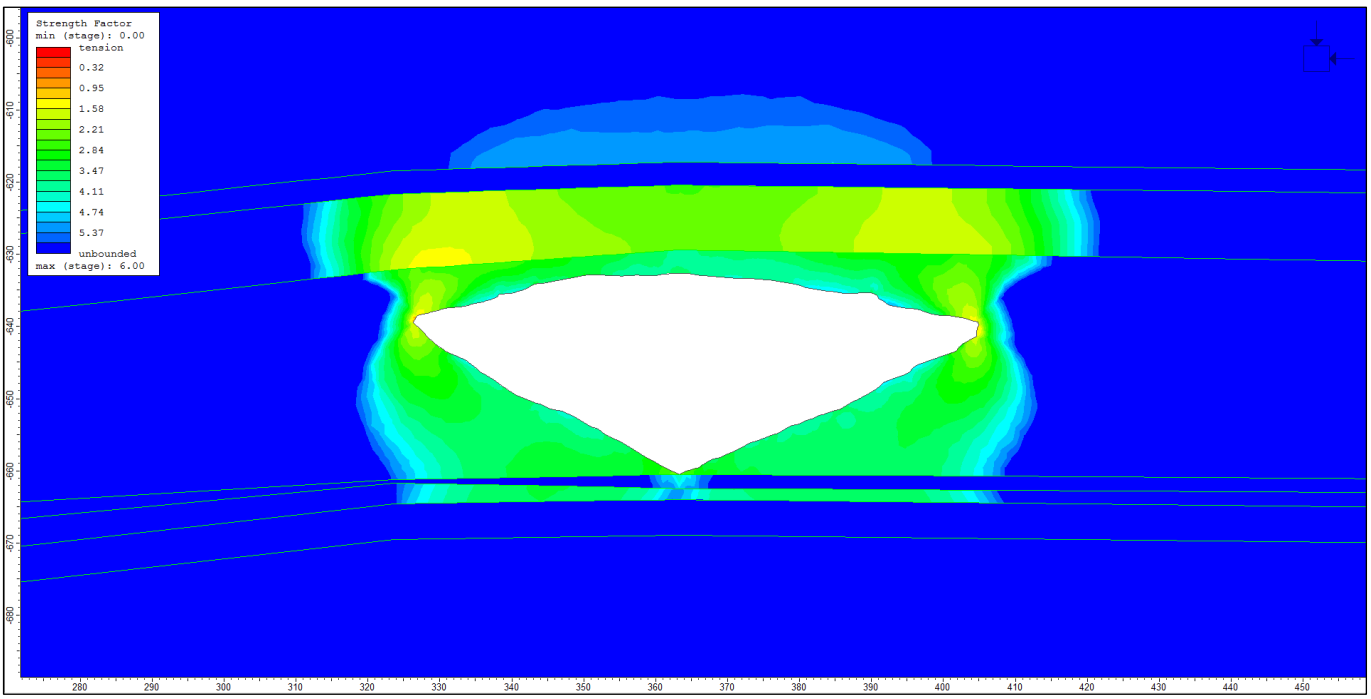

Figure D6-5: Distribution of *Strength Factor* values around Teesside representative cavern

D.7. Mathematical definition of the Drucker-Prager failure criterion

The Drucker-Prager model is used for geological materials that yield when subjected to shear loading and the corresponding shear failure envelope is expressed by the following relationship:

$$f^s = \sqrt{J_2} + \frac{q_\varphi}{3} I_1 - k_\varphi$$

Equation D5

while the tensile failure is given by the following tension yield function:

$$f^t = \frac{I_1}{3} - \sigma_t$$

Equation D6

where σ_t is the tensile strength.

Examination of Equation D5 indicates that that the yield stress depends on the two stress invariants:

- the first invariant (I_1) of the Cauchy stress tensor equal to:

$$I_1 = (\sigma_1 + \sigma_2 + \sigma_3)$$

Equation D7

- the second invariant (J_2) of the deviatoric stress tensor equal to:

$$J_2 = \frac{1}{6}\left[(\sigma_1 - \sigma_2)^2 + (\sigma_1 - \sigma_3)^2 + (\sigma_2 - \sigma_3)^2\right]$$

Equation D8

where: σ_1, σ_2 and σ_3 are the major, intermediate and minor principal stresses respectively and where q_φ and k_φ are constant material properties. The slope of the Drucker-Prager failure envelope corresponds to ⅓ of the parameter q_φ and the parameter k_φ is the intercept of the Drucker-Prager failure envelope with the $\sqrt{J_2}$ axis.

The post-failure response is modelled by using a *non-associated* flow rule which corresponds to a plastic shear potential function g^s that resembles the adopted yield function of Equation D5, but has the form:

$$g^s = \sqrt{J_2} + \frac{q_\psi}{3} I_1$$

Equation D9

Shear dilatancy is the change in volume that occurs with shear distortion of a material and is characterised by a dilation angle, ψ, which is related to the ratio of plastic volume change to plastic shear strain. The dilation parameter q_ψ for the Drucker-Prager model is determined by employing the following equation:

$$q_\psi = \frac{6}{\sqrt{3}(3 - \sin\psi)} \sin\psi$$

Equation D10

D.8. Mathematical definition of the Mohr-Coulomb failure criterion

The Mohr-Coulomb yield function defines the shear failure envelope by means of the expression:

$$f^s = \sigma_1 - \sigma_3 N_\varphi + 2c\sqrt{N_\varphi}$$ **Equation D11**

and the tensile failure by the tension yield function:

$$f^t = \sigma_t - \sigma_3$$ **Equation D12**

where φ is the peak angle of shearing resistance, c is the peak cohesion, σ_t the tensile strength and

$$N_\varphi = \frac{1+\sin\varphi}{1-\sin\varphi}$$ **Equation D13**

Note that only the major (σ_1) and minor (σ_3) principal stresses are active in the shear yield formulation presented in Equation D11; the intermediate principal stress (σ_2) has no effect.

The post-failure response is modelled by using a *non-associated* flow rule which corresponds to a plastic shear potential function g^s that resembles the adopted yield function of Equation D11, but which involves a dilatancy angle ψ instead of an of peak angle of shear resistance φ (Itasca Consulting Group, 2011a):

$$g^s = \sigma_1 - \sigma_3 N_\psi$$ **Equation D14**

where the dilation parameter N_ψ is given by

$$N_\psi = \frac{1+\sin\psi}{1-\sin\psi}$$ **Equation D15**

The angle ψ is the dilation angle which is related to the ratio of plastic volume change to plastic shear strain and which characterises the shear dilatancy of a material i.e. the change in volume that occurs with shear distortion. Slightly before and beyond peak strength, the dilatancy angle attains a constant value which is significantly smaller than the peak angle of shearing resistance.

The dilation angle ψ for geological materials is typically determined from triaxial tests, as specified by ISRM (1983), by making use of the slope of the volumetric strain versus axial strain that characterises the post-failure regime (Vermeer & de Borst, 1984).

D.9. Details of the thermodynamic analysis for East Yorkshire representative cavern

By zooming-in into the pressure ramp that precedes point A (labelled in Figure 4-3) it is possible to identify in Figure D9-1 the skipped two hrs of injection (marked with red arrows), that contributed in the reduction of the cavern pressure during its de-pressurisation.

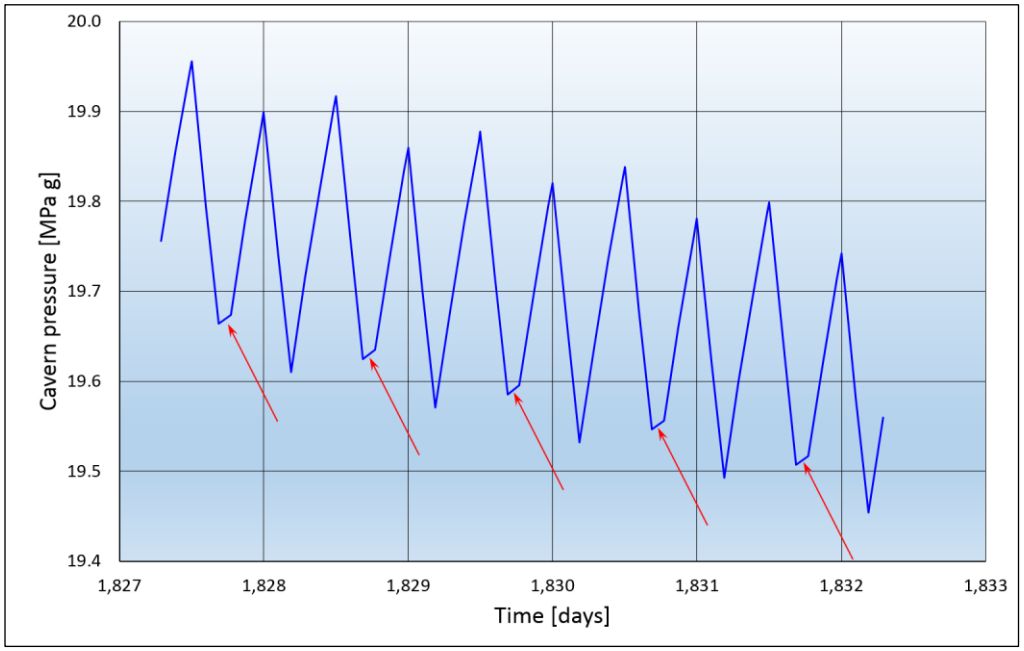

Figure D9-1: Zoom-in into the cavern pressure history of the East Yorkshire representative cavern, during its de-pressurisation phase

Similarly, by zooming-in into the cavern pressure ramp near point B (labelled in Figure 4-3) it is possible to identify in Figure D9-2 the effect of restoring the two hrs of injection which stopped the reduction of the cavern pressure. Careful examination of the peaks of the cyclic history shown in Figure D9-2, shows

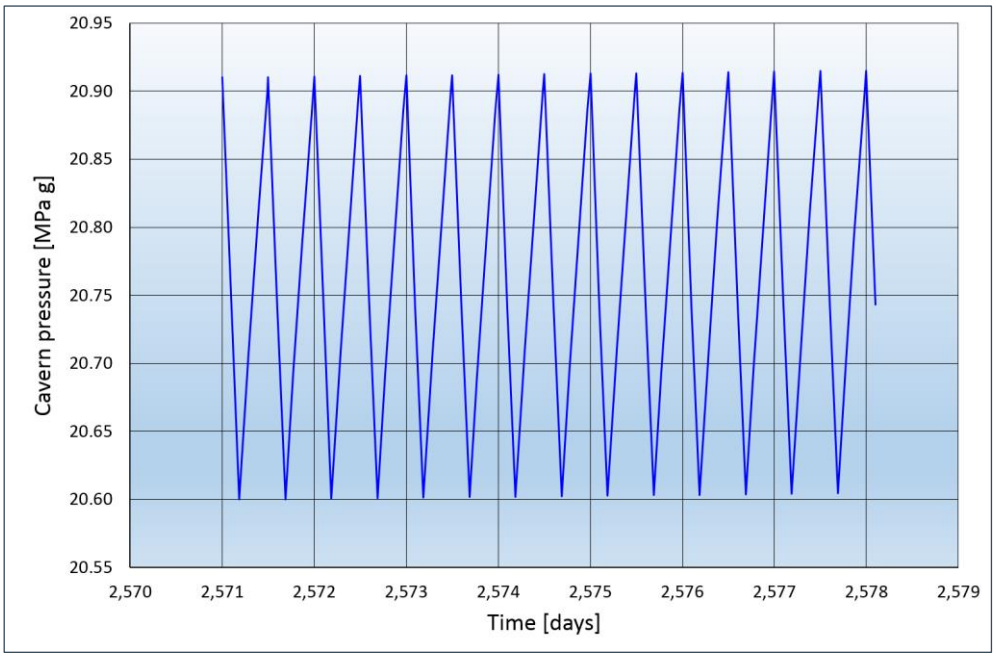

Figure D9-2: Zoom-in into the cavern pressure history of the East Yorkshire representative cavern,following its de-pressurisation phase

the gentle increase in the cavern pressure, which is related to the identified increase in the cavern temperature that was presented in Figure 4-2.

Like the pressure history, if we zoom-in into the temperature history that precedes point A (labelled in Figure 4-2), it is possible to recognise in Figure D9-3 the effect of skipping two hrs of injection (marked with green arrows) had on the development of the cavern temperature during its de-pressurisation.

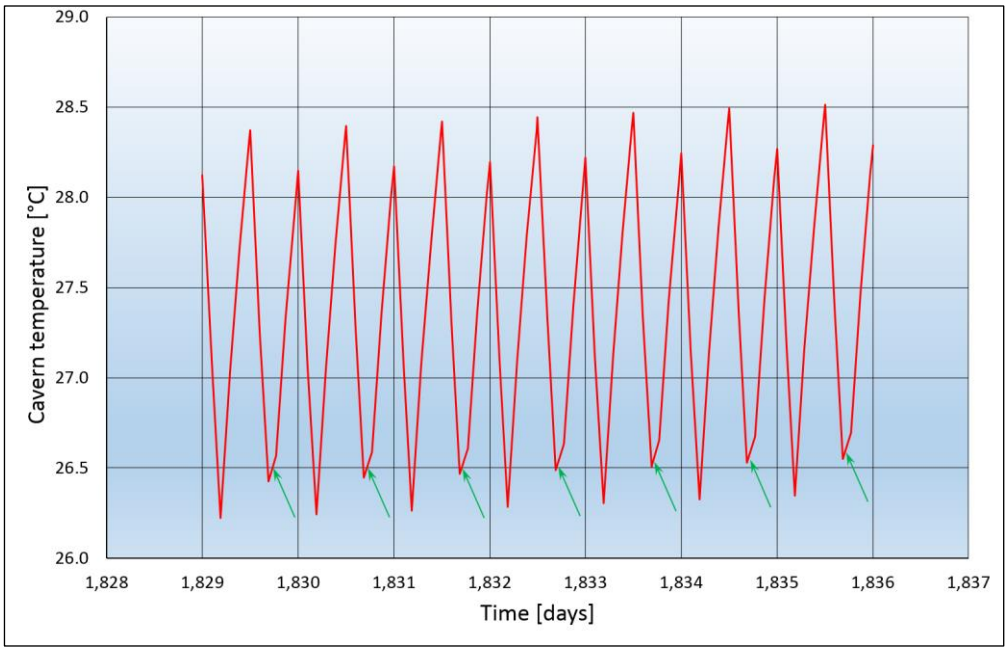

Figure D9-3: Zoom-in into the cavern temperature history of the East Yorkshire representative cavern during its de-pressurisation phase

Similarly, by zooming-in into the cavern temperature ramp, near point B (labelled in Figure 4-2), it is possible to identify in Figure D9-4 the effect of restoring the two hrs of injection, which essentially regulated the shape of the spikes that define the cyclic history of the cavern temperature. Careful examination of the peaks of the cyclic history shown in Figure D9-4, shows the very gentle increase in

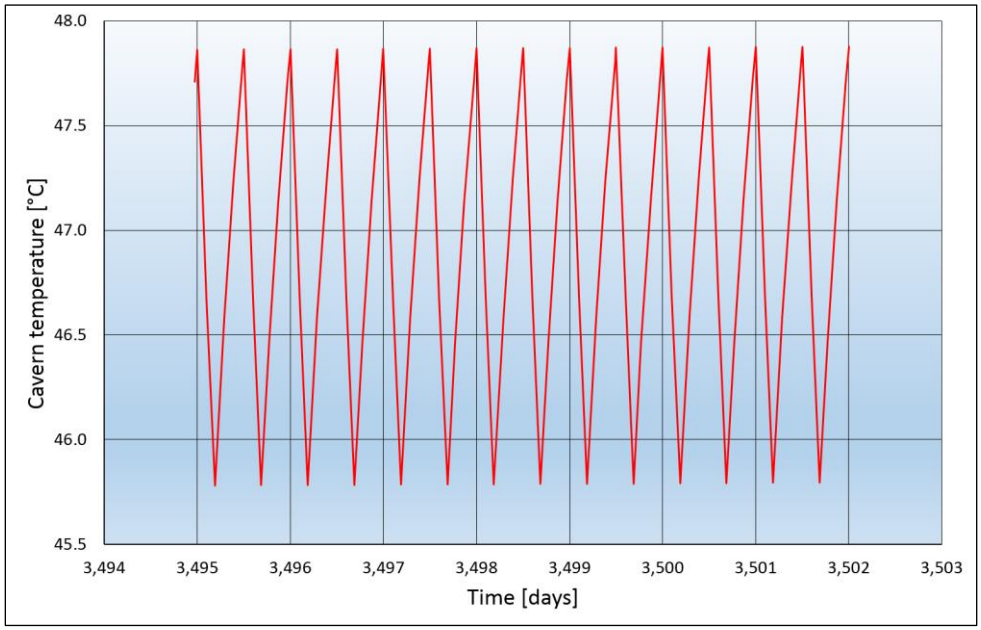

Figure D9-4: Zoom-in into the cavern temperature history of the East Yorkshire representative cavern following its de-pressurisation phase

the cavern temperature that was presented in Figure 4-2.

Furthermore, following the end of the de-pressurisation of the cavern, one can see that the temperature steps corresponding to the applied cyclic loading are of the order of 2°C.

The temperature and pressure histories that were presented respectively in Figures 4-2 and 4-3 were extrapolated to 30 years as shown in Figure D9-5 with dotted lines, by employing a second order polynomial expression. Examination of the results shown in in Figure D9-5 indicates that the specified cyclic loading over a period of 30 years results in acceptable cavern temperature and pressure conditions. In particular, the cavern temperature reaches asymptotically 53.5°C (noting that the geothermal temperature at cavern mid-height is approximately 56°C), while the cavern pressure follows a similar trend reaching asymptotically 22.4 MPa g (well below the maximum allowable pressure of 27.1 MPa g).

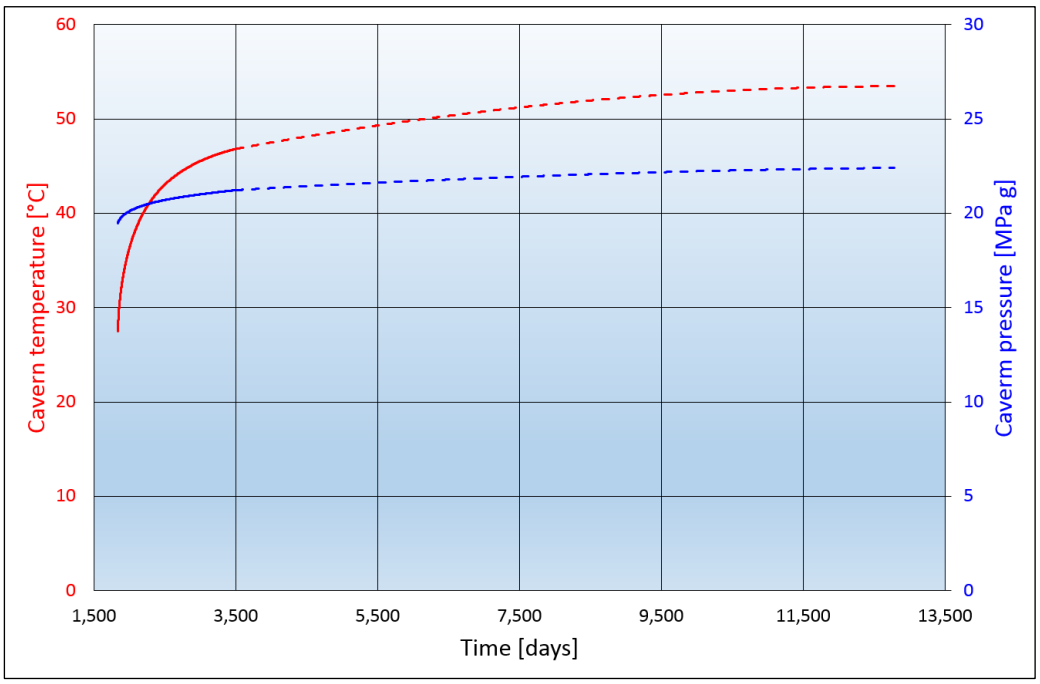

Figure D9-5: Extrapolation to 30 years of the cavern pressure and temperature histories for the East Yorkshire representative cavern

D.10. Details of the thermodynamic analysis for Cheshire representative cavern

By zooming-in into the pressure ramp that precedes point A (labelled in Figure 4-4) it is possible to identify in Figure D10-1 the skipped two hrs of injection (marked with red arrows), that contributed in the reduction of the cavern pressure during its de-pressurisation.

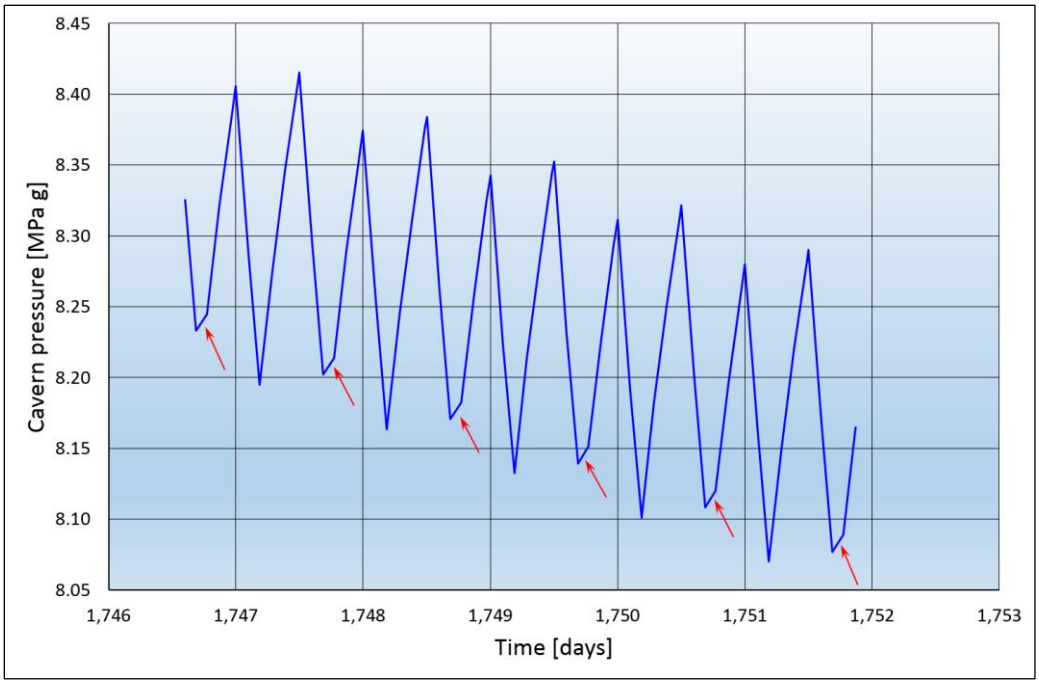

Figure D10-1: Zoom-in into the cavern pressure history of the Cheshire representative cavern, during its de-pressurisation phase

Similarly, by zooming-in into the cavern pressure ramp near point B (labelled in Figure 4-5) it is possible to identify in Figure D10-2 the effect of restoring the two hrs of injection which stopped the reduction of the cavern pressure. Careful examination of the peaks of the cyclic history shown in Figure D10-2, shows the gentle increase in the cavern pressure, which is related to the identified increase in the cavern temperature that was presented in Figure 4-4.

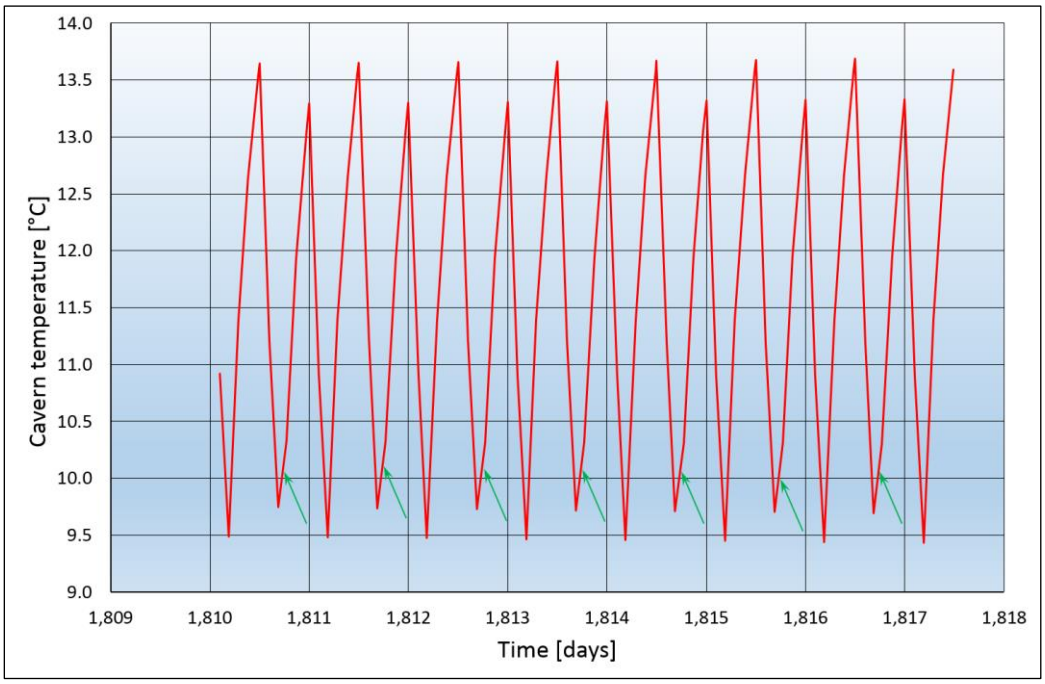

Figure D10-2: Zoom-in into the cavern pressure history of the Cheshire representative cavern, following its de-pressurisation phase

Like the pressure history, if we zoom-in into the temperature history that precedes point A (labelled in Figure 4-4), it is possible to recognise in Figure D10-3 the effect of skipping two hrs of injection (marked with green arrows) had on the development of the cavern temperature during its de-pressurisation.

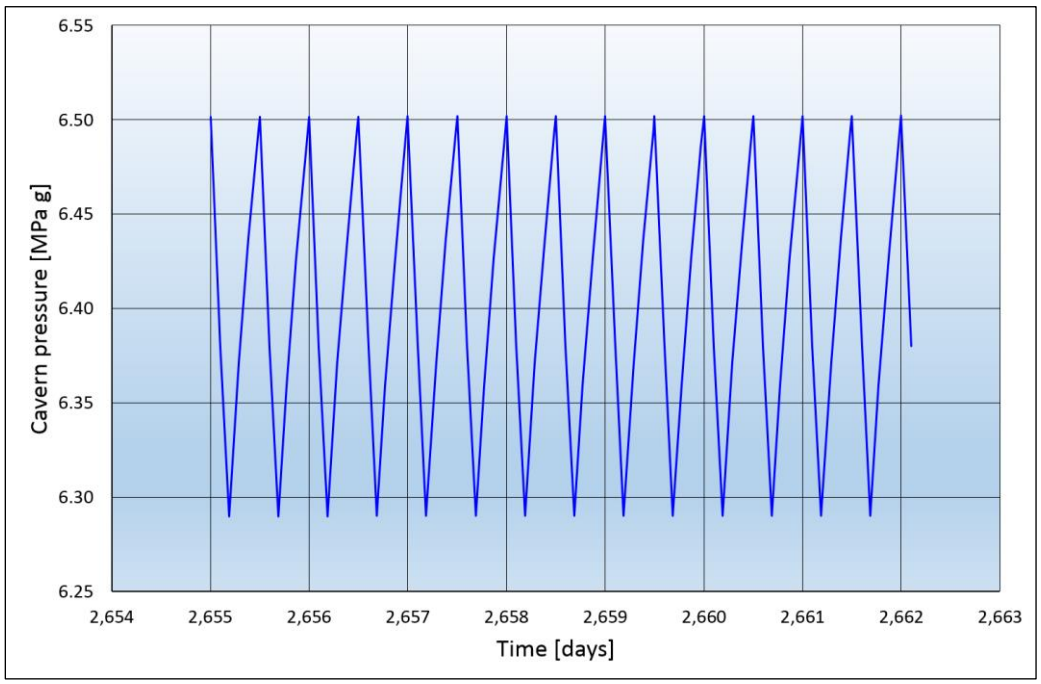

Figure D10-3: Zoom-in into the cavern temperature history of the Cheshire representative cavern during its de-pressurisation phase

Similarly, by zooming-in into the cavern temperature ramp, near point B (labelled in Figure 4-4), it is possible to identify in Figure D10-4 the effect of restoring the two hrs of injection, which essentially regulated the shape of the spikes that define the cyclic history of the cavern temperature. Careful examination of the peaks of the cyclic history shown in Figure D9-4, shows the very gentle increase in the cavern temperature that was presented in Figure 4-2.

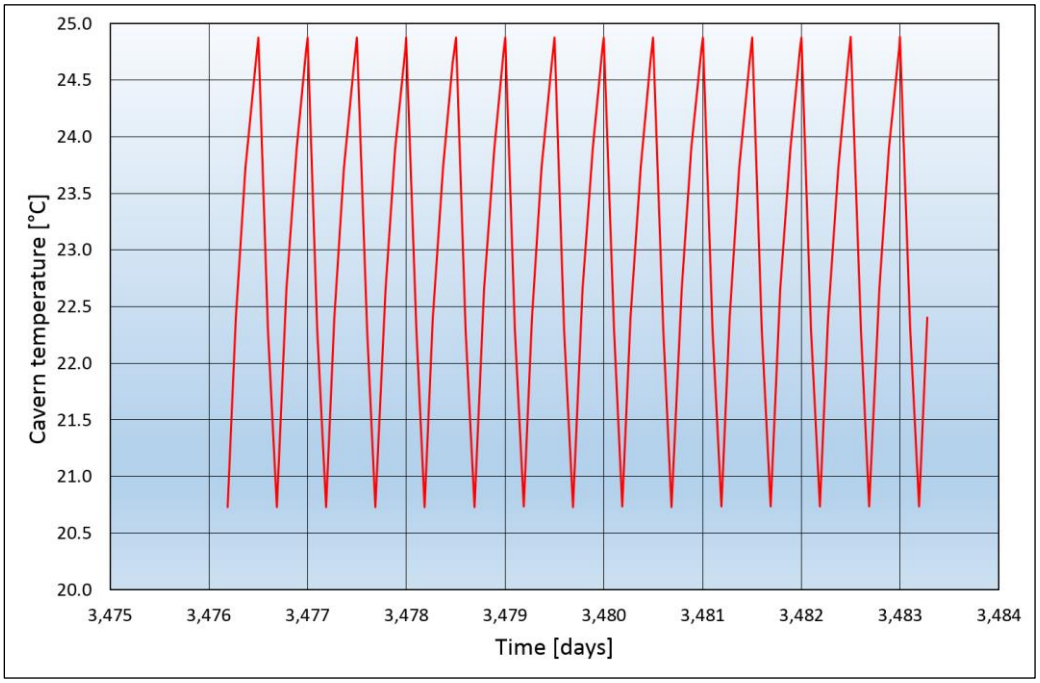

Figure D10-4: Zoom-in into the cavern temperature history of the Cheshire representative cavern following its de-pressurisation phase

Furthermore, following the end of the de-pressurisation of the cavern, one can see that the temperature steps corresponding to the applied cyclic loading are of the order of 4°C.

The temperature and pressure histories that were presented respectively in Figures 4-4 and 4-5 were extrapolated to 30 years as shown in Figure D10-5 with dotted lines, by employing a second order polynomial expression. Examination of the results shown in in Figure D10-5 indicates that the specified cyclic loading over a period of 30 years results in acceptable cavern temperature and pressure conditions. In particular, the cavern temperature reaches asymptotically 24.1°C (noting that the geothermal temperature at cavern mid-height is approximately 25.2°C), while the cavern pressure follows a similar trend reaching asymptotically 6.6 MPa g (well below the maximum allowable pressure of 9.5 MPa g)

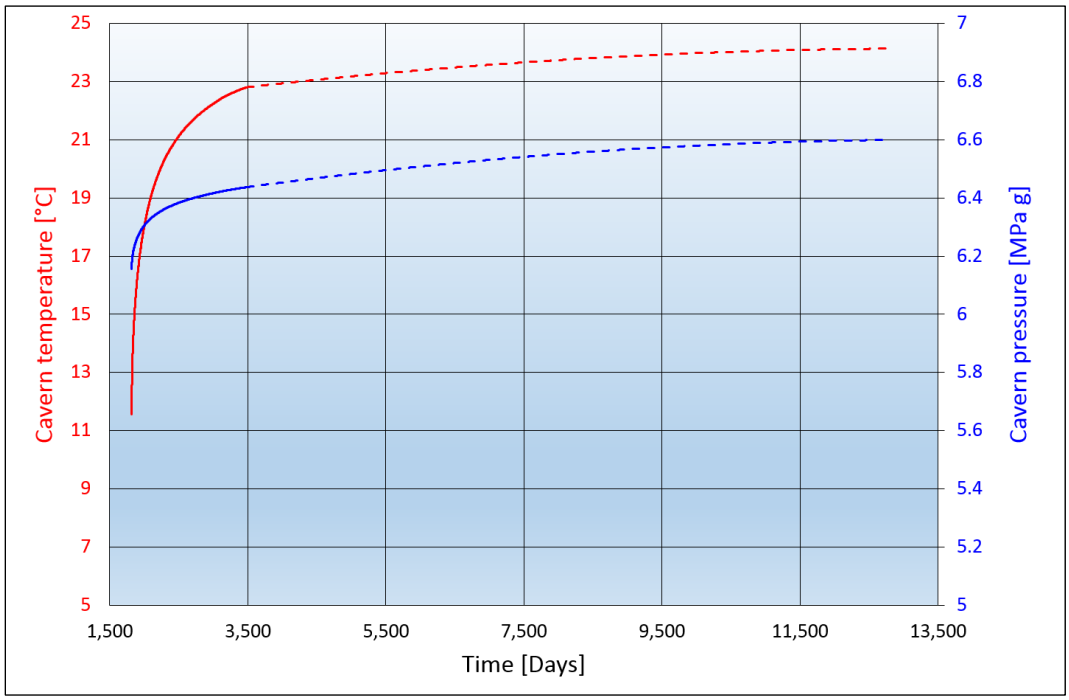

Figure D10-5: Extrapolation to 30 years of the cavern pressure and temperature histories for the Cheshire representative cavern

D.11. Geological material parameters for the East Yorkshire salt field

Table D11-1: Density, deformability and tensile strength

Material	Density [Mg/m3]	Bulk modulus [MPa]	Shear modulus [MPa]	Tensile strength [MPa]
Carnallitic Marl:	2.30	3,894	2,921	1.89
Zechstein III Boulby Halite:	2.15	10,283	8,701	1.43
Zechstein III Billingham Anhydrite:	2.93	51,321	32,282	5.88
Zechstein III Brotherton Formation:	2.42	16,571	15,130	5.28
Grauer Salzton:	2.29	18,519	12,195	1.30
Zechstein II Fordon Evaporites – Upper Halite:	2.15	16,667	10,000	1.60
Zechstein II Fordon Evaporites – Anhydrite:	2.90	33,333	15,385	8.56
Zechstein II Fordon Evaporites – Lower Halite:	2.15	16,667	10 000	1.60
Zechstein II Fordon Evaporites – Main salt:	2.56	19,279	12,127	1.60
Zechstein II Polyhalite:	2.85	27,785	14,777	4.73
Hayton Anhydrite:	2.94	50,000	23,077	8.44
Cadeby Formation:	2.62	26,149	18,802	11.0

Table D11-2: Mohr-coulomb parameters

Material	Angle of shearing resistance [°]	Cohesion [MPa]	Dilation angle [°]
Zechstein III Billingham Anhydrite	48.18	15.6	11.08
Zechstein III Brotherton Formation	44.05	13.8	9.65
Grauer Salzton	49.0	0.41	11.39
Zechstein II Fordon Evaporites - Anhydrite	45.0	5.0	9.96
Zechstein II Polyhalite	44.13	10.73	9.68
Hayton – Anhydrite	41.6	23.96	8.89
Cadeby Formation	40.0	42.0	8.41

Table D11-3: Norton power law parameters

Material	Constant C	Stress exponent n
Carnallitic Marl	1.20×10^{-10}	4.0
Zechstein III Boulby Halite	1.73×10^{-11}	4.8
Zechstein II Fordon Evaporites – Upper Halite	1.73×10^{-11}	4.8
Zechstein II Fordon Evaporites – Lower Halite	1.73×10^{-11}	4.8

Table D11-4: Main salt parameters for the PWIPP model

q_φ	0.2016,
k_φ	24.176 MPa
q_ψ	0.001
Q	14,030 cal/mol,
R	1.987 cal/(mol K),
n	2.10,
A	45 MPa-n d-1,
B	700,
$\dot{\varepsilon}^*_{ss}$	9.5 × 10-6 (m/m) d-1, and
ε_α	0.02 m/m.

D.12. Geological material parameters for the Cheshire basin

Table D12-1: Marl and salt material properties

Material property	Marl	Salt
Density[Mg/m^3]	2.498	2.174
Young's modulus [GPa]	9.287	27.048
Poisson's ratio	0.17	0.30
Tensile strength [MPa]	1.76	1.75
Cohesion [MPa]	10.0	-
Angle of shearing resistance [°]	35	-

The mean deviatoric stress associated with the beginning of dilation of the salt is about 28.7 MPa. For salt, the dilation strength should be understood as a maximum allowable stress magnitude, but cannot be interpreted as a shear failure criterion. As the confining pressure is increased, the dilating phase is less pronounced and in fact the deviatoric stress ($\sigma_1 - \sigma_3$) depends on the applied pressure (σ_3). The linear fitting of this trend leads to the following relationship:

$$(\sigma_1 - \sigma_3) = 2.4 \times \sigma_3 + 15.9 \text{ [MPa]}$$

The creep tests led to very similar results (the Vouille creep index varying between 0.42% and 0.52%). These indexes show that Cheshire salt may be classified as a relatively low creeping rock.

The following parameters describe the creep behaviour of Stublach salt according to Lemaitre's model:

α= 0.1, β= 2.208, K = 0.349 MPa (at T=300 K) and $B = Q/R$ =1,581 K.

These values lead to a Vouille creep index of 0.47%.

D.13. Geological material parameters for the Teesside salt field

Table D13-1: Density, deformability and tensile strength

Material	Density [Mg/m3]	Young's modulus [GPa]	Poisson's ratio	Tensile strength [MPa]
Boulder Clay (assumed)	1.95	0.037	0.31	0.006
Lower Liassic Shales	2.40	16.830	0.20	3.88
Penarth Shales	2.58	12.970	0.29	4.25
Mercia Mudstone	2.48	34.070	0.10	2.78
Sherwood Sandstone	2.45	14.574	0.08	2.60
Roxby Formation	2.55	14.191	0.09	2.75
Sherburn Anhydrite	2.76	33.045	0.23	3.04
Carnallitic Marl	2.30	7.100	0.20	1.89
Upper Main Salt	2.15	20.360	0.17	1.43
Honeycomb Anhydrite	2.85	56.550	0.24	4.46
Lower Main Salt	2.15	20.360	0.17	1.43
Billingham Anhydrite	2.93	80.060	0.24	5.88
Brotherton Formation	2.42	34.800	0.15	5.28

Table D13-2: Mohr-Coulomb parameters

Material	Angle of shearing resistance [°]	Cohesion [MPa]	Dilation angle [°]
Boulder Clay (assumed)	28.08	0.01	7.50
Lower Liassic Shales	33.92	15.22	6.81
Penarth Shales	33.87	14.10	6.80
Mercia Mudstone	47.77	21.83	10.93
Sherwood Sandstone	31.58	16.82	14.00
Roxby Formation	36.07	16.00	16.00
Sherburn Anhydrite	21.38	22.88	10.00
Carnallitic Marl	6.93	5.74	4.00
Upper Main Salt	38.64	8.74	6.00
Honeycomb Anhydrite	25.69	27.44	10.00
Lower Main Salt	6.93	5.74	4.00
Billingham Anhydrite	30.00	32.00	10.00
Brotherton Formation	40.00	42.00	20.00

ATKINS

Appendix E: Economic viability

E.1. OPEX design life profile and annual service, fixed and variable costs

There are many influencing factors regarding the recommended inspection intervals advised by the OEMs. A fixed ratio of starts to operating hours is commonly adopted, but some OEMs, such as GE, recognise these as separate criteria as shown in Table E-1. Cyclic application of GTs as needed for this project will result in thermal mechanical fatigue, which will be the plant life limiting factor.

Table E-1: Typical GE baseline inspection intervals

Hot gas path inspection	24,000 hrs or 1,200 starts
Major Inspection	48,000 hrs or 2,400 starts

Generally, the inspection intervals are driven by operating hours and number of starts, which are in turn based on the following service factors (Jamieson Janawitz (GE power), 2015):

Hours-Based Factors

- Fuel type.
- Peak load operation.
- Diluent (N_2, water or steam injection).

Starts-Based Factors

- Start type (conventional or peak demand matching).
- Start load (max. load achieved during start cycle, e.g. part, base, or peak load).
- Normal shutdown.
- Emergency trips.

An example OPEX profile for the design life of the plant is given in Appendix E. In this example the inspection intervals are planned throughout the expected GT lifetime. The inspections considered are as follows:

A. **Minor inspection:** Assumed to be mainly visual inspections of the accessible gas path, including the compressor, turbine inlet, the combustion chamber and the exhaust.
Duration 3 days, approx. £192,500

B. **Hot Gas Path inspection:** The GT is opened for the hot gas path inspection. Based on the findings parts may be replaced or refurbished. Non-destructive testing (NDT) may also be performed.
Duration up to 12days, approx. £269,500

C. **Major Overhaul:** The compressor / GT casings are removed and all vanes, blades and nozzles are inspected. In particular, the status of coatings is noted and components are replaced if found to be damaged or suffering from thermal mechanical stresses. NDT is deployed alongside detailed visual inspections. The rotor is removed.
Duration up to 6 weeks. Approx. £8,354,500

The indicative OPEX costs over the design life of the GT plant considered for this report are presented in Table E1-1 below. The slow ramp up in costs is due to no gasifier outages in the first three years, and staggered unit commissioning. The mid life peak is due to major overhaul costs included half way through the design life.

Table E1-1: OPEX design life indicative costing and plant availability assumptions

PROJECT ETI 1026MWe + 2 x (2+1) E class machines, service, fixed/ variable costs

	days
A	3
B	12
C	42

							5years					10years					15years					20years					25years					30years
Year		2030	2031	2032	2033	2034	2035	2036	2037	2038	2039	2040	2041	2042	2043	2044	2045	2046	2047	2048	2049	2050	2051	2052	2053	2054	2055	2056	2057	2058	2059	2060
Unit 1		comissioning phase	A	B	C	A	B	C	A	B	C	A	B	C	A	B	C	A	B	C	A	B	C	A	B	C	A	B	C	A	B	C
Unit 2			A	B	C	A	B	C	A	B	C	A	B	C	A	B	C	A	B	C	A	B	C	A	B	C	A	B	C	A	B	C
Unit 3				A	B	C	A	B	C	A	B	C	A	B	C	A	B	C	A	B	C	A	B	C	A	B	C	A	B	C	A	B
Unit 4					A	B	C	A	B	C	A	B	C	A	B	C	A	B	C	A	B	C	A	B	C	A	B	C	A	B	C	A	A
EOH-equiv operating hours	(Scenario 3 = 9hrs/day)	0	3231	3042	2394	2745	2664	2394	2745	2664	2394	2745	2664	2394	2745	2664	2394	2745	2664	2394	2745	2664	2394	2745	2664	2394	2745	2664	2394	2745	2664	2394
starts, can equate to EOH			698	670	526	604	586	526	604	586	526	604	586	526	604	586	526	604	586	526	604	586	526	604	586	526	604	586	526	604	586	526
cumulative starts			698	1368	1894	2498	3084	3610	4214	4800	5326	5930	6516	7042	7646	8232	8758	9362	9948	10474	11078	11664	12190	12794	13380	13906	14510	15096	15622	16226	16812	17338
estimate annual GWh generation	GWh (@ plant = 0.96GW)		2792	2628	2068	2372	2302	2068	2372	2302	2068	2372	2302	2068	2372	2302	2068	2372	2302	2068	2372	2302	2068	2372	2302	2068	2372	2302	2068	2372	2302	2068
GT Outage (across 4 units based on inspections)	days		6	27	99	60	69	99	60	69	99	60	69	99	60	69	99	60	69	99	60	69	99	60	69	99	60	69	99	60	69	99
Gasifier Outage 3wks/yr/gasifier	assume 3x gasifiers		0	0	0	42	21	21	42	21	21	42	21	21	42	21	21	42	21	21	42	21	21	42	21	21	42	21	21	42	21	21
Plant Planned Outage rate	days		6	27	99	102	90	120	102	90	120	102	90	120	102	90	120	102	90	120	102	90	120	102	90	120	102	90	120	102	90	120
Plant Planned Outage Rate , percent of year	POR%		2%	7%	27%	28%	25%	33%	28%	25%	33%	28%	25%	33%	28%	25%	33%	28%	25%	33%	28%	25%	33%	28%	25%	33%	28%	25%	33%	28%	25%	33%
Forced outage rate	FOR%		10	3	3	3	3	3	3	3	3	3	3	3	3	3	3	3	3	3	3	3	3	3	3	3	3	3	3	3	3	3
Availabilty (planned + forced)	AV%	59.20	88.4	89.6	69.9	69.1	72.3	64.1	69.1	72.3	64.1	69.1	72.3	64.1	69.1	72.3	64.1	69.1	72.3	64.1	69.1	72.3	64.1	69.1	72.3	64.1	69.1	72.3	64.1	69.1	72.3	64.1
Shakedown - due to initial defects, adjustments etc		59.20																														
Overhaul Maintenance																																
Unit 1	$M Dollar		0.25	0.35	10.85	0.25	0.35	10.85	0.25	0.35	10.85	0.25	0.35	10.85	0.25	0.35	10.85	0.25	0.35	10.85	0.25	0.35	10.85	0.25	0.35	10.85	0.25	0.35	10.85	0.25	0.35	10.85
Unit 2	$M Dollar		0.25	0.35	10.85	0.25	0.35	10.85	0.25	0.35	10.85	0.25	0.35	10.85	0.25	0.35	10.85	0.25	0.35	10.85	0.25	0.35	10.85	0.25	0.35	10.85	0.25	0.35	10.85	0.25	0.35	10.85
Unit 3	$M Dollar		0	0.25	0.35	10.85	0.25	0.35	10.85	0.25	0.35	10.85	0.25	0.35	10.85	0.25	0.35	10.85	0.25	0.35	10.85	0.25	0.35	10.85	0.25	0.35	10.85	0.25	0.35	10.85	0.25	0.35
Unit 4	$M Dollar		0	0	0.25	0.35	10.85	0.25	0.35	10.85	0.25	0.35	10.85	0.25	0.35	10.85	0.25	0.35	10.85	0.25	0.35	10.85	0.25	0.35	10.85	0.25	0.35	10.85	0.25	0.35	10.85	0.25
Fixed costs (1. Other Fixed Contracts, 2. Preventative maintenance costs, 3. Salaries, 4. Insurance, 5. Grid Connection Charge, 6. Rates)		7	14	14	14	14	14	14	14	14	14	14	14	14	14	14	14	14	14	14	14	14	14	14	14	14	14	14	14	14	14	14
Annual Fee	$M Dollar		0.66	0.66	0.66	0.66	0.66	0.66	0.66	0.66	0.66	0.66	0.66	0.66	0.66	0.66	0.66	0.66	0.66	0.66	0.66	0.66	0.66	0.66	0.66	0.66	0.66	0.66	0.66	0.66	0.66	0.66
Mobilisation Fee		0.35																														
Mid Life	$M Dollar														25	25	25	25														
TOTAL	**$M Dollar**	**7.4**	**15.2**	**15.6**	**37.0**	**26.4**	**26.5**	**37.0**	**26.4**	**26.5**	**37.0**	**26.4**	**26.5**	**37.0**	**51.4**	**51.5**	**62.0**	**51.4**	**26.5**	**37.0**	**26.4**	**26.5**	**37.0**	**26.4**	**26.5**	**37.0**	**26.4**	**26.5**	**37.0**	**26.4**	**26.5**	**37.0**
	£M Pounds	**5.7**	**11.7**	**12.0**	**28.5**	**20.3**	**20.4**	**28.5**	**20.3**	**20.4**	**28.5**	**20.3**	**20.4**	**28.5**	**39.5**	**39.6**	**47.7**	**39.5**	**20.4**	**28.5**	**20.3**	**20.4**	**28.5**	**20.3**	**20.4**	**28.5**	**20.3**	**20.4**	**28.5**	**20.3**	**20.4**	**28.5**

EVENT	PAYMENT	
	$	£
Mobilsation Fee	*$350,000*	£269,500
Annual Fee - LTSA	*$660,000*	£508,200
A Inspection - Minor		
Duration 3 days		
Fee	*$250,000*	£192,500
B Inspection - Hot gas path		
Duration 12 days		
Fee	*$350,000*	£269,500
C Inspection - Major		
Duration (up to) 6weeks		
duratino 5 weeks	*$10,300,000*	£7,931,000
duration 6 weeks	*$11,400,000*	£8,778,000
inspection C average	*$10,850,000*	£8,354,500

Assumptions:

1. costs presented are indicative only,
2. equivelant operating hours based on hours generating annually from scenario 3
3. assumed no gasifer outage in first 3 years, but required thereafter due to H2 production source being stream 1.
4. force outage rate assumed at 3 days per year, but 10 days in the 1st year of operation to reflect plant shakedown (initial defects etc.)
5. Gasifer maintenance costs have been included,
6. A mid life major overall cost of £25m has been included per unit, includes cost of rotor assumed at approx $15m
7. Assume 30 year design life
8. assume hot gas path inspection required after 1200 starts per unit and major overaul after 2400 starts per unit
9. 65 personnel at site and an average salary of £30k and on cost of a further 50% salaries are £3million per annum
10. costs based on 2010 cost rates for E class machine OCGT
11. fixed costs assumed, contracts @ $3m pa, preventative maintenance $2m pa, salaries $3m pa, insurance $1.5m pa, grid connection $2m pa, rates $2.5 pa
12. variable costs excluded, except for costs of inspections dependant on operational hours
13. 0.77 £ to $ rate used, may 2017

30year OPEX cost **$ 983.1**
£ 757.0

ATKINS

Appendix F:
Low Carbon Case

F.1. Surface plant design considerations

F.1.1. Final power plant configuration (2030 future capability)

To present a credible future scenario case historic performance data was reviewed and the improvements that have been seen in efficiency and power output have been plotted since 1990. This data was largely obtained through the GT PRO database, but also supported from case studies and past project experience.

Figure F1-1 and figure F1-2 show historical performance of small frame and "E" class GTs. The trends were extrapolated to 2030 to predict an average performance improvement of about 1.5% in efficiency and 10-15% in power output by 2030.

Table F1-1: Future performance improvements by 2030 (indicative only)

Model	Combined cycle power generation		
	Configuration	GT net power output	Gross efficiency
"E" class	CCGT 2 + 1	~600 MW	~55%
"F" class	CCGT 2 + 1	~1,000 MW	~60%
"H" class	CCGT 2 + 1	~1,400 MW	~63%
SGT-800	CCGT 6 + 1	~500 MW	~58%

Table F1-1 indicates that a new build high H_2 CCGT plant in 2030 could be expected to achieve efficiencies of the order of ~58-63%, provided significant technology advancement and financial investment is applied.

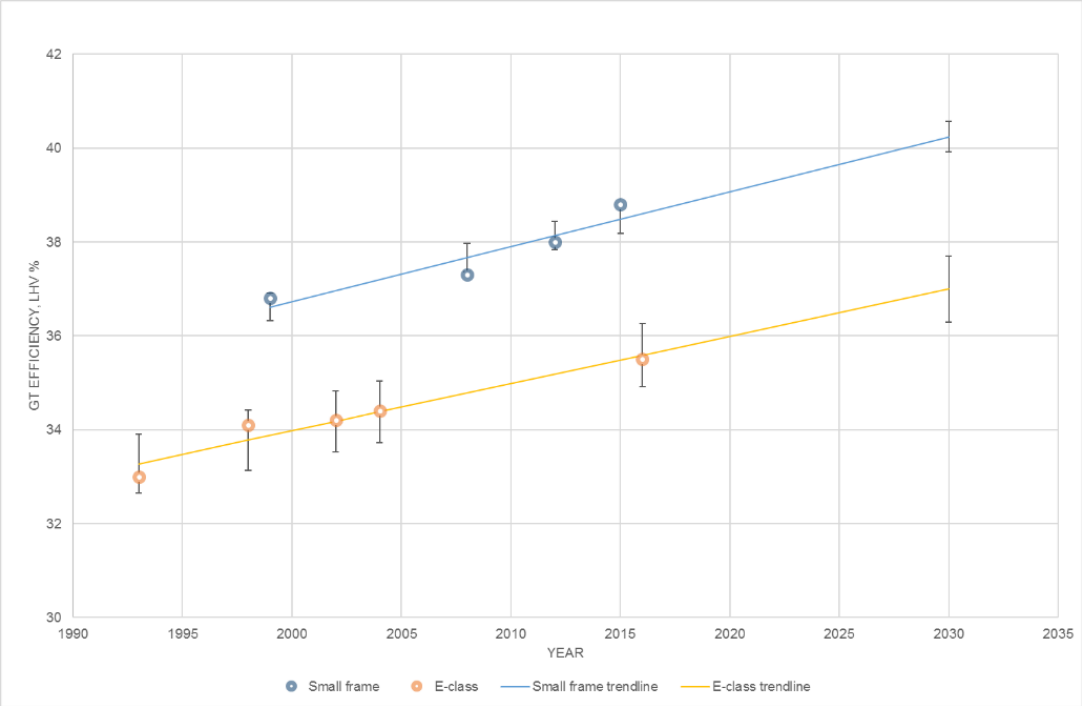

Figure F1-1: Net efficiency trendlines for small frame and "E" class GTs*

*The results presented in Figure F-1 and Figure F-2 have a significant uncertainty associated with this method of performance prediction, which depends on a number of variables, such as future commercial drivers for GT development, theoretical maximum performance due to material development etc..
** A tolerance band has been given to each data point, where several GT models may exist across manufactures for the same GT class.

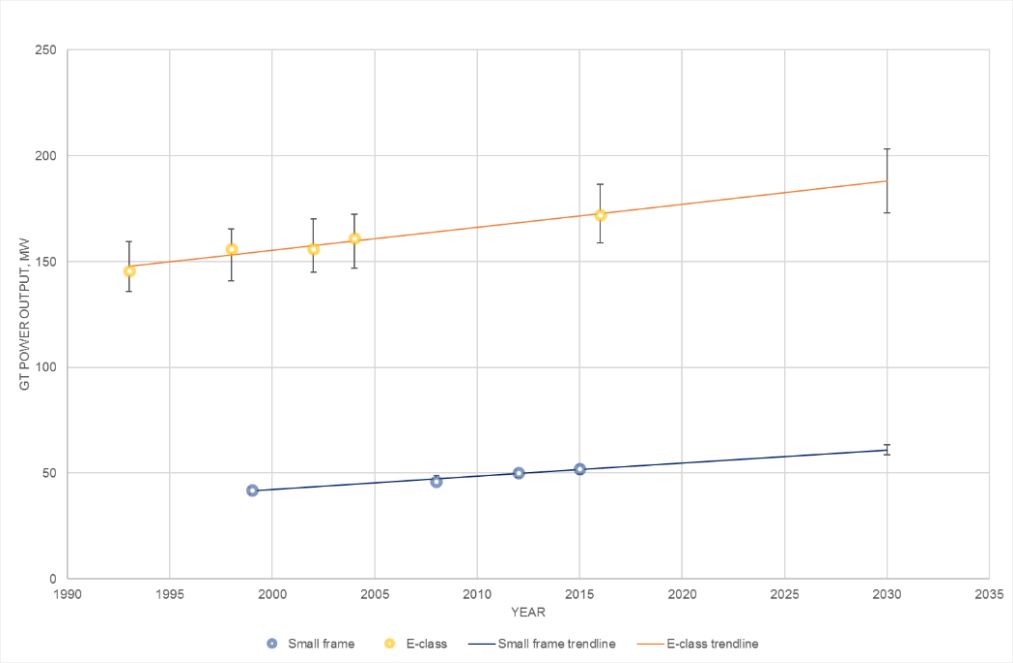

Figure F1-2: Power output trendlines for small frame and "E" class GTs

F.1.2. Fuel requirement for low carbon, 2030 case per cavern

To investigate the unconstrained cavern demand a low carbon case was reviewed, where no natural gas is assumed to be needed (or where NG may be used to supplement the 1GWe generation). In this case, the cavern would support approx. 60% (based on 10 hours generation) of the instantaneous gas requirement to the GT. The remaining ~40% would be provided directly from the gasifier as discussed previously.

To determine the final fuel requirement from the cavern for multiple modelling cases the following methodology was undertaken:

- A base fuel requirement case is modelled from GT PRO for 2x SGT-2000E machines. This assumes a gross GT efficiency of 35.4% (which is an average across the GTs modelled under fuel mixes 1 to 5, (see table 2-10) and includes a 1.5% uplift as discussed in F.1.1).
- The power output assumed is approx. 2/3 of total 1GWe (with remaining ~1/3 provided from the steam turbine).
- Based on the fuel properties for fuel gas stream 1 (see Appendix A, Table A1-1) the total fuel mass flow rate was calculated and split between the gasifier output and the required cavern output.
- An initial two cavern model was assumed and potential cavern injection and extraction flowrates are calculated. For the following models, the resultant fuel gas flowrates were based on a 2 well per cavern basis.

The operational flowrate limits of the daily cycles were as detailed in Table F1-2 for a 2, 3 and 5 cavern basis.

Table F1-2: Daily cycle operational limits

No. of caverns	No. of wells	Mass extraction period (10hours) per cavern (kg)	Equivalent volume extraction per cavern (Nm^3)
2	4	487,201	1,969,284.08
3	6	324,801	1,312,856.05
5	10	194,880	787,713.63
Density at normal conditions, 0°C 1 atm		0.2474	kg/Nm3

The minimum number of caverns required was determined based on the achievable extraction from one well (with a typical ID of 8.835'') and maximum was based on the number of caverns needed to achieve stable cavern thermo-mechanical modelling results. The estimated max gas flows are given in table F1-3 below based on densities (at constant temperature of 23.9°C) from the HYSYS software:

Table F1-3: Maximum volume flowrates based on densities

(indicative) Cavern pressure at LCCS (barg)	Cheshire, (stream 1) max 1x well flowrate at 30m/s, kg/hr	Cavern gas density (kg/m^3) From HYSYS	Maximum volume flowrate Nm^3/hr
95	89,528	20.96	361,875
75	71,383	16.71	288,531
55	52,951	12.40	214,029
35	34,250	8.02	138,440
30	29,535	6.91	119,383

ATKINS

Appendix G:

Cheshire Case Study,

Cavern Cyclic loading impact

G.1. Stress the Cheshire representative cavern to theoretical limits.

G.1.1. Bench-marking of the employed thermodynamic modelling software for hydrogen application

As mentioned in Chapter 4, the thermodynamic computations of the hydrogen storage salt caverns were carried out employing the SCTS software package (Nieland, 2004) and the derived results were adjusted by employing a bench-marking process using the TDFD program which was developed in the University of Newcastle (Thompson, 1973) to allow the modelling of H_2 storage.

However, taking into consideration the intense cyclic nature of the H_2 storage operations that need to be investigated, it was decided to bench-mark the capabilities of the SCTS program with the recent modelling of H_2 storage caverns that was carried out by Storengy (Louvet et al, 2017). The results of the comparative study between H_2 storage and traditional natural gas storage that was undertaken by Storengy to investigate the main differences between these two storage operations, are shown in G1-1 (for the cavern pressure) and in G1-2 (for the cavern temperature).

The Storengy modelling was carried out for a cavern with a volume of 570,000 m^3, that was operated between *pmax* = 240 bara and and *pmin* = 60 bara, with a LCCS located a depth of 1,300 m and a ground temperature at cavern depth of 53°C.

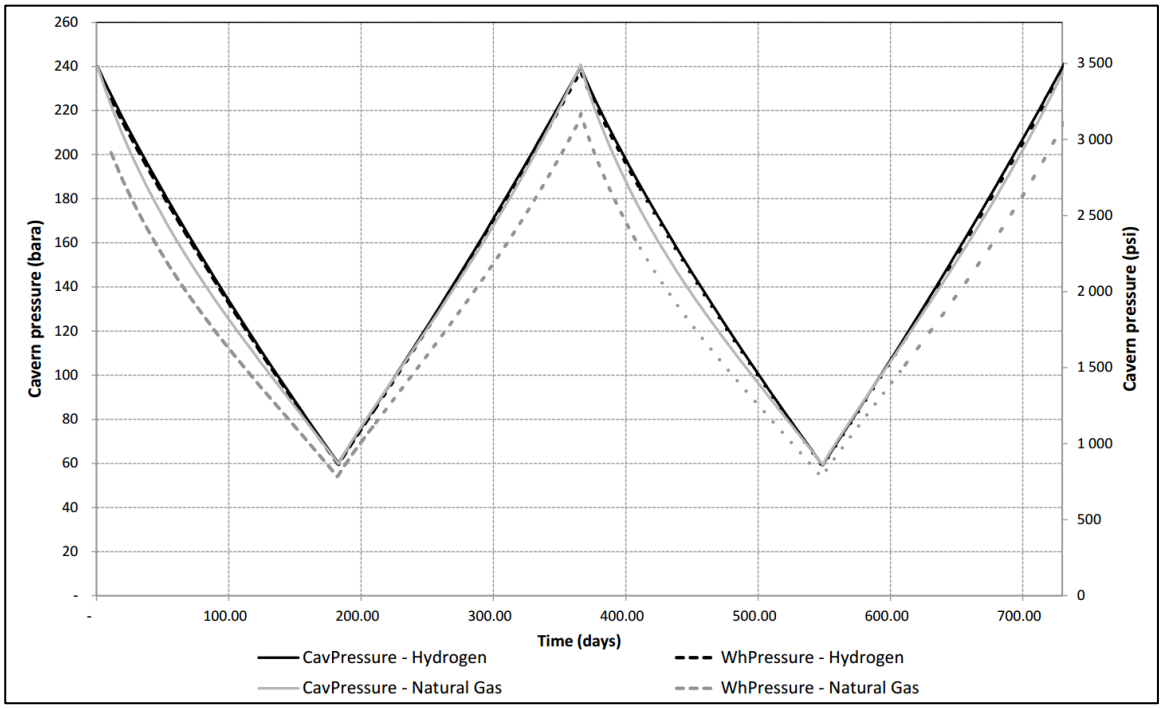

Figure G1-1: Comparison of cavern and well-head pressures for natural gas and hydrogen Storengy results (Louvet et al, 2017)

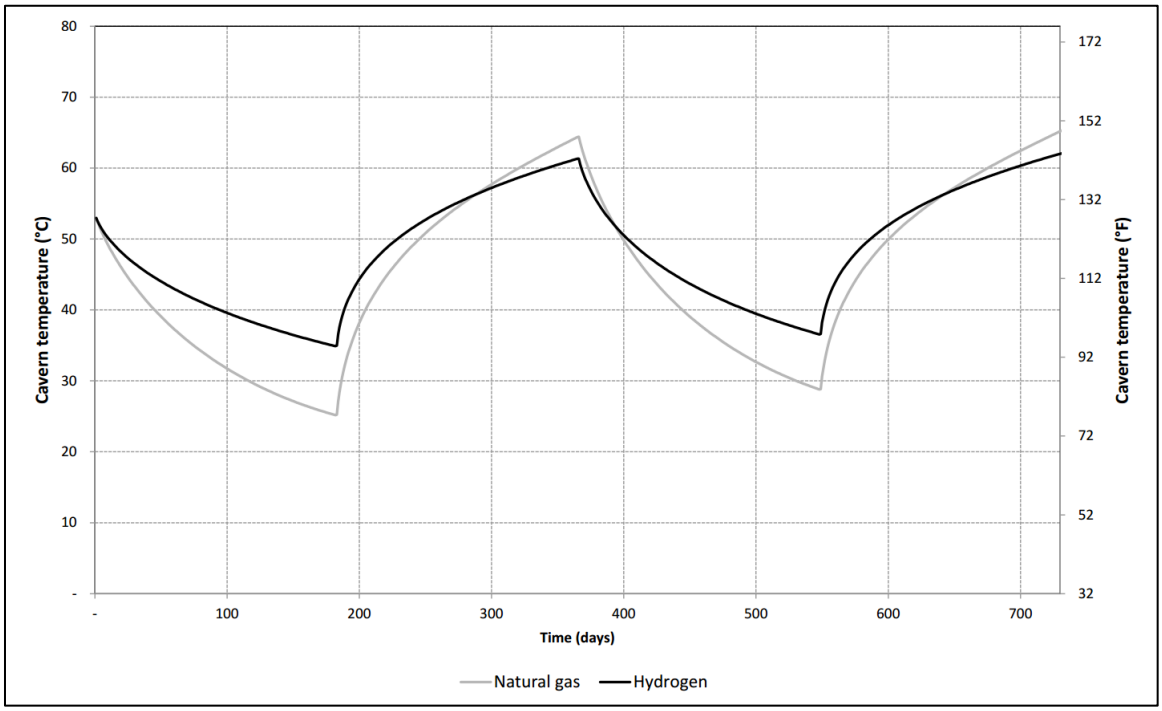

Figure G1-2: Comparison of cavern temperature for natural gas and hydrogen, Storengy results (Louvet et al, 2017)

The SCTS modelling was carried out for the Cheshire representative cavern which has a volume of 304,400 m^3, that is operated between *pmax* = 95 barg and and *pmin* = 30 barg, with a LCCS located a depth of 535 m and a ground temperature at cavern depth of 25.2°C.

Moreover, the composition of H_2 and natural gas mixtures used in the SCTS modelling are different from Storengy's data. Storengy is using pure H_2 (SCTS modelling employs 90%) and 91.4% CH_4 (SCTS modelling employs 86%). As a result, the ratio "natural gas/H_2" of the flow rates used in the modelling by Storengy is 1.327 while in the SCTS modelling it corresponds to 1.463.

Despite the identified differences between the two modelling approaches, the respective pressure and temperature graphs exhibit identical trends. Comparison of the graphs for the natural gas and H_2 shown in Figure G1-1 and Figure G1-2, with the corresponding graphs shown Figure G1-3 and Figure G1-4 that were derived using the SCTS program, confirms the ability of the SCTS to model successfully the underground H_2 storage in salt caverns.

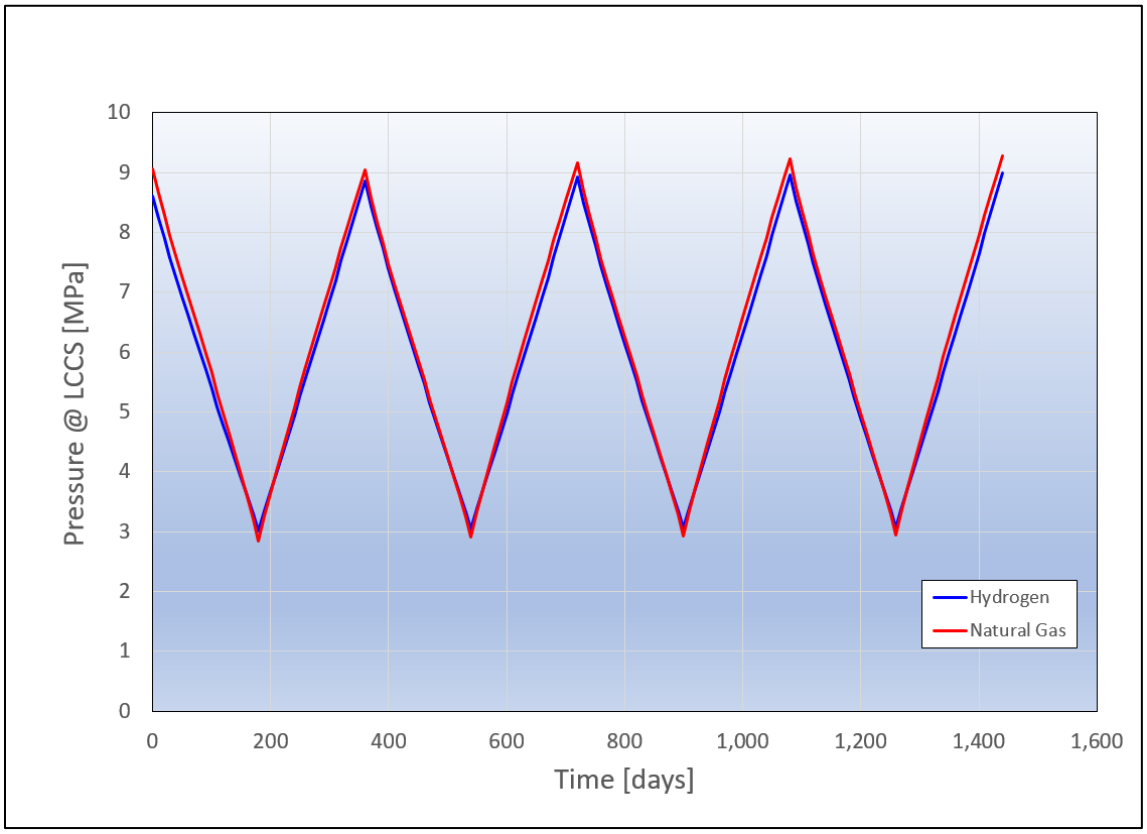

Figure G1-3: SCTS Comparison of cavern and well-head pressures for natural gas and hydrogen

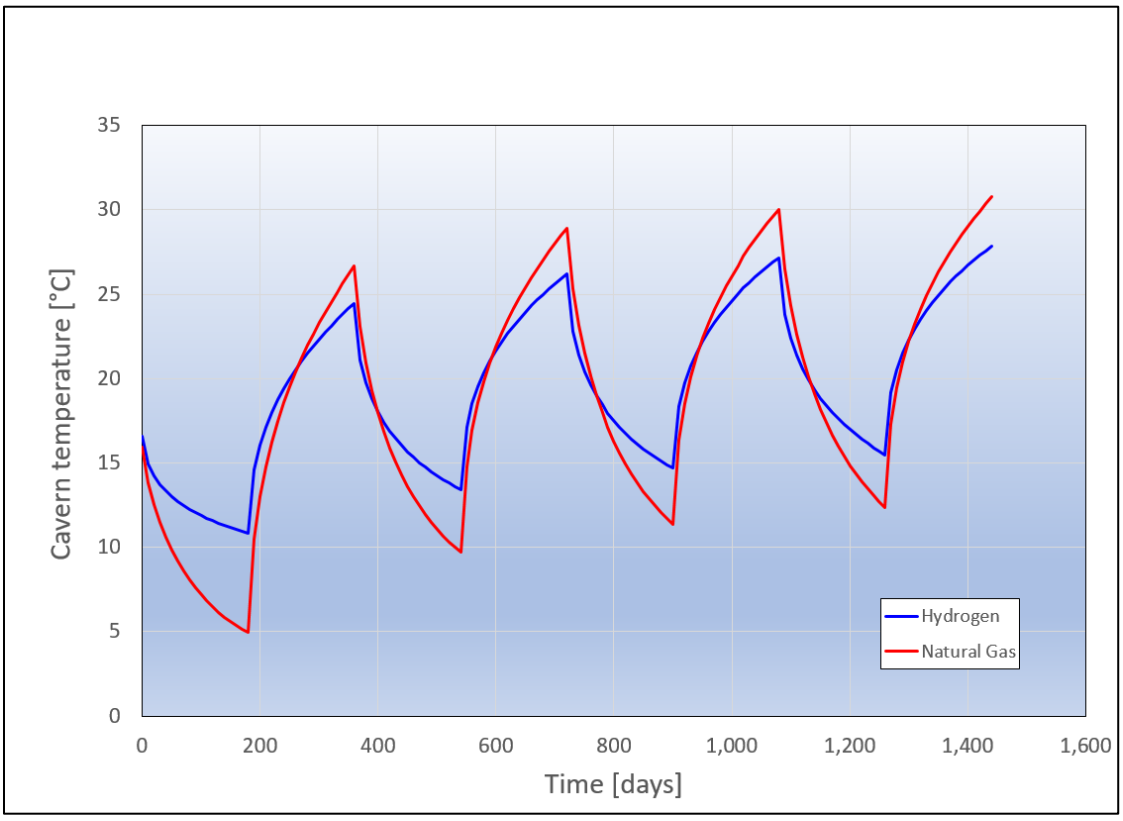

Figure G1-4: SCTS Comparison of cavern temperature for natural gas and hydrogen

G.2. Analysis for seasonal plus diurnal loading cycles

G.2.1. Run 1, 2 cavern basis:

In Run 1, two caverns were used and the employed H_2 flowrates are shown in Table G2-1,

Table G2-1: Flow rates used for Run 1 incorporating two caverns

	Volume flowrates per cavern			
	0.208 day	0.292 day	0.208 day	0.292 day
	Cycle 1 Part1	Cycle 1 Part2	Cycle 2 Part1	Cycle 2 Part2
Day	$Nm^3/5hr$	$Nm^3/7hr$	$Nm^3/5hr$	$Nm^3/7hr$
1	-984642	809803	-984642	809803
2	-984642	459180	-984642	459180
3	-984642	984642	-984642	984642
4	-984642	984642	-984642	984642
5	-492321	674209	-492321	674209
6	-984642	984642	-984642	984642
7	-984642	984642	-984642	984642
8	-984642	984642	-984642	984642
9	-984642	984642	-984642	984642
10	-984642	984642	-984642	984642
11	-492321	895625	-492321	895625
12	-492321	908173	-492321	908173
13	-492321	612880	-492321	612880
14	-492321	492321	-492321	492321
15	-492321	893621	-492321	893621
16	-984642	717400	-984642	717400
17	-492321	893038	-492321	893038
18	-984642	984642	-984642	984642
19	-492321	625698	-492321	625698
20	…….	……	…….	…….
…	…….	……	…….	…….

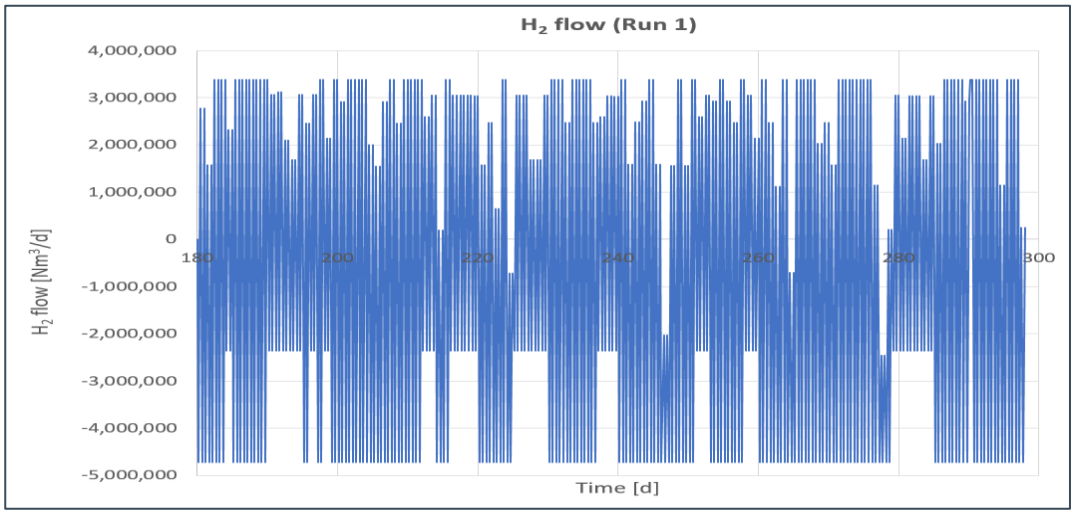

Figure G2-1: Run 1, flowrates profile

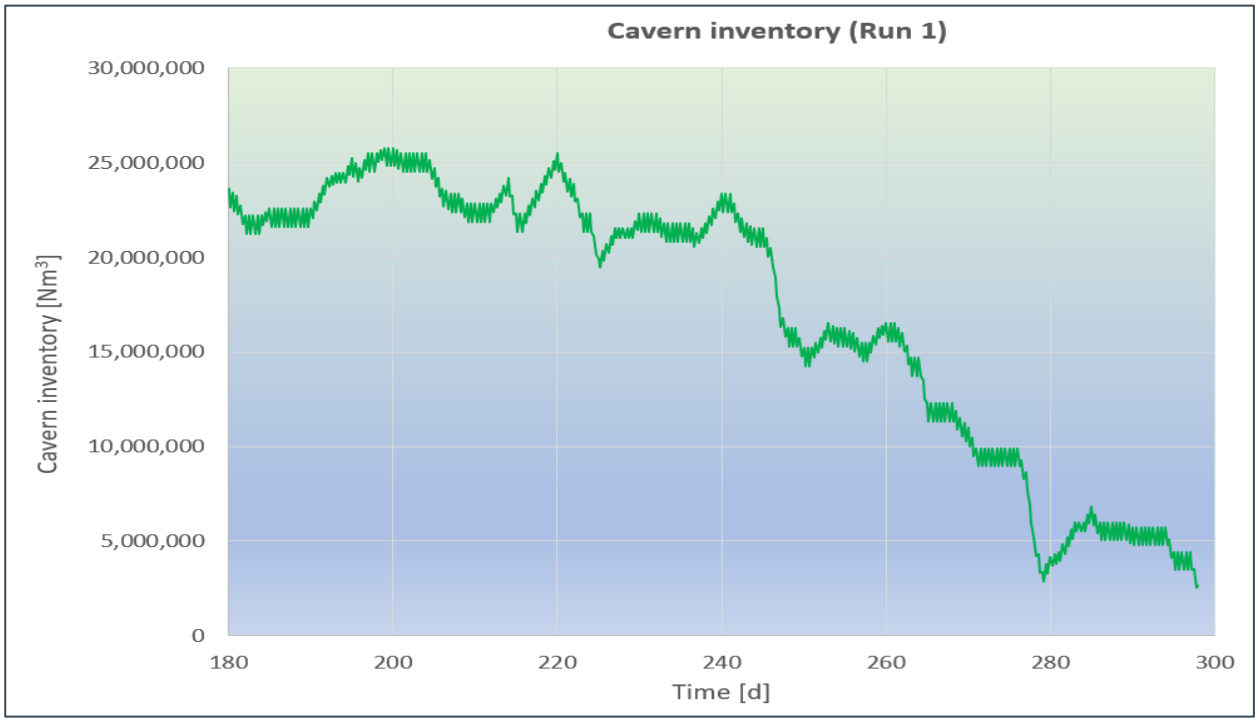

Figure G2-2: Run 1, Cavern inventory profile

Figure G2-3: Run1, Cavern pressure profile

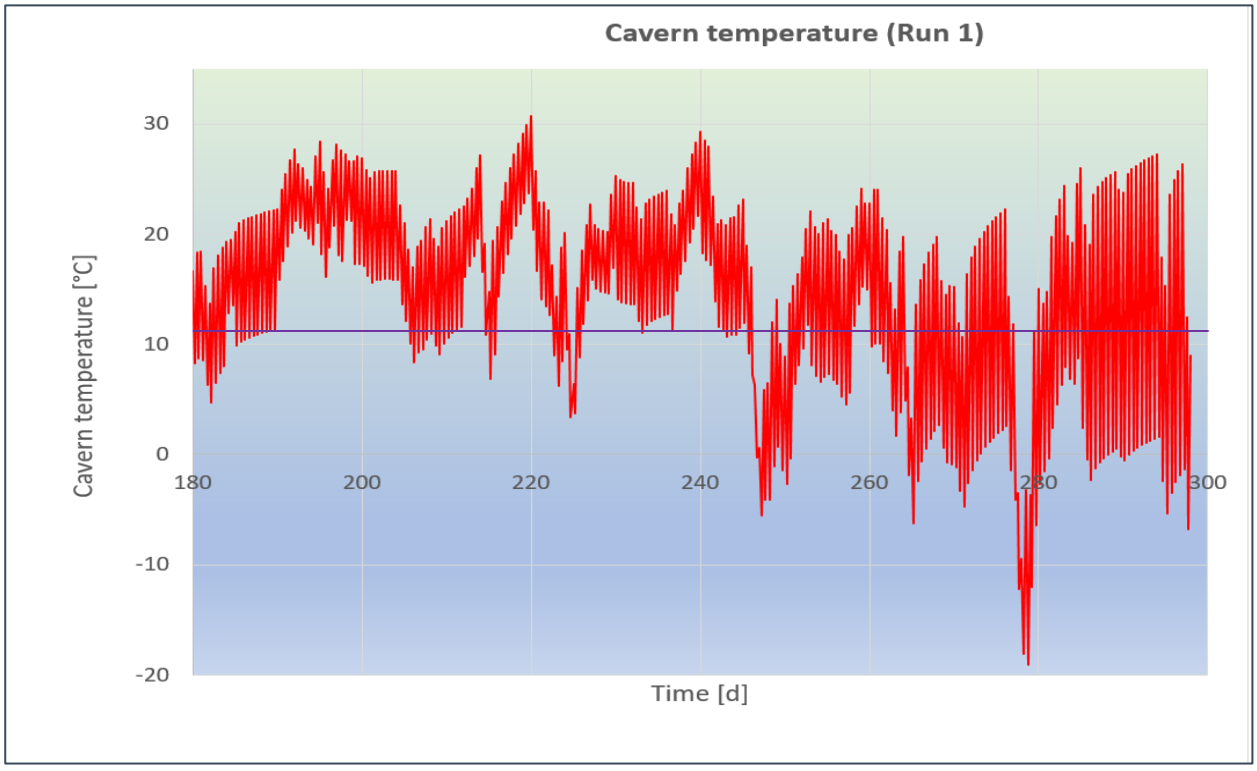

Figure G2-4: Run 1, cavern temperature profile

G.2.2. Run 2, 3 cavern basis:

In Run 2, three caverns were used and the employed H_2 flowrates are shown in Table G2-2.

Table G2-2 Flow rates used for Run 2 incorporating three caverns

	Volume flowrates per cavern			
	0.208 day	0.292 day	0.208 day	0.292 day
	Cycle 1 Part1	Cycle 1 Part2	Cycle 2 Part1	Cycle 2 Part2
Day	$Nm^3/5hr$	$Nm^3/7hr$	$Nm^3/5hr$	$Nm^3/7hr$
1	-328214	-110423	-328214	-110423
2	-328214	548304	-328214	548304
3	-328214	811424	-328214	811424
4	-328214	810490	-328214	810490
5	-328214	416435	-328214	416435
6	-328214	809549	-328214	809549
7	-656428	351536	-656428	351536
8	-656428	744649	-656428	744649
9	-656428	744649	-656428	744649
10	-656428	744649	-656428	744649
11	-656428	614246	-656428	614246
12	-656428	744649	-656428	744649
13	-656428	744649	-656428	744649
14	-656428	744649	-656428	744649
15	-656428	744649	-656428	744649
16	-656428	94236	-656428	94236
17	-656428	744649	-656428	744649
18	-656428	744649	-656428	744649
19	-656428	-166678	-656428	-166678
20	…….	……	…….	…….
…	…….	……	…….	…….

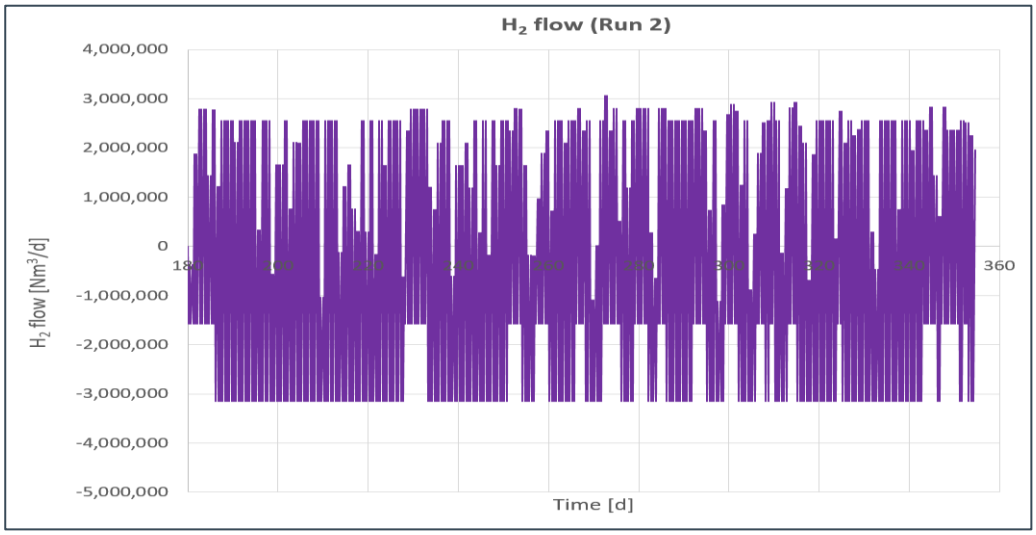

Figure G2-5: Run 2, flowrates profile

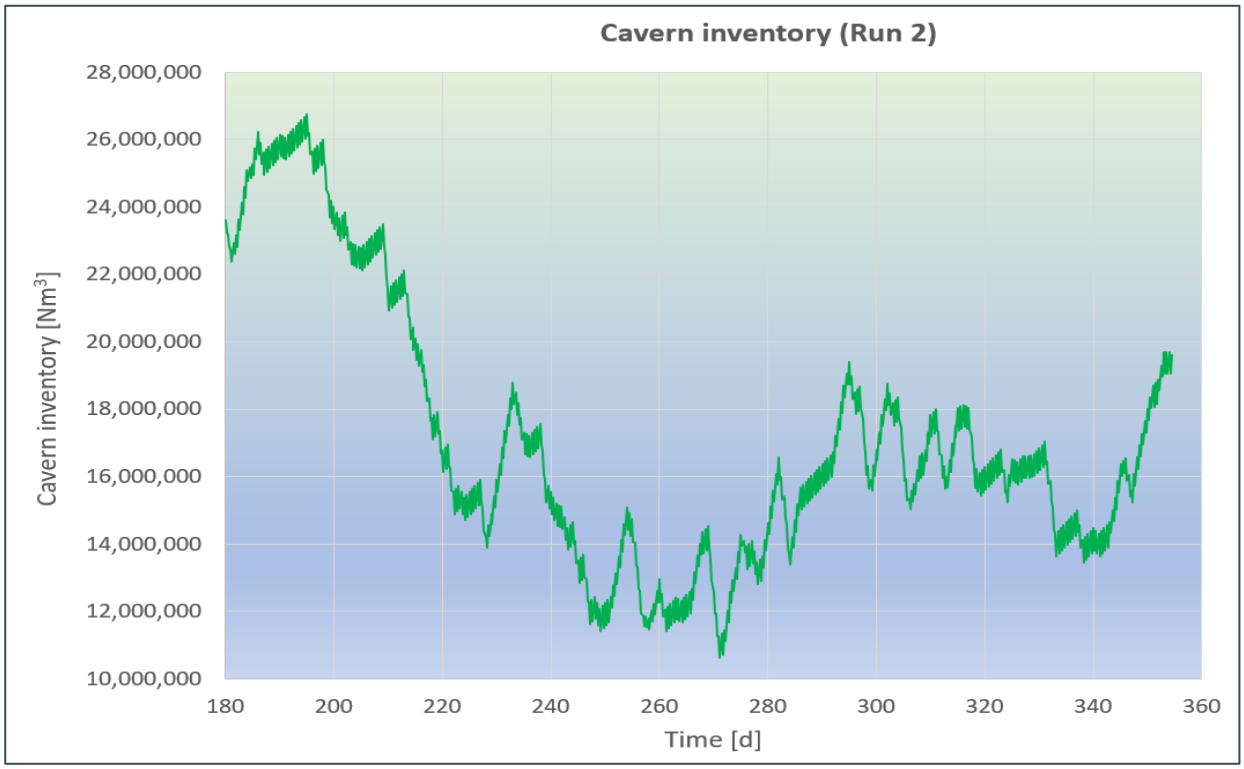

Figure G2-6: Run 2, Cavern inventory profile

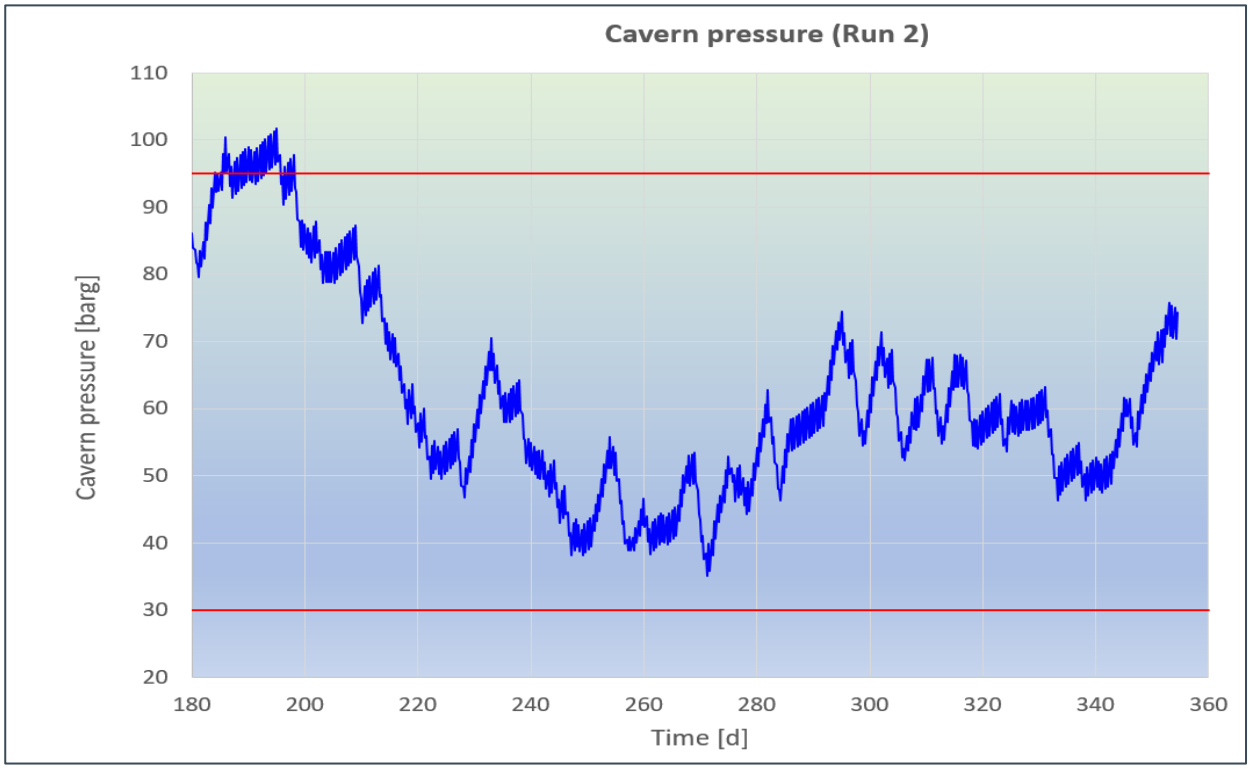

Figure G2-7: Run 2, Cavern pressure profile

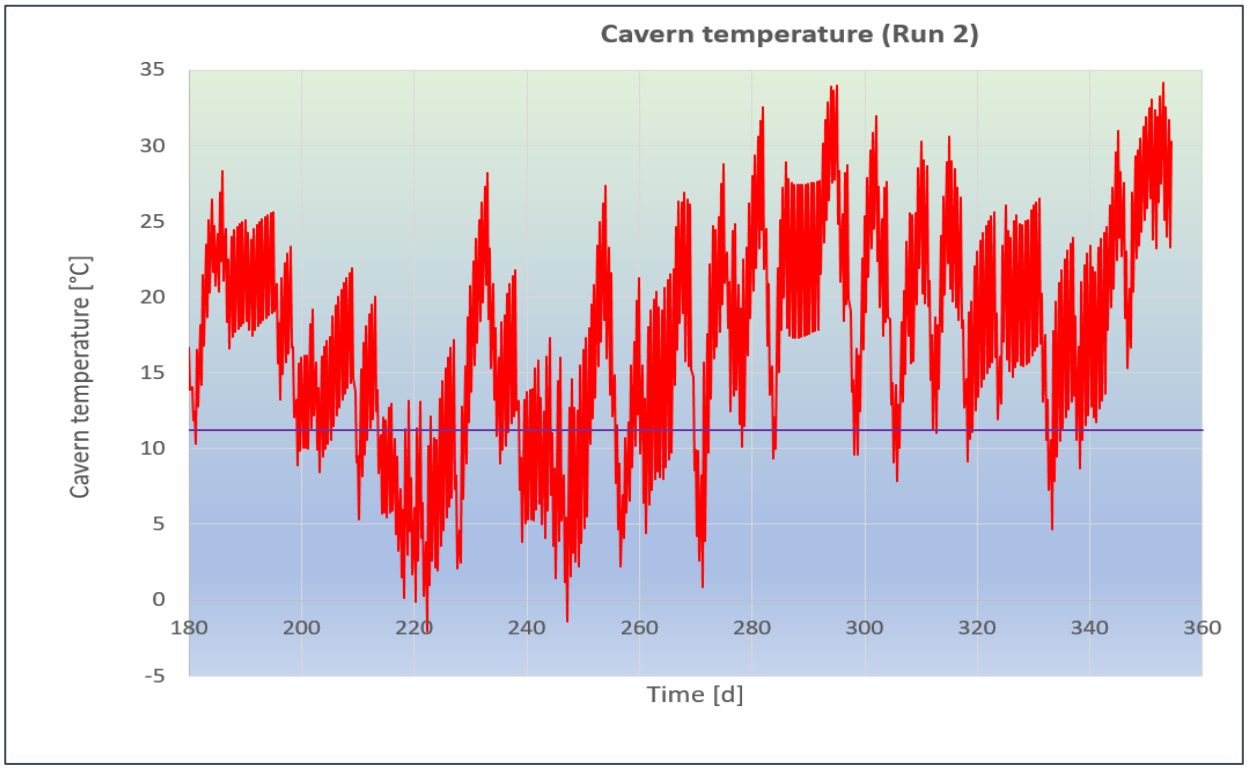

Figure G2-8: Run 2, Cavern temperature profile

G.2.3. Run 3, 5 cavern basis:

in Run 3, five caverns were used and the employed H_2 flowrates are shown in Table G2-3,

Table G2-3: Flow rates used for Run 3 incorporating five caverns

	Volume flowrates per cavern			
	0.208 day	0.292 day	0.208 day	0.292 day
	Cycle 1 Part1	Cycle 1 Part2	Cycle 2 Part1	Cycle 2 Part2
Day	$Nm^3/5hr$	$Nm^3/7hr$	$Nm^3/5hr$	$Nm^3/7hr$
1	-196928	-241708	-196928	-241708
2	-196928	417019	-196928	417019
3	-196928	680138	-196928	680138
4	-196928	679204	-196928	679204
5	-196928	285150	-196928	285150
6	-196928	678263	-196928	678263
7	-393857	88965	-393857	88965
8	-393857	482078	-393857	482078
9	-393857	482078	-393857	482078
10	-393857	482078	-393857	482078
11	-393857	351675	-393857	351675
12	-393857	482078	-393857	482078
13	-393857	482078	-393857	482078
14	-393857	482078	-393857	482078
15	-393857	482078	-393857	482078
16	-393857	-168336	-393857	-168336
17	-393857	482078	-393857	482078
18	-393857	482078	-393857	482078
19	-393857	-429249	-393857	-429249

20	…….	……	…….	…….
…	…….	……	…….	…….

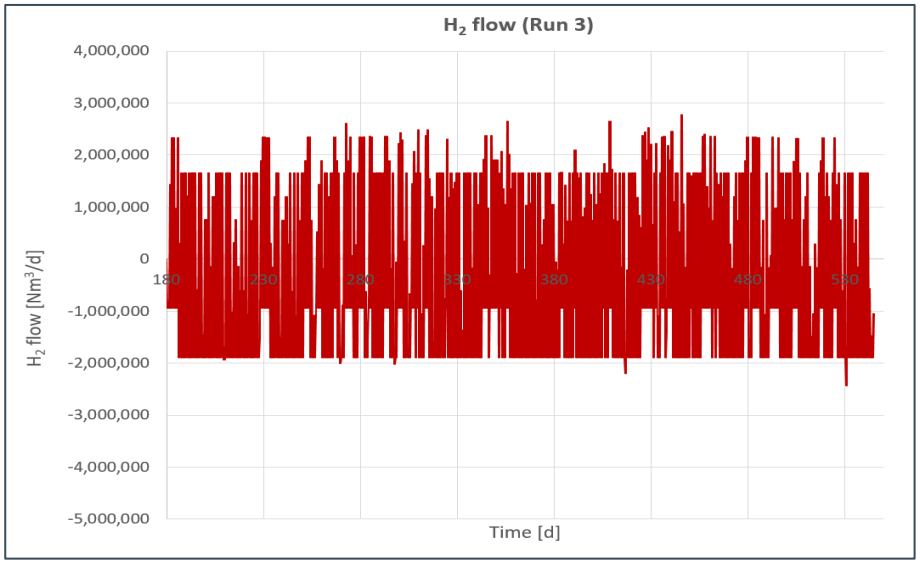

Figure G2-9: Run 3, flowrates

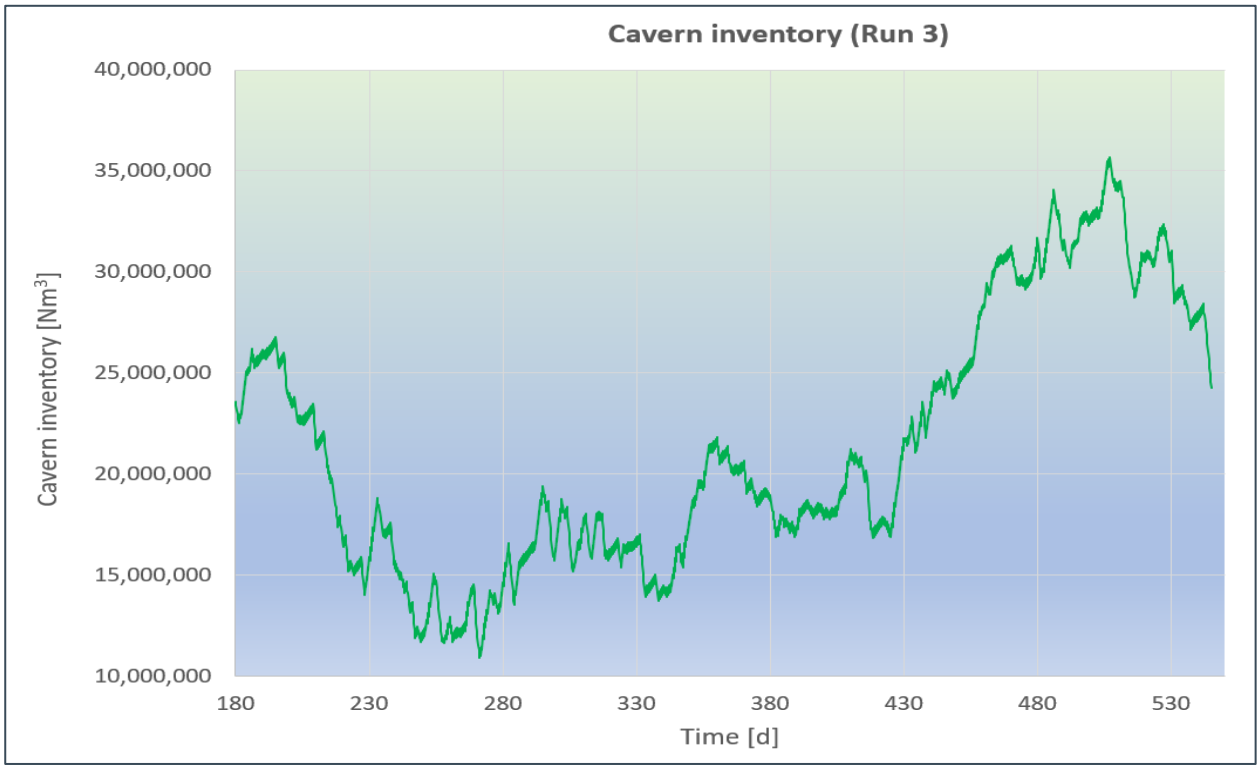

Figure G2-10: Run 3, Cavern inventory profile

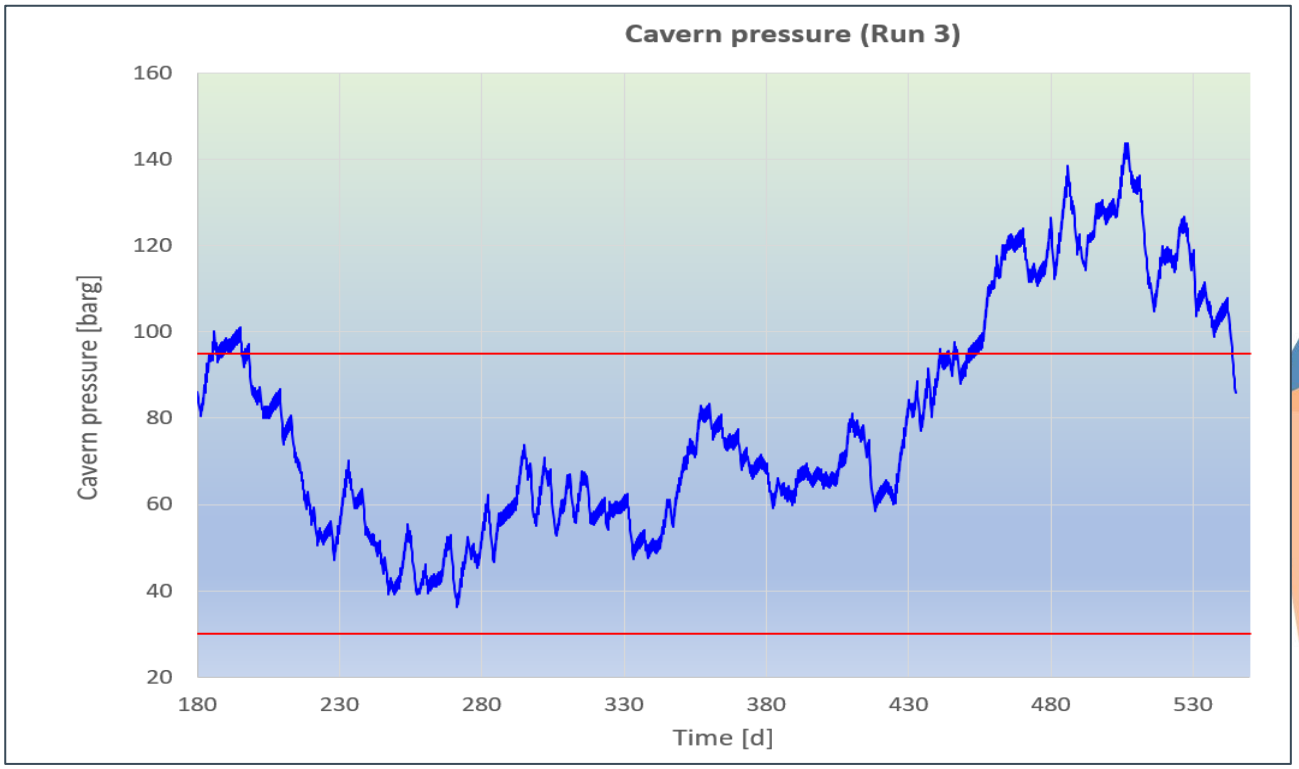

Figure G2-11: Run 3, Cavern pressure profile

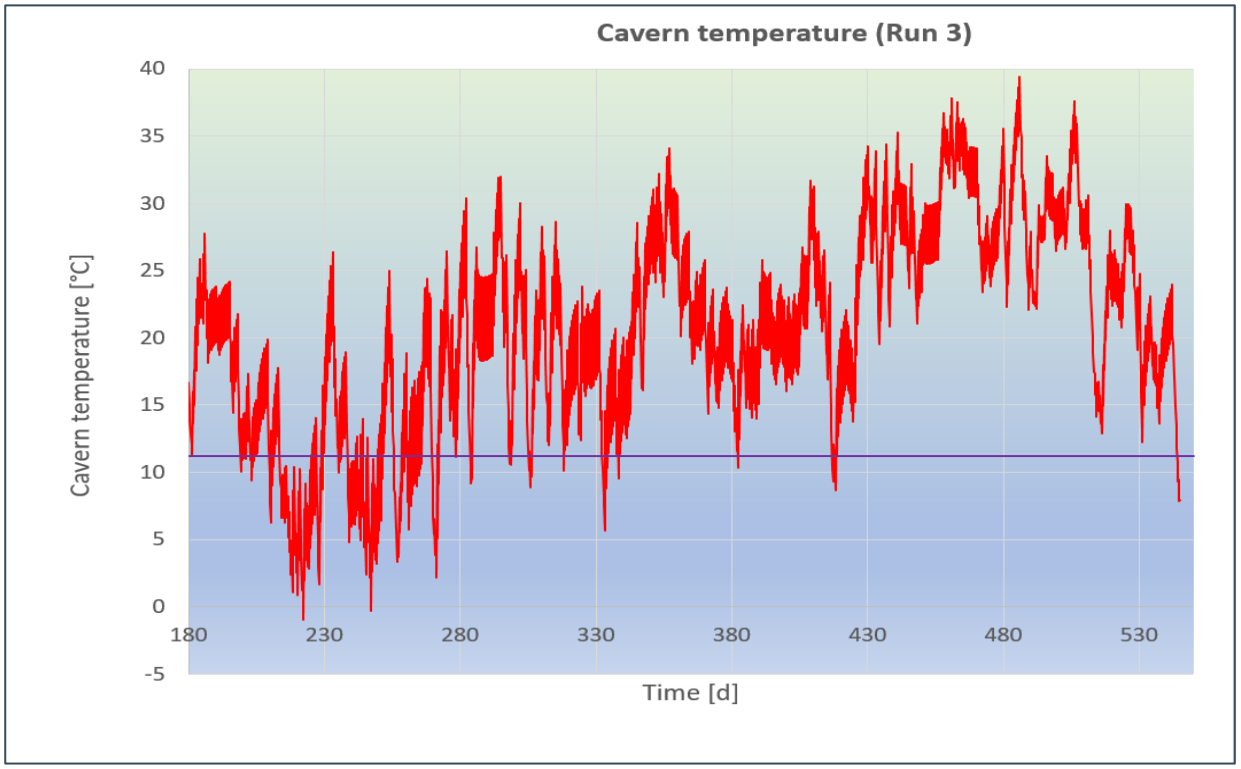

Figure G2-12: Run 3, Cavern temperature profile

G.2.4. Run 4, 3 cavern basis:

In Run 4, three caverns were used and the employed H_2 flowrates are shown in Table G2-4.

Table G2-4: Flow rates used for Run 4 incorporating three caverns

	Volume flowrates per cavern			
	0.208 day	0.292 day	0.208 day	0.292 day
	Cycle 1 Part1	Cycle 1 Part2	Cycle 2 Part1	Cycle 2 Part2
Day	$Nm^3/5hr$	$Nm^3/7hr$	$Nm^3/5hr$	$Nm^3/7hr$
1	-328214	-110423	-328214	-110423
2	-328214	351536	-328214	351536
3	-328214	351536	-328214	351536
4	-328214	351536	-328214	351536
5	-328214	416435	-328214	416435
6	-328214	351536	-328214	351536
7	-656428	351536	-656428	351536
8	-656428	744649	-656428	744649
9	-656428	744649	-656428	744649
10	-656428	744649	-656428	744649
11	-656428	614246	-656428	614246
12	-656428	744649	-656428	744649
13	-656428	744649	-656428	744649
14	-656428	744649	-656428	744649
15	-656428	656428	-656428	656428
16	-656428	94236	-656428	94236
17	-656428	744649	-656428	744649
18	-656428	744649	-656428	744649
19	-656428	-166678	-656428	-166678
20	…….	……	…….	…….
…	…….	……	…….	…….

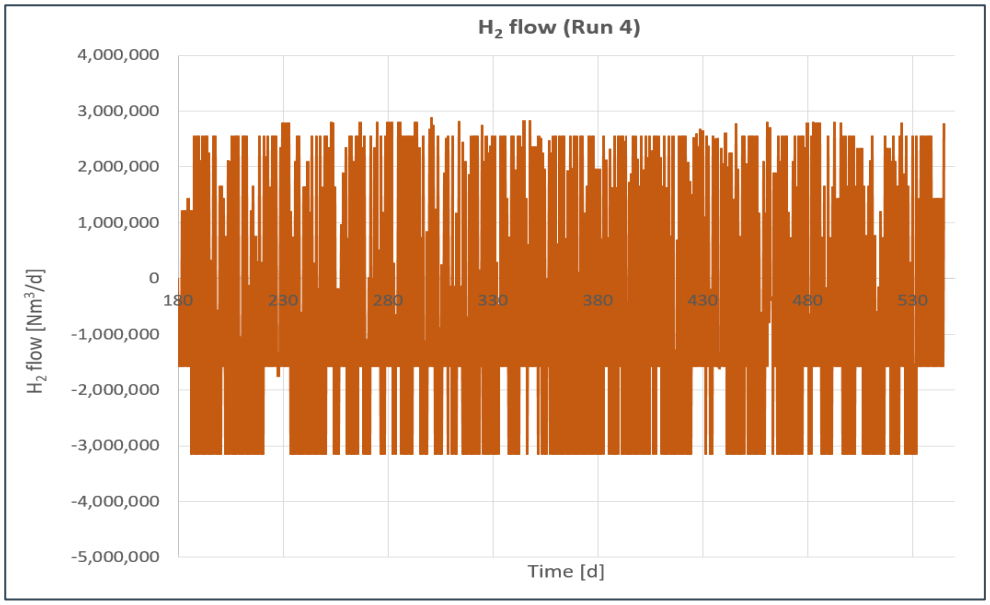

Figure G2-13: Run 4, flowrates profile

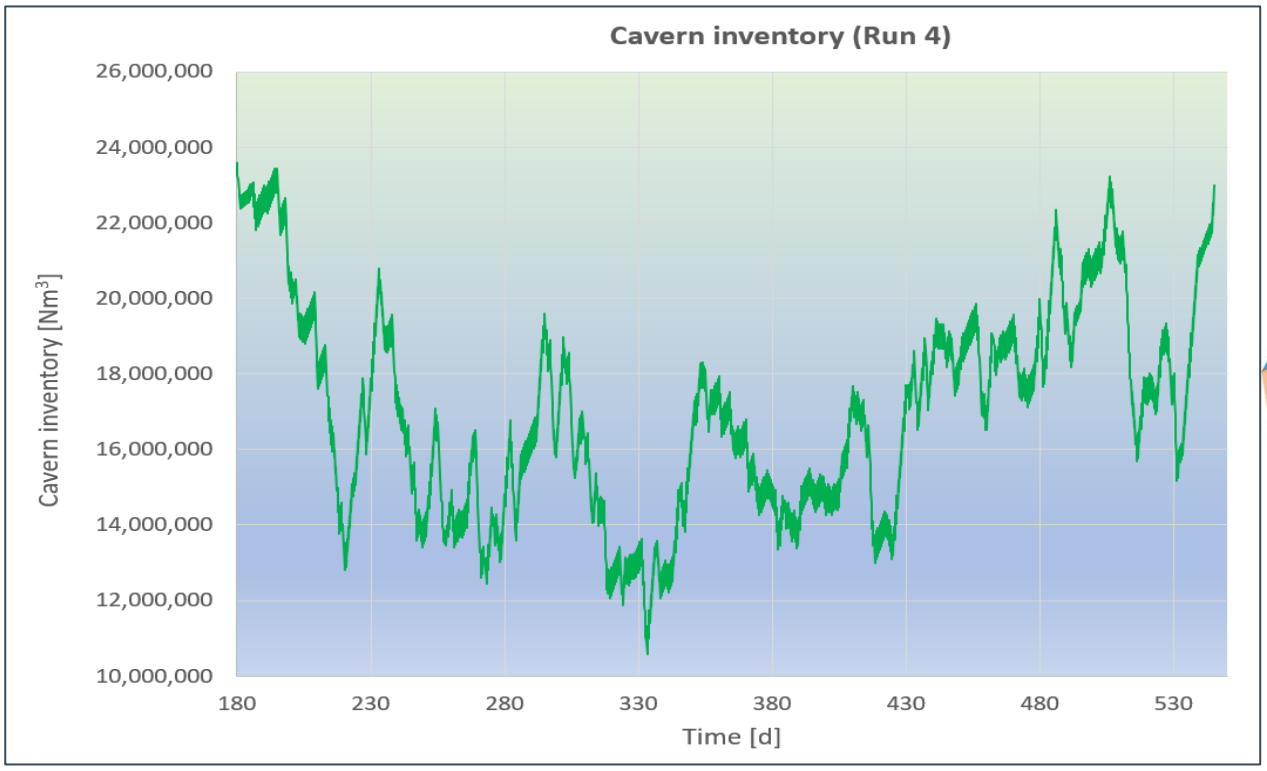

Figure G2-14: Run 4, Cavern inventory profile

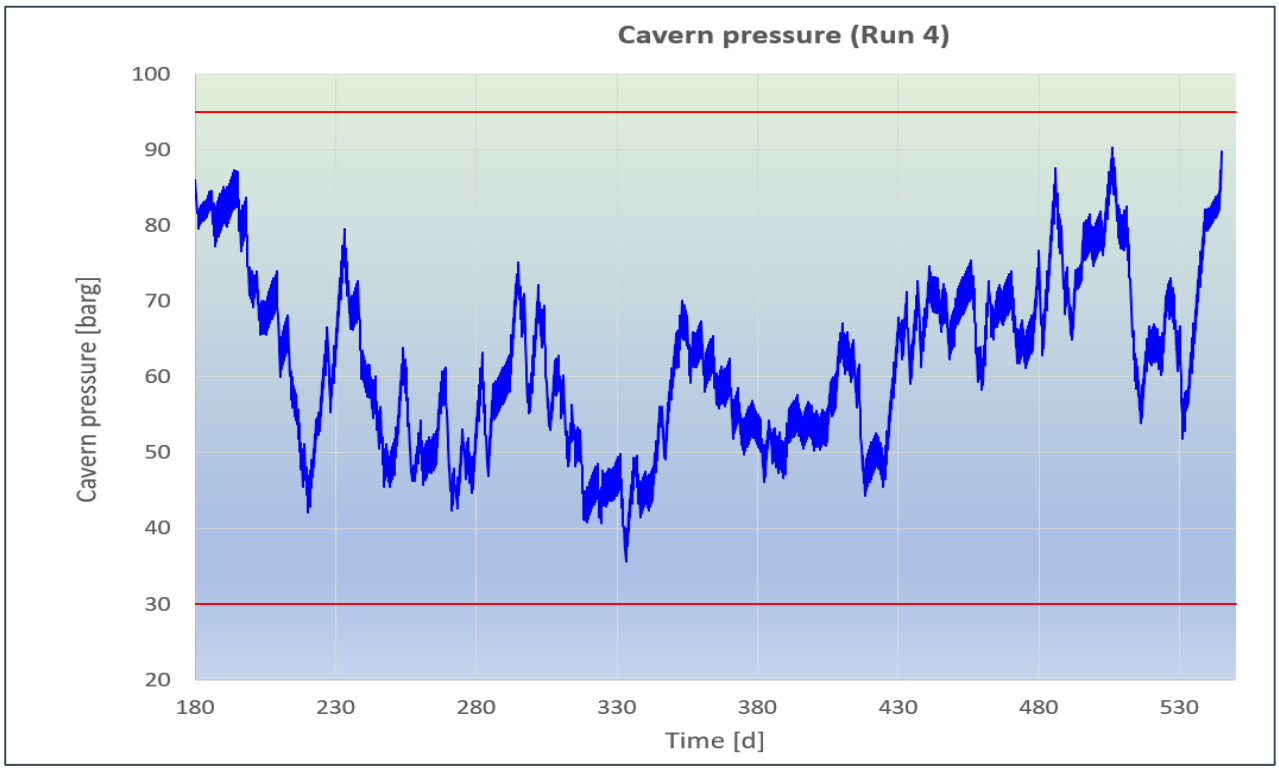

Figure G2-15: Run 4, Cavern pressure profile

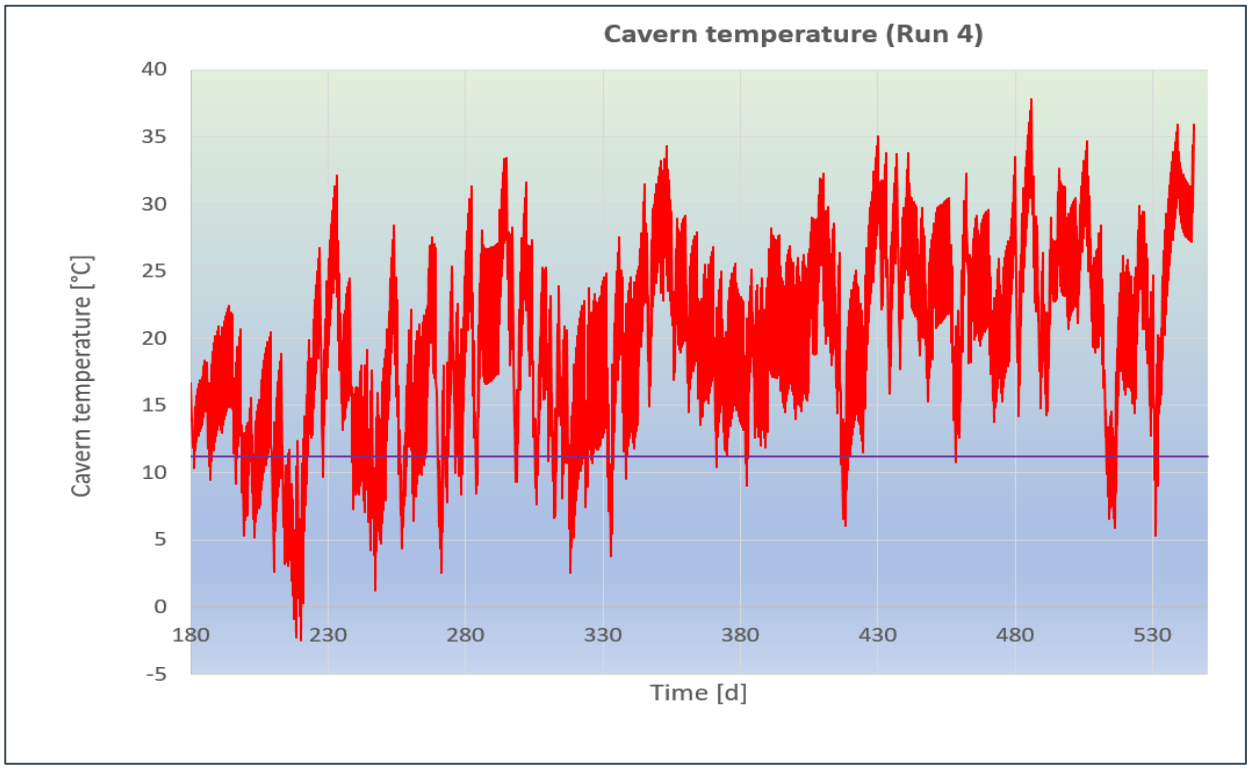

Figure G2-16: Run 4, Cavern temperature profile